

HEAVY AND HEAVY-LIGHT MESON MASSES IN THE FRAMEWORK OF TRIGONOMETRIC ROSEN-MORSE POTENTIAL USING THE GENERALIZED FRACTIONAL DERIVATIVE[†]

✉ Mohamed Abu-Shady^a, ✉ Etido P. Inyang^{b*}

^aDepartment of Mathematics and Computer Science, Faculty of Science, Menoufia University, Egypt
E-mail: dr.abushaddy@gmail.com

^bDepartment of Physics, National Open University of Nigeria, Jabi, Abuja, Nigeria

*Corresponding Author: einyang@noun.edu.ng

Received September 29, 2022; revised November 18, 2022 accepted November 20, 2022

Trigonometric Rosen-Morse Potential is employed as a mesonic potential interaction. The extended Nikiforov-Uvarov method is used to solve the N-radial Fractional Schrödinger equation analytically. Using the generalized fractional derivative, the energy eigenvalues are obtained in the fractional forms. The current findings are used to calculate the masses of mesons such as charmonium, bottomonium, and heavy-light mesons. The current findings are superior to those of other recent studies and show good agreement with experimental data as a result, the fractional parameter is crucial in optimizing meson masses.

Keywords: Trigonometric Rosen-Morse potential, Extended Nikiforov-Uvarov method, Generalized fractional derivative

PACS: 12.39.Jh

INTRODUCTION

Hadrons are made up of quarks and gluons, which are more fundamental particles. Quantum chromodynamics (QCD) is the quantum theory of these particles. This theory has vital properties such as asymptotic freedom, spontaneous symmetry breaking, and confinement. Because of the asymptotic freedom, perturbative QCD calculations work in high-energy physics. The low-energy effective field theory is used to examine non-perturbative QCD phenomena. The properties of the heavy and light hadrons can be studied in two ways: the relativistic quark models [1-4] and the non-relativistic quark models [5-10]. The Schrödinger equation (SE) is used as a non-relativistic quark model. As a result, the SE solutions are critical for computing quarkonium masses. For specific potentials, numerous methods have been utilized to find exact and approximate SE solutions, such as the Nikiforov-Uvarov (NU) method [11-13] among others [14-16]. The trigonometric Rosen-Morse potential (TRMP) has recently gained popularity as a useful potential for QCD. The potential is used in one-dimensional space according to references [17, 18]. Deta et al. [19] used the NU approach to expand the investigation to D-dimensional space. According to Abu-Shady and Ezz-Alarb [6], the trigonometric quark confinement potential is an effective tool for quark model estimates of heavy meson properties using exact-analytical iteration method.

The fractional calculus has recently garnered attention in various domains of physics that feature nonlinear, complex phenomena, such as Refs. [11, 20] where the authors used the conformable fractional derivative to solve the fractional N-dimensional radial SE with extended Cornell potential by using the extended Nikiforov-Uvarov (ENU) method. Recently, Abu-shady and Kaabar [21] suggested a new definition for fractional derivative called the generalized fractional derivative and it coincides with classical fractional derivative and also a simple tool for fractional differential equations.

This work aims to employ the TRMP to calculate the mass spectra (MS) of heavy and heavy-light meson in the framework of fractional SE by using the generalized fractional extended Nikiforov-Uvarov method (GFD-ENU).

TRIGONOMETRIC ROSEN- MORSE POTENTIAL

The features of TRMP is discussed in this section, and it takes the form [6, 22].

$$V(z) = \frac{1}{2\mu d^2} \left(-2b \cot|z| + \frac{a(a+1)}{(\sin|z|)^2} \right), \quad (1)$$

where $a = 1, 2, 3$, and $z = r/d$. μ, b, d are parameters to be determined later.

We expand the potential in a Taylor series for small z and have:

$$V(r) = -\frac{A}{r} + Br + \frac{C}{r^2} + Dr^2, \quad (2)$$

[†] Cite as: M. Abu-Shady, and E.P. Inyang, East Eur. J. Phys. 4, 80 (2022), <https://doi.org/10.26565/2312-4334-2022-4-06>
© M. Abu-Shady, E.P. Inyang, 2022

where

$$A = \frac{b}{\mu d}, \quad B = \frac{b}{3\mu d^3}, \quad C = \frac{a(a+1)}{2\mu}, \quad \text{and} \quad D = \frac{a(a+1)}{30\mu d^4} \tag{3}$$

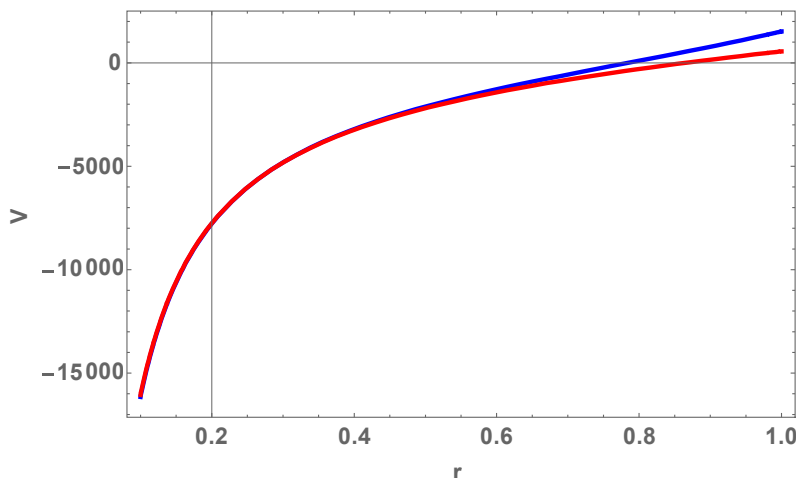


Figure 1. Plot of TRMP for the exact and approximate potential

The plot of the TRMP as a function of r is shown in Fig.1, we note that TRMP has two features the Coulomb potential (CP) and confinement potential, the short distance is described by CP and the long distance is describe by the confinement force. The approximate and exact potentials concise at point up to 0.8 fm. Therefore, TRMP is a good potential for the depiction of quarkonium interaction.

GENERALIZED FRACTIONAL DERIVATIVE OF THE SCHRÖDINGER EQUATION

The SE in the N -dimensional space is of the form [7].

$$\left[\frac{d^2}{dr^2} + \frac{N-1}{r} \frac{d}{dr} - \frac{L(L+N-2)}{r^2} + 2\mu(E_{nl} - V(r)) \right] \psi(r) = 0, \tag{4}$$

where L , N , and μ are the angular momentum quantum number, the dimensionality number, and the reduced mass, respectively.

We set the wave function $\psi(r) = r^{\frac{1-N}{2}} R(r)$, and Eq. (4) takes the form

$$\left[\frac{d^2}{dr^2} + 2\mu(E_{nl} - V(r)) - \frac{\left(L + \frac{N-2}{2}\right)^2 - \frac{1}{4}}{r^2} \right] R(r) = 0, \tag{5}$$

By substituting Eq. (2) into Eq. (5), we obtain the following equation

$$\left[\frac{d^2}{dr^2} + 2\mu \left(E_{nl} + \frac{A}{r} - Br - \frac{C}{r^2} - Dr^2 \right) - \frac{\left(L + \frac{N-2}{2}\right)^2 - \frac{1}{4}}{r^2} \right] R(r) = 0, \tag{6}$$

Eq. (6) is compact in the form

$$\left[\frac{d^2}{dr^2} + \frac{1}{r^2} (\varepsilon r^2 + A_1 r - B_1 r^3 - C_1 - D_1 r^4) \right] R(r) = 0, \tag{7}$$

where

$$\varepsilon = 2\mu E_{nl}, \quad A_1 = 2\mu A, \quad B_1 = 2\mu B, \tag{8}$$

$$C_1 = 2\mu C + \left(L + \frac{N-2}{2} \right)^2 - \frac{1}{4}, \quad D_1 = 2\mu D. \tag{9}$$

To put Eq. (7) in the fractional form, firstly, we introduce the dimensionless form by introducing $Z = \frac{r}{w}$ where W is scalar quantity measure in 1 GeV

$$\left[\frac{d^2}{dz^2} + \frac{1}{z^2} (\varepsilon z^2 + A_1 z - B_1 z^3 - C_1 - D_1 z^4) \right] R(z) = 0, \tag{10}$$

where

$$\left. \begin{aligned} \varepsilon &= \frac{2\mu E_{nl}}{w^2}, \quad A_1 = \frac{2\mu A}{w}, \quad B_1 = \frac{2\mu B}{w^3}, \\ C_1 &= 2\mu C + \left(L + \frac{N-2}{2} \right)^2 - \frac{1}{4}, \quad D_1 = \frac{2\mu D}{w^4} \end{aligned} \right\} \tag{11}$$

We write generalized fractional derivative Eq. (10) as in [21],

$$\left[D^\alpha D^\alpha + \frac{1}{z^{2\alpha}} (\varepsilon z^{2\alpha} + A_1 z^\alpha - B_1 z^{3\alpha} - C_1 - D_1 z^{4\alpha}) \right] R(z) = 0, \tag{12}$$

where the potential defines in Eq. (2) is replaced by

$$V(z) = -\frac{A}{z^\alpha} + Bz^\alpha + \frac{C}{z^{2\alpha}} + Dz^{2\alpha}, \tag{13}$$

by using the generalized fractional derivative in Ref. [21] and also Ref. [13].

$$D^\alpha \left[D^\alpha R(z) \right] = \lambda^2 \left[(1-\alpha) z^{1-2\alpha} R'(z) + s^{2-2\alpha} R''(z) \right], \tag{14}$$

where

$$\lambda = \frac{\Gamma(\beta)}{\Gamma(\beta-\alpha+1)} \text{ with } 0 < \alpha \leq 1 \text{ and with } 0 < \beta \leq 1. \tag{15}$$

By substituting Eq. (14) into (12), we get

$$R_{nl}''(z) + \frac{1-\alpha}{z} R_{nl}'(z) + \frac{1}{z^2} (\varepsilon z^{2\alpha} + A_1 z^\alpha - Bz^{3\alpha} - C_1 - D_1 z^{4\alpha}) R(z) = 0, \tag{16}$$

where

$$\left. \begin{aligned} \bar{\tau}_r(s) &= 1 - \alpha, \quad \sigma(s) = z, \\ \tilde{\sigma}(s) &= \frac{1}{\lambda^2} (\varepsilon_n Z^{2\alpha} + A_1 Z^\alpha - B_1 Z^{3\alpha} - C_1 - D_1 Z^{4\alpha}), \\ \lambda &= \frac{\Gamma(\beta)}{\Gamma(\beta-\alpha+1)} \end{aligned} \right\} \tag{17}$$

By using ENU-CFD method [11], we obtain π_f

$$\pi_f = \frac{\alpha}{2} \pm \sqrt{\frac{\alpha^2}{4} - \frac{1}{\lambda^2} (\varepsilon_n Z^{2\alpha} + A_1 Z^\alpha - B_1 Z^{3\alpha} - C_1 - D_1 Z^{4\alpha}) + zG(z)}. \tag{18}$$

To choose the function form of $G(z)$. We then find a function $G(z) = S + Pz^{\alpha-1} + Qz^{2\alpha-1}$ that makes the function under the root in the above equation to become quadratic

$$\pi_f = \frac{\alpha}{2} \pm \sqrt{(A_{11} + B_{11} Z^\alpha + F_{11} Z^{2\alpha})^2}. \tag{19}$$

then

$$\pi_f = \frac{\alpha}{2} \pm (A_{11} + B_{11}Z^\alpha + F_{11}Z^{2\alpha}). \quad (20)$$

Substituting $G(z)$ in Eq. (18) and then equating the coefficients in Eqs. (18 and 20). To find the constants S, P, Q, A_{11}, B_{11} , and F_{11}

$$(A_{11} + B_{11}Z^\alpha + F_{11}Z^{2\alpha})^2 = \frac{\alpha^2}{4} - \frac{1}{\lambda^2} (\varepsilon_{nl}Z^{2\alpha} + A_1Z^\alpha - B_1Z^{3\alpha} - C_1 - D_1Z^{4\alpha}) + z(s + pz^{\alpha-1} + Qz^{2\alpha-1}) \quad (21)$$

so, we obtain

$$\left(A_{11}^2 - \frac{\alpha^2}{4} - \frac{C_1}{\Gamma^2} \right) + (2A_{11}B_{11} + A_1 - p)Z^\alpha + (B_{11}^2 + 2A_{11}F_{11} + \varepsilon_{nl} - Q)Z^{2\alpha} + (2B_{11}F_{11} - B_1)Z^{3\alpha} + (F_{11}^2 - D_1)Z^{4\alpha} = 0 \quad (22)$$

then, we have

$$A_{11} = -\frac{1}{2} \sqrt{\alpha^2 + \frac{4C_1}{\lambda^2}}, \quad (23)$$

$$B_{11} = \frac{-A_1 + p}{2A_{11}} = \frac{-A_1 + p}{\sqrt{\alpha^2 + \frac{4C_1}{\lambda^2}}}, \quad (24)$$

$$F_{11}^2 - D_1 = 0 \Rightarrow F_{11} = \sqrt{D_1}, \quad (25)$$

$$2B_{11}F_{11} - B_1 = 0 \Rightarrow B_{11} = \frac{B_1}{2\sqrt{D_1}} \quad (26)$$

$$B_{11}^2 + 2A_{11}F_{11} + \varepsilon_{nl} - Q = 0 \Rightarrow \varepsilon_{nl} = Q - B_{11}^2 - 2A_{11}F_{11} \quad (27)$$

By using Eqs. (23-26), we have

$$\varepsilon_{nl} = -\frac{B_1^2}{4D_1} + \sqrt{D_1} \left[2\alpha(1+n) + \sqrt{\alpha^2 + \frac{4}{\lambda^2} \left(2\mu C + \left(l + \frac{N-2}{2} \right)^2 - \frac{1}{4} \right)} \right], \quad (28)$$

from Eq. (28), we obtain the energy spectrum of the TRMP

$$E_{nl} = -\frac{B^2}{4D} + \sqrt{\frac{2D}{\mu}} \left[2\alpha(1+n) + \sqrt{\alpha^2 + \frac{4}{\lambda^2} \left(2\mu C + \left(l + \frac{N-2}{2} \right)^2 - \frac{1}{4} \right)} \right] \quad (29)$$

MASS SPECTRA OF HEAVY AND HEAVY-LIGHT MESONS

The MS of the heavy and heavy-light mesons is predicted in the 3-dimensional (N=3), by applying the relation [23,24].

$$M = m_q + m_{\bar{q}} + E_{nl}, \quad (30)$$

where m is bare quark mass for quarkonium.

Plugging Eq. (29), into Eq. (30) gives:

$$M = m_q + m_{\bar{q}} - \frac{B^2}{4D} + \sqrt{\frac{2D}{\mu}} \left[2\alpha(1+n) + \sqrt{\alpha^2 + \frac{4}{\lambda^2} \left(2\mu C + \left(l + \frac{N-2}{2} \right)^2 - \frac{1}{4} \right)} \right] \quad (31)$$

where $\lambda = \frac{\Gamma(\beta)}{\Gamma(\beta - \alpha + 1)}$, $0 < \alpha \leq 1$ and $0 < \beta \leq 1$

RESULTS AND DISCUSSION

Using Eq. (31), we determined the MS of charmonium for the states 1S to 4S as displayed in Table (1). The experimental data (ED) are used to fit the free parameters of the current computations, B, D, and C. Additionally, bare quark masses may be found in Ref. [6]. By calculating total error in comparison with ED, we observe that estimations of charmonium masses are in good agreement with ED and are improved over Refs. [6, 25, 26] that used different potentials and methods. Table (2) show that the bottomonium spectrum masses for states 1S to 4S coincide with ED and that the current calculations are more accurate than those in Refs. [6, 25-27], with a smaller total error.

Table 1. Mass spectra of charmonium (in GeV), ($m_c = 1.275 \text{ GeV}$ [31], $\mu = 0.638 \text{ GeV}$, $D = 0.2630 \text{ GeV}^{-1}$, $B = 1.4925 \text{ GeV}^2$, $N = 3$, $\alpha = 0.1$, $\beta = 1$, $C = 4.7598$)

State	Present paper	[25]	[26]	[27]	[6]	N=4	Exp. [31]
1S	3.096	3.078	3.096	3.078	3.239	3.352	3.096
1P	3.421	3.415	3.433	3.415	3.372	3.533	3.525
2S	3.649	4.187	3.686	3.581	3.646	3.675	3.649
1D	3.757	3.752	3.767	3.749	3.604	4.158	3.769
2P	3.899	4.143	3.910	3.917	3.779	3.715	3.900
3S	4.040	5.297	3.984	4.085	4.052	4.684	4.040
4S	4.399	6.407	4.150	4.589	4.459	5.463	4.415
Total Error	0.00521	0.9513	0.11065	0.11152	0.05788	0.09147	

Table 2. Mass spectra of bottomonium (in GeV), ($m_b = 4.18 \text{ GeV}$ [31], $\mu = 2.09 \text{ GeV}$, $D = 0.347 \text{ GeV}^{-1}$, $B = 0.5231 \text{ GeV}^2$, $\alpha = 0.1$, $C = -0.0154$, $\beta = 1$)

State	Present paper	[25]	[27]	[26]	[6]	N=4	Exp. [31]
1S	9.445	9.510	9.510	9.460	9.495	9.552	9.444
1P	9.915	9.862	9.862	9.840	9.657	10.458	9.900
2S	10.023	10.627	10.038	10.023	10.023	10.567	10.023
1D	10.162	10.214	10.214	10.140	10.161	10.453	10.161
2P	10.246	10.944	10.390	10.160	10.26	10.564	10.260
3S	10.355	11.726	10.566	10.280	10.355	10.473	10.355
4S	10.553	12.834	11.094	10.420	10.579	10.654	10.579
Total Error	0.000917	0.488529	0.09777	0.08207	0.09612	0.03086	

For states from 1S to 3S, we use the $2m = m_b + m_c$ part of Eq. (31) to calculate the MS of heavy-light ($b\bar{c}$) mesons. We notice that the 1S and 2S states are closer, but the ED for the other states is not known. By calculating the sum error for these works, we can see that the current predictions of the $b\bar{c}$ mass are better than those in Refs. [6, 28, 29]. Using the $2m = m_c + m_s$ part of Eq. (31), we compute the MS of the $c\bar{s}$ mesons from the 1S to the 1D state in Table (4). Close to ED are 1S and 2S. By computing the total error for each potential, other states are enhanced in contrast to the screened potential and phenomenological potential [30].

In the current work, we observe that for every state, as shown in Tables (1,2,3,4), the MS increase as N is increased at $N = 4$ for various states. This resulted in the restriction of non-relativistic quark models for higher dimensional.

Table 3. Mass spectra of $b\bar{c}$ meson (in GeV) ($m_b = 4.18 \text{ GeV}$, $m_c = 1.275 \text{ GeV}$, $\mu = 0.976 \text{ GeV}$, $D = 0.23 \text{ GeV}^{-1}$, $B = 2.1150 \text{ GeV}^2$, $\alpha = 0.1$, $\beta = 1$, $C = 8.0028$)

State	Present paper	[28]	[29]	[6]	N=4	Exp. [32]
1S	6.274	6.349	6.264	6.268	6.543	6.274
1P	6.711	6.715	6.700	6.529	6.680	-
2S	6.872	6.821	6.856	6.895	7.250	6.871
2P	7.103	7.102	7.108	7.156	6.818	-
3S	7.179	7.175	7.244	7.522	8.127	-
Total	0.00002	0.01922	0.00377	0.00444	0.0490	Exp.[32]

Table 4. Mass spectra of $c\bar{s}$ meson in (GeV) ($m_c = 1.275 \text{ GeV}$, $m_s = 0.419 \text{ GeV}$, $\mu = 0.315 \text{ GeV}$, $B = 5.319 \text{ GeV}^2$, $D = 0.23 \text{ GeV}^{-1}$, $\alpha = 0.1$, $\beta = 1$, $C = 275.338$)

State	Present paper	[6]	Screened	Phenomenological	N=4	Exp.[32]
1S	1.968	1.969	1.9685	1.968	2.122	1.968
1P	2.211	2.126	2.7485	2.566	2.364	2.112
2S	2.318	2.318	2.8385	2.815	2.556	2.317
3S	2.834	2.667	3.2537	3.280	3.153	2.700
1D	2.359	2.374	-	-	2.797	2.318
Total Error	0.02827	0.04392	0.73081	0.64471	0.13502	Exp.[32]

The plots of the eigenvalues against the principal quantum number (n) are shown in Figures (2-5). In Fig. (2), it was noticed that as the dimensional number increases, the curves of the energy increase at different values of n . In addition, the curves of energy are shifted to higher values by increasing N . The variation of eigenvalues of $c\bar{c}$ against n for different values of $\alpha = 0.2$, $\alpha = 0.5$, and $\alpha = 0.7$ is shown in Fig. 3. We note the energy increases when n is increased. Also, we note that an increase in the fractional parameter leads to decreasing energy eigenvalue for $b\bar{c}$ meson and $c\bar{s}$ meson as in Figs. (4, 5). Thus, the fractional parameter makes the energy more stable.

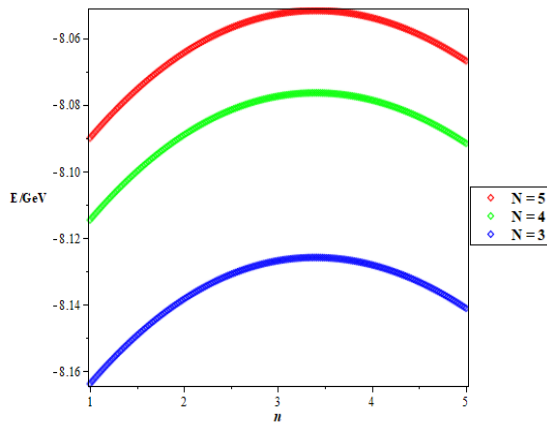


Figure 2. Variation of the energy eigenvalue with n for different dimensional numbers N

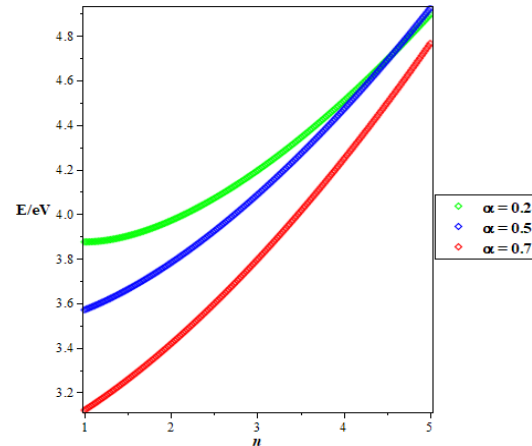


Figure 3. Variation of the energy eigenvalue of charmonium with n for different values of α

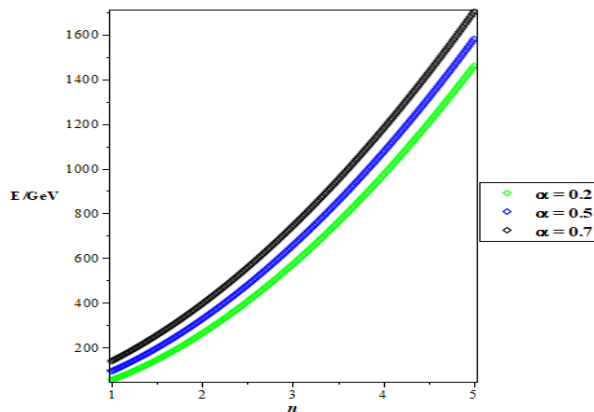


Figure 4. Variation of the energy eigenvalue of $b\bar{c}$ meson with n for different values of α

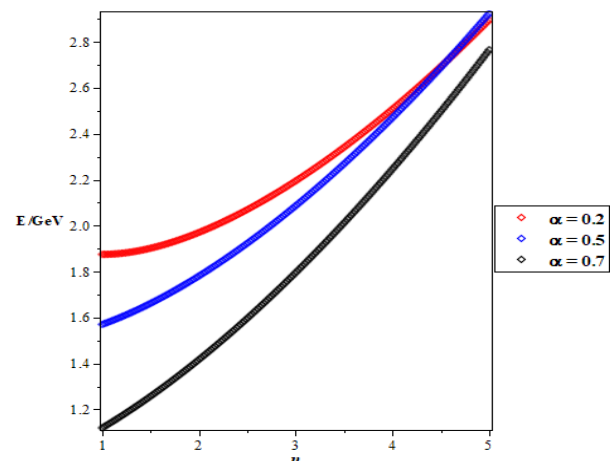


Figure 5. Variation of the energy eigenvalue of $c\bar{s}$ meson with n for different values of α

CONCLUSION

In this study, the TRMP is model to interact in a quarkonium system and the solutions of SE were obtained using the GFD-ENU method that displayed in Refs. [21, 13, 33]. The energy spectrum was obtained and used to predict the MS of the HMs and heavy-light mesons. The results obtained showed an improvement when compared with the work of other researchers and excellently agreed with ED with a total error less than the errors obtained from other results as shown in Tables 1-4. Also, the figures show that the decreasing fractional parameter leads to lower the energy eigenvalues which makes the state more stable in the fractional model.

Availability of data and materials. All data generated during this study are included in the references in the paper.

Competing interests. The authors declare that they have no competing interests.

ORCID IDs

© Mohamed Abu-Shady, <https://orcid.org/0000-0001-7077-7884>; © Etido P. Inyang, <https://orcid.org/0000-0002-5031-3297>

REFERENCES

- [1] M. Abu-shady, and Rashdan, Phys. Rev. C, **81**, 015203 (2010). <https://doi.org/10.1103/PhysRevC.81.015203>
- [2] M. Abu-shady, and H.M. Mansour, Phys. Rev. C, **85**, 055204 (2012). <https://doi.org/10.1103/PhysRevC.85.055204>
- [3] M. Rashdan, M. Abu-Shady, and T.S.T. Ali, Int. Mod. Phys. A, **22**, 2673 (2007). <https://doi.org/10.1142/S0217751X07036178>
- [4] M. Rashdan, M. Abu-Shady, and T.S.T. Ali, Int. Mod. Phys. E, **15**, 143 (2006). <https://doi.org/10.1142/S0218301306003965>

- [5] E.P. Inyang, E.O. Obisung, E.S. William, and I.B. Okon. East European Journal of Physics, **3**, 104 (2022). <https://doi.org/10.26565/2312-4334-2022-3-14>
- [6] M. Abu-Shady, and S.Y. Ezz-Alarb, Few-body systems, **60**, 66 (2019). <https://doi.org/10.1007/s00601-019-1531-y>
- [7] M. Abu-Shady, T.A. Abdel-Karim, and E.M. Khokha, Advances in High Energy Physics, **2018**, 7356843 (2018). <https://doi.org/10.1155/2018/7356843>
- [8] M. Abu-Shady, and E.M. Khokha, Advances in High Energy Physics, 7032041 (2018). <https://doi.org/10.1155/2018/7032041>
- [9] E. Omugbe, O.E. Osafire, I.B. Okon, E.P. Inyang, E.S. William, and A. Jahanshir, Few-Body systems, **63**, 7 (2022). <https://doi.org/10.1007/s00601-021-01705-1>
- [10] E.P. Inyang, E.P. Inyang, E.S. William, and E.E. Ibekwe, Jordan Journal of Physics, **14**, 339 (2021). <https://doi.org/10.47011/14.4.8>
- [11] Al-Jamel, Int. J. Mod. Phys. A, **34**, 1950054 (2019). <https://doi.org/10.1142/S0217751X19500544>
- [12] E.P. Inyang, and E.O. Obisung, East European Journal of Physics, **3**, 38 (2022). <https://doi.org/10.26565/2312-4334-2022-3-04>
- [13] H. Karayer, D. Demirhan, and F. Büyükk, Commun. Theor. Phys. **66**, 12 (2018). <https://doi.org/10.1088/0253-6102/66/1/012>
- [14] C.O. Edet, S. Mahmoud, E.P. Inyang, N. Ali, S.A. Aljunid, R. Endut, A.N. Ikot, and M. Asjad, Mathematics, **10**(15), 2824 (2022). <https://doi.org/10.3390/math10152824>
- [15] E.P. Inyang, E.S. William, J.E. Ntibi, J.A. Obu, P.C. Iwuji, and E.P. Inyang. Canadian Journal of Physics, **100**(10), 463 (2022). <https://doi.org/10.1139/cjp-2022-0030>
- [16] E.E. Ibekwe, U.S. Okorie, J.B. Emah, E.P. Inyang, and S.A. Ekong, Eur. Phys. J. Plus, **136**, 87 (2021). <https://doi.org/10.1140/epjp/s13360-021-01090-y>
- [17] C.B.C. Jasso, and M. Kirchbach, AIP Conf. Proc. **857**, 275 (2006). <https://doi.org/10.1063/1.2359266>
- [18] C.B.C. Jasso, and M. Kirchbach, J. Phys. A: Math. Gen. **39**, 547 (2006).
- [19] U.A. Deta, Suparmi, Cari, A.S. Husein, H. Yulian, I.K.A. Khaled, H. Luqman, and Supriyanto, 4th. Inter. Conf. Adv. Nucl. Sci. Eng. **1615**, 121-127 (2014). <https://doi.org/10.1063/1.4895872>
- [20] M. Abu-Shady, Inter. J. Mod. Phys. A, **34**(31), 1950201 (2019). <https://doi.org/10.1142/S0217751X19502014>
- [21] M. Abu-Shady, and M.K.A. Kaabar, Mathematical Problems in Engineering, **2021**, 9444803 (2021). <https://doi.org/10.1155/2021/9444803>
- [22] S. Sharma, Hindawi. Pub. Corp, **2013**, 452978, (2013). <https://doi.org/10.1155/2013/452978>
- [23] E.P. Inyang, E.P. Inyang, I.O. Akpan, J.E. Ntibi, and E.S. William, Canadian Journal Physics, **99**, 990 (2021). <https://doi.org/10.1139/cjp-2020-0578>
- [24] E.P. Inyang, P.C. Iwuji, J.E. Ntibi, E. Omugbe, E.A. Ibang and E.S. William, East European Journal of Physics, **2**, (2022) 51. <https://doi.org/10.26565/2312-4334-2022-2-05>
- [25] R. Kumar, and F. Chand, Commun. Theor. Phys. **59**, 528 (2013). <https://doi.org/10.1088/0253-6102/59/5/02>
- [26] N.V. Maskimenko, and S.M. Kuchin, Russ. Phys. J. **54**, 57 (2011).
- [27] R. Kumar, and F. Chand, Phys. Scr. **85**, 055008 (2012). <https://doi.org/10.1088/0031-8949/85/05/055008>
- [28] A.K. Ray, and P.C. Vinodkumar, Pramana J. Phys. **66**, 953 (2006). <https://doi.org/10.1007/BF02704795>
- [29] E.J. Eichten, and C. Quigg, Phys. Rev. D, **49**, 5845 (1994). <https://doi.org/10.1103/PhysRevD.49.5845>
- [30] D. Ebert, R.N. Faustov, and V.O. Galkin, Phys. Rev. D, **67**, 014027 (2003). <https://doi.org/10.1103/PhysRevD.67.014027>
- [31] M. Tanabashi, et al, (Particle Data Group), "Review of Particle Physics". Physical Review D, **98**(3), 030001 (2018). <https://doi.org/10.1103/PhysRevD.98.030001>
- [32] C. Patrignani, et al, (Particle data group), Chinese Physics C, **40**, 100001 (2016). <https://doi.org/10.1088/1674-1137/40/10/100001>
- [33] M. Abu-Shady, M.K.A. Kaabar, Computational and Mathematical Methods in Medicine, **2022**, 2138775, (2022). <https://doi.org/10.1155/2022/2138775>

МАСИ ВАЖКОГО ТА ВАЖКОГО-ЛЕГКОГО МЕЗОНУ В РАМКАХ ТРИГОНОМЕТРИЧНОГО ПОТЕНЦІАЛУ РОЗЕНА-МОРЗЕ З ВИКОРИСТАННЯМ УЗАГАЛЬНЕНОЇ ДРОБОВОЇ ПОХІДНОЇ

Мохамед Абу-Шаді^a, Етідо П. Іньянг^b

^aФакультет математики та інформатики, факультет природничих наук, Університет Менуфія, Єгипет

^bФакультет фізики, Національний відкритий університет Нігерії, Джабі, Абуджа, Нігерія

Тригонометричний потенціал Розена-Морзе використовується як потенціал мезонної взаємодії. Для аналітичного вирішення N-радіального дробового рівняння Шредінгера використовується розширений метод Нікіфорова-Уварова. Використовуючи узагальнену дробову похідну, власні значення енергії отримують у дробовій формі. Сучасні результати використовуються для розрахунку мас мезонів, таких як чармоній, боттоніум і важкі-легкі мезони. Поточні висновки перевершують результати інших недавніх досліджень і показують хорошу узгодженість з експериментальними даними, тому фракційний параметр є вирішальним для оптимізації мас мезонів.

Ключові слова: тригонометричний потенціал Розена-Морзе, розширений метод Нікіфорова-Уварова, узагальнена дробова похідна

ANALYTICAL SOLUTIONS TO THE SCHRÖDINGER EQUATION WITH COLLECTIVE POTENTIAL MODELS: APPLICATION TO QUANTUM INFORMATION THEORY[†]

✉ **Funmilayo Ayedun**, ✉ **Etido P. Inyang**, **Efiong A. Ibanga**, **Kolawole M. Lawal**

Department of Physics, National Open University of Nigeria, Jabi, Abuja

Corresponding Author: etidophysics@gmail.com, einyang@noun.edu.ng

Received October 15, 2022; revised November 11, 2022; accepted November 14, 2022

In this study, the energy equation and normalized wave function were obtained by solving the Schrödinger equation analytically utilizing the Eckart-Hellmann potential and the Nikiforov-Uvarov method. Fisher information and Shannon entropy were investigated. Our results showed higher-order characteristic behavior for position and momentum space. Our numerical results showed an increase in the accuracy of the location of the predicted particles occurring in the position space. Also, our results show that the sum of the position and momentum entropies satisfies the lower-bound Berkner, Bialynicki-Birula, and Mycielski inequality and Fisher information was also satisfied for the different eigenstates. This study's findings have applications in quantum chemistry, atomic and molecular physics, and quantum physics.

Keywords: Schrödinger equation; Eckart-Hellmann potential; Fisher information; Shannon entropy; Nikiforov-Uvarov method

PACS: 03.65.-w, 03.67.-a

1. Introduction

With various analytical techniques, such as the Nikiforov-Uvarov (NU) method [1-10], the asymptotic iterative method (AIM) [11], the supersymmetric quantum mechanics method (SUSQM) [12], the Nikiforov-Uvarov functional analysis (NUFA) method [13-16], the series expansion method [17-21], the WKB approximation [22-24], and so on [25], the Schrödinger equation (SE) can be solved for a variety of potentials. Our knowledge of the underlying cause of a quantum system is significantly influenced by the analytical solutions to this equation with a physical potential. This is due to the fact that the eigenvalues and eigenfunctions convey essential information about the quantum system under investigation [26, 27]. However, the exact bound state solutions of the SE are possible in some cases [28]. One can solve the SE using appropriate approximation approaches, such as the Pekeris, Greene and Aldrich, and others [29–31], to obtain the approximate solutions when the arbitrary angular momentum quantum number is not equal to zero. The eigenvalues and eigenfunctions are of great importance in the study of mass spectra of heavy mesons [32], thermodynamic properties of the system [33], and the quantum theoretic information entropies [34] among others. According to the fundamental principle of information theory put forward by Claude Shannon, the global measures of Shannon entropy and Fisher information are crucial to quantum information-theoretic measures [36]. As a result of its numerous applications in physics and chemistry, scientists have actively investigated Shannon and Fisher entropies in various fields in recent years. The theory of communication is one field in which Shannon and Fisher entropies are applied [37,38]. The theoretical foundation of Fisher information was obtained much earlier [39], but the application was unknown until Sear et al., [40], found a link between Fisher information and the kinetic energy of a quantum system. The significance of the global measure is to investigate the uncertainty associated with the probability distribution [41,42]. The position and momentum spaces of the Shannon entropy have an entropic relation derived by Berkner, Bialynicki-Birula and Mycielski [43] and expressed as $s_r + s_p \geq D(1 + \ln\pi)$, where D is the spatial dimension. In view of this, many scholars have studied the Shannon and Fisher entropies [44-46], for instance, Edet et al., [47] used a class of Yukawa potential to study the global quantum information-theoretic measurements in the presence of magnetic and Aharanov-Bohm (AB) fields. Also, Olendski [48] used the quadratic and inverse quadratic dependencies on the radius to study the Shannon quantum information entropies, Fisher information, and Onicescu energies and complexities in the position and momentum spaces for the azimuthally symmetric two-dimensional nano-ring that is placed into the combination of the transverse uniform magnetic field and the AB flux. For time-dependent harmonic vector potential. Onate et al. [49] found the exact solution to the Feinberg-Horodecki equation. Explicitly, the quantized momentum and its corresponding un-normalized wave functions were obtained. Using the Hellman-Feynman theory, expectation values of time and momentum were used to determine the Fisher information (for time and momentum) and variance (for time and momentum). Also, Under the influence of an improved expression for the Wei potential energy function, Onate et al., [50] obtained an approximate solution of the one-dimensional Klein-Gordon equation. By using specific mappings, it was possible to derive the solution of the SE from that of the Klein-Gordon equation. The computation of expectation values was used to study the Fisher information for position space and momentum space. Furthermore, Onate et al., [51] obtained an approximate bound state solution of the three-dimensional SE for a potential family together with the corresponding

[†] **Cite as:** F. Ayedun, E.P. Inyang, E.A. Ibanga, and K.M. Lawal, East Eur. J. Phys. 4, 87 (2022), <https://doi.org/10.26565/2312-4334-2022-4-07>
© F. Ayedun, E.P. Inyang, E.A. Ibanga, K.M. Lawal, 2022

wave function, after which the Fisher information for a potential family was explicitly obtained via the methodology of expectation value and the radial expectation value. Also, some uncertainty relations that are closely related to Heisenberg-like uncertainty were obtained and numerical results were generated to justify the relations and inequalities. Onate et al., [52], obtained the solutions of the SE with Tietz-Hua potential using the Parametric NU method. The Shannon entropy and information energy were computed. Idiodi and Onate [53] studied the Shannon and Renyi information entropy for both position and momentum space and the Fisher information for the position-dependent mass SE with the Frost-Musulin potential. Onate et al [54], solved the approximate analytical solution of the SE in the framework of the parametric NU method with a hyperbolic exponential-type potential. Using the integral method, the Shannon entropy, information energy, Fisher information, and complexity measures were calculated. Edet et al., [55], investigated quantum information by a theoretical measurement approach of an Aharonov-Bohm (AB) ring with Yukawa interaction in curved space with disclination. They obtained the Shannon entropy through the eigenfunctions of the system. Ikot et al., [56] solved the SE for the Mobius square potential using the NUFA method. The Shannon entropy, Fisher information, Fisher-Shannon product and the expectation values for the Mobius square were investigated in position and momentum space. Amadi et al. [57] solved the SE with screened Kratzer potential to study the Shannon entropy and Fisher information. Their results showed that the sum of the position and momentum entropies satisfies the lower-bound Berkner, Bialynicki-Birula and Mycielski inequality. Ikot et al., [58], solved the approximate solutions of the SE with the generalized Hulthen and Yukawa potential within the framework of the functional method. The obtained wave function and the energy levels are used to study the Shannon entropy, Renyi entropy, Fisher information, Shannon-Fisher complexity, Shannon power and Fisher-Shannon product in both position and momentum spaces for the ground and first excited states. Ikot et al. [59], studied the Shannon entropy and the Fisher Information entropies were investigated for a generalized hyperbolic potential in position and momentum spaces through the solutions of SE using the NUFA method. The position and momentum spaces for Shannon entropy and the Fisher Information entropies were calculated numerically.

Eckart potential [60], was proposed in 1930, and its application cut across molecular physics and other related areas. Numerous authors in the references [61–63] took into consideration the bound state solutions for this potential. Numerous scholars have extensively used the Hellmann potential [64] to obtain bound-state solutions in studying the condensed matter, atomic, nuclear, and particle physics [65–69]. Recently, a lot of scholars have expressed interest in the pairing of at least two potentials. The main goal of combining at least two physical potential models is to include additional physical applications and comparative analysis with previous studies [58,70,71]. Inyang et al.,[70] proposed Eckart and Hellmann potential (EHP) to study selected diatomic molecules. Furthermore, they adopted the potential to study the mass spectra and thermal properties of heavy mesons [71]. In this research, we aim at obtaining the approximate bound state analytical solutions to the SE with the Eckart plus Hellmann potential (EHP) using the NU method. The obtained energy eigenvalues and eigenfunctions will be applied to study the Shannon entropy and Fisher information. The combined potential takes the form [60,64].

$$V(r) = -\frac{A_0 e^{-\alpha r}}{1 - e^{-\alpha r}} + \frac{A_1 e^{-\alpha r}}{(1 - e^{-\alpha r})^2} - \frac{A_2}{r} + \frac{A_3 e^{-\alpha r}}{r}, \tag{1}$$

where $A_0, A_1, A_2,$ and A_3 are the strength of the potential, α is the screening parameter and r is inter-particle distance.

This paper is organized as follows: In Sect. 2 we solve the Schrödinger equation with the Eckart plus Hellmann potential to obtain the energy equation and normalized wave function. In Sect. 3, the derived eigenfunctions will be used to obtain the numerical computation of the Shannon entropy and Fisher information. In Sect. 3, we present the results and discussion. Conclusions are given in Sect. 4.

2. Analytical solutions of the Schrödinger equation with Eckart plus Hellmann potential

In this study, we adopt the NU method [1] which is based on solving the second-order differential equation of the hypergeometric type. The details can be found in Appendix A. The Schrödinger equation of a quantum physical system is characterized by a given potential $V(r)$ takes the form [72,73]

$$\frac{d^2 W(r)}{dr^2} + \left[\frac{2\mu}{\hbar^2} (E_{nl} - V(r)) - \frac{l(l+1)}{r^2} \right] W(r) = 0 \tag{2}$$

E_{nl} is the energy eigenvalues of the quantum system, l is the angular momentum quantum number, μ is the reduced mass of the system, \hbar is the reduced Planck's constant and r is the radial distance from the origin.

Equation (2) cannot be exactly solved using the adopted potential. To deal with the centrifugal barrier, we thus employ an approximation approach suggested by Greene-Aldrich [29]. This approximation is a good approximation to the centrifugal term which is valid for $\alpha \ll 1$, and it becomes

$$\frac{1}{r^2} \approx \frac{\alpha^2}{(1 - e^{-\alpha r})^2}. \tag{3}$$

Substituting Eqs. (1) and (3) into Eq. (2), Eq. (4) is obtained as

$$\frac{d^2W(r)}{dr^2} + \left[\frac{2\mu}{\hbar^2} \left(E_{nl} - \frac{A_0 e^{-ar}}{1 - e^{-ar}} - \frac{A_1 e^{-ar}}{(1 - e^{-ar})^2} + \frac{A_2 \alpha}{1 - e^{-ar}} - \frac{A_3 e^{-ar}}{1 - e^{-ar}} \right) + \frac{l(l+1)\alpha^2}{(1 - e^{-ar})^2} \right] W(r) = 0, \quad (4)$$

By using the change of variable from r to s , our new coordinate becomes

$$s = e^{-ar}. \quad (5)$$

We substitute Eq. (5) into Eq. (4) and after some simplifications; Eq. (6) is gotten as

$$\frac{d^2W(s)}{ds^2} + \frac{1-s}{s(1-s)} \frac{dW(s)}{ds} + \frac{1}{s^2(1-s)^2} \left[-(\varepsilon + \beta_3)s^2 + (2\varepsilon - \beta_0 - \beta_1 - \beta_2 - \beta_3)s - (\varepsilon - \beta_0 - \beta_2 + \gamma) \right] W(s) = 0, \quad (6)$$

where

$$-\varepsilon = \frac{2\mu E_{nl}}{\alpha^2 \hbar^2}, \quad \beta_0 = \frac{2\mu A_0}{\alpha^2 \hbar^2}, \quad \beta_1 = \frac{2\mu A_1}{\alpha^2 \hbar^2}, \quad \beta_2 = \frac{2\mu A_2}{\alpha \hbar^2}, \quad \beta_3 = \frac{2\mu A_3}{\alpha \hbar^2}, \quad \gamma = l(l+1). \quad (7)$$

Comparing Eq. (6) with Eq. (A1) we obtain the following parameters

$$\left. \begin{aligned} \tilde{\tau}(s) &= 1-s, \quad \sigma(s) = s(1-s), \quad \sigma'(s) = 1-2s \\ \tilde{\sigma}(s) &= -(\varepsilon + \beta_3)s^2 + (2\varepsilon - \beta_0 - \beta_1 - \beta_2 - \beta_3)s - (\varepsilon - \beta_0 - \beta_2 + \gamma) \end{aligned} \right\}. \quad (8)$$

Substituting Eq. (8) into Eq.(A9) we have

$$\pi(s) = -\frac{s}{2} \pm \sqrt{(P_0 - k)s^2 + (R_0 + k)s + Q_0}, \quad (9)$$

where

$$\left. \begin{aligned} P_0 &= \frac{1}{4} + \varepsilon + \beta_3, \quad R_0 = -(2\varepsilon - \beta_0 - \beta_1 - \beta_2 - \beta_3) \\ Q_0 &= \varepsilon - \beta_0 - \beta_2 + \gamma \end{aligned} \right\}. \quad (10)$$

To find the constant k , the discriminant of the expression under the square root of Eq. (9) must be equal to zero. As such we have that

$$k_- = -(\beta_1 - \beta_0 - \beta_2 + \beta_3 + 2\gamma) - 2\sqrt{\varepsilon - \beta_0 - \beta_2 + \gamma} \sqrt{\frac{1}{4} + \gamma + \beta_1} \quad (11)$$

Substituting Eqs. (10) and (11) in Eq. (9) we have

$$\pi_-(s) = -\frac{s}{2} - \left[\left(\sqrt{\varepsilon - \beta_0 - \beta_2 + \gamma} + \sqrt{\frac{1}{4} + \gamma + \beta_1} \right) s - \sqrt{\varepsilon - \beta_0 - \beta_2 + \gamma} \right]. \quad (12)$$

Differentiating Eq. (12) gives

$$\pi'_-(s) = -\frac{1}{2} - \left(\sqrt{\varepsilon - \beta_0 - \beta_2 + \gamma} + \sqrt{\frac{1}{4} + \gamma + \beta_1} \right). \quad (13)$$

Substituting Eqs. (11) and (13) into Eq.(A10) gives

$$\lambda = \beta_0 - \beta_1 + \beta_2 - \beta_3 - 2\gamma - 2\sqrt{\varepsilon - \beta_0 - \beta_2 + \gamma} \sqrt{\frac{1}{4} + \gamma + \beta_1} - \frac{1}{2} - \left(\sqrt{\varepsilon - \beta_0 - \beta_2 + \gamma} + \sqrt{\frac{1}{4} + \gamma + \beta_1} \right). \quad (14)$$

With $\tau(s)$ being obtained from Eq.(A7) as

$$\tau(s) = 1 - 2s - 2\sqrt{\varepsilon - \beta_0 - \beta_2 + \gamma} s - 2\sqrt{\frac{1}{4} + \gamma + \beta_1} s + 2\sqrt{\varepsilon - \beta_0 - \beta_2 + \gamma}. \quad (15)$$

Differentiating Eq. (15) yields

$$\tau'(s) = -2 - 2 \left(\sqrt{\varepsilon - \beta_0 - \beta_2 + \gamma} + \sqrt{\frac{1}{4} + \gamma + \beta_1} \right). \quad (16)$$

And also taking the derivative of $\sigma'(s)$ with respect to s from Eq. (8), we have

$$\sigma''(s) = -2. \tag{17}$$

Substituting Eqs.(16) and (17) into Eq.(A11) and simplifying, yields

$$\lambda_n = n^2 + n + 2n\sqrt{\varepsilon - \beta_0 - \beta_2 + \gamma} + 2n\sqrt{\frac{1}{4} + \gamma + \beta_1}. \tag{18}$$

Equating Eqs. (14) and (18) and substituting Eq. (7) yields the energy eigenvalues equation of the Eckart plus Hellmann potential as

$$E_{nl} = \frac{\alpha^2 \hbar^2 (l+l^2)}{2\mu} - A_0 - A_2 \alpha - \frac{\hbar^2 \alpha^2}{8\mu} \left[\frac{\left(n + \frac{1}{2} + \sqrt{\left(\frac{1}{4} + l\right)^2 + \frac{2A_1\mu}{\alpha^2 \hbar^2}} \right)^2 - \frac{2A_0\mu}{\alpha^2 \hbar^2} + \frac{2A_1\mu}{\alpha^2 \hbar^2} - \frac{2A_2\mu}{\alpha \hbar^2} + \frac{2A_3\mu}{\alpha \hbar^2} + (l+l^2)}{n + \frac{1}{2} + \sqrt{\left(\frac{1}{4} + l\right)^2 + \frac{2A_1\mu}{\alpha^2 \hbar^2}}} \right]^2. \tag{19}$$

2.1. Special cases

1. We set $A_0 = A_1 = 0$ and obtain the energy eigenvalues for Hellmann potential

$$E_{nl} = \frac{\alpha^2 \hbar^2 (l+l^2)}{2\mu} - A_2 \alpha - \frac{\hbar^2 \alpha^2}{8\mu} \left[\frac{\left(n + \frac{1}{2} + \sqrt{\left(\frac{1}{4} + l\right)^2} \right)^2 - \frac{2A_2\mu}{\alpha \hbar^2} + \frac{2A_3\mu}{\alpha \hbar^2} + (l+l^2)}{n + \frac{1}{2} + \sqrt{\left(\frac{1}{4} + l\right)^2}} \right]^2. \tag{20}$$

2. We set $A_2 = A_3 = 0$ and obtain the energy eigenvalues for Eckart potential

$$E_{nl} = \frac{\alpha^2 \hbar^2 (l+l^2)}{2\mu} - A_0 - \frac{\hbar^2 \alpha^2}{8\mu} \left[\frac{\left(n + \frac{1}{2} + \sqrt{\left(\frac{1}{4} + l\right)^2 + \frac{2A_1\mu}{\alpha^2 \hbar^2}} \right)^2 - \frac{2A_0\mu}{\alpha^2 \hbar^2} + \frac{2A_1\mu}{\alpha^2 \hbar^2} + (l+l^2)}{n + \frac{1}{2} + \sqrt{\left(\frac{1}{4} + l\right)^2 + \frac{2A_1\mu}{\alpha^2 \hbar^2}}} \right]^2. \tag{21}$$

3. We set $A_0 = A_1 = A_3 = \alpha = 0$ and obtain the energy eigenvalues for Coulomb potential

$$E_{nl} = -\frac{\mu A_2^2}{2\hbar^2 (n+l+1)^2}. \tag{22}$$

4. We set $A_0 = A_1 = A_2 = 0$ and obtain the energy eigenvalues for Yukawa potential

$$E_{nl} = \frac{\alpha^2 \hbar^2 (l+l^2)}{2\mu} - \frac{\hbar^2 \alpha^2}{8\mu} \left[\frac{\left(n + \frac{1}{2} + \sqrt{\left(\frac{1}{4} + l\right)^2} \right)^2 + \frac{2A_3\mu}{\alpha \hbar^2} + (l+l^2)}{n + \frac{1}{2} + \sqrt{\left(\frac{1}{4} + l\right)^2}} \right]^2. \tag{23}$$

2.2. Wave function

To obtain the corresponding wavefunction, we consider Eqs. (A4) and (A6) and upon substituting Eqs. (8) and (15) and integrating, we get

$$\phi(s) = s^{\sqrt{\varepsilon - \beta_0 - \beta_2 + \gamma}} (1-s)^{\frac{1}{2} + \sqrt{\frac{1}{4} + \gamma + \beta_1}}, \tag{24}$$

$$\rho(s) = s^{2\sqrt{\varepsilon - \beta_0 - \beta_2 + \gamma}} (1-s)^{2\sqrt{\frac{1}{4} + \gamma + \beta_1}}. \quad (25)$$

Equation 25 is known as the weight function.

By substituting Eqs. (8) and (25) into Eq. (A5) we obtain the Rodrigue's equation as

$$y_n(s) = B_{nl} s^{-2\sqrt{\varepsilon - \beta_0 - \beta_2 + \gamma}} (1-s)^{-2\sqrt{\frac{1}{4} + \gamma + \beta_1}} \frac{d^n}{ds^n} \left[s^{n+2\sqrt{\varepsilon - \beta_0 - \beta_2 + \gamma}} (1-s)^{n+2\sqrt{\frac{1}{4} + \gamma + \beta_1}} \right], \quad (26)$$

where B_{nl} is normalization constant.

Equation (26) is equivalent to

$$P_n^{(2\sqrt{\varepsilon - \beta_0 - \beta_2 + \gamma}, 2\sqrt{\frac{1}{4} + \gamma + \beta_1})} (1-2s), \quad (27)$$

where $P_n^{(\alpha, \beta)}$ is Jacobi Polynomial

The wave function is given by

$$\psi_{nl}(s) = B_{nl} s^{\sqrt{\varepsilon - \beta_0 - \beta_2 + \gamma}} (1-s)^{\frac{1}{2} + \sqrt{\frac{1}{4} + \gamma + \beta_1}} P_n^{(2\sqrt{\varepsilon - \beta_0 - \beta_2 + \gamma}, 2\sqrt{\frac{1}{4} + \gamma + \beta_1})} (1-2s). \quad (28)$$

Using the normalization condition, we obtain the normalization constant as follows

$$\int_0^1 |\psi_{nl}(r)|^2 dr = 1. \quad (29)$$

From our coordinate transformation of Eq. (5), we have that

$$-\frac{1}{\alpha s} \int_1^0 |\psi_{nl}(s)|^2 ds = 1. \quad (30)$$

By letting, $y = 1 - 2s$, we have

$$\frac{B_{nl}^2}{\alpha} \int_{-1}^1 \left(\frac{1-y}{2} \right)^{2\sqrt{\varepsilon + \beta_0 - \beta_1 + \gamma}} \left(\frac{1+y}{2} \right)^{1+2\sqrt{\frac{1}{4} + \gamma}} \left[P_n^{(2\sqrt{\varepsilon + \beta_0 - \beta_1 + \gamma}, 2\sqrt{\frac{1}{4} + \gamma})} y \right]^2 dy = 1. \quad (31)$$

Let

$$\left. \begin{aligned} \eta &= 1 + 2\sqrt{\frac{1}{4} + \gamma}, \quad \eta - 1 = 2\sqrt{\frac{1}{4} + \gamma} \\ u &= 2\sqrt{\varepsilon + \beta_0 - \beta_1 + \gamma} \end{aligned} \right\}. \quad (32)$$

Substituting Eq. (32) into Eq. (31) we have

$$\frac{B_{nl}^2}{\alpha} \int_{-1}^1 \left(\frac{1-y}{2} \right)^{\eta} \left(\frac{1+y}{2} \right)^{\eta} \left[P_n^{(2u, \mu-1)} y \right]^2 dy = 1. \quad (33)$$

According to Ebomwonyi et al. [74], integral of the form in Eq.(33) can be expresses as

$$\int_{-1}^1 \left(\frac{1-p}{2} \right)^x \left(\frac{1+p}{2} \right)^y \left[P_n^{(2x, 2y-1)} p \right]^2 dp = \frac{2\Gamma(x+n+1)\Gamma(y+n+1)}{n!x\Gamma(x+y+n+1)}. \quad (34)$$

Hence, comparing Eq. (33) with the standard integral of Eq.(34), we obtain the normalization constant as

$$B_{nl} = \sqrt{\frac{n! \alpha \Gamma(u+\eta+n+1)}{2\Gamma(u+n+1)\Gamma(\eta+n+1)}}. \quad (35)$$

2.3. Shannon Entropy for the Eckart plus Hellmann potential

Entropy is a thermodynamic quantity representing the unavailability of a systems thermal energy for conversion into mechanical work [53]. The Shannon entropy is defined in position and momentum spaces as [75]

$$S_r = -\int_c^p \rho(r) \ln \rho(r) dr, \tag{36}$$

and

$$S_p = -\int_c^p \rho(p) \ln \rho(p) dp, \tag{37}$$

where S_r is the position space Shannon entropy, S_p is the momentum space Shannon entropy,

$$\rho(r) = |\psi(r)|^2, \tag{38}$$

and

$$\rho(p) = |\psi(p)|^2, \tag{39}$$

are the probability densities in the position and momentum spaces, respectively. $\psi(p)$ is the wave function in the momentum coordinate obtained by the Fourier transform of $\psi(r)$. The Shannon entropic uncertainty relation proposed by Beckner, Bialynicki-Birula and Mycielski (BBM) takes the form [43]

$$S_T = S_r + S_p \geq D(1 + \ln \pi), \tag{40}$$

where D is the spatial dimension.

The probability density's logarithmic functional measure of randomness and uncertainty in a particle's spatial localization is called Shannon entropy. The lower this entropy, the more concentrated is the wave function, the smaller the uncertainty and the higher is the accuracy in predicting the localization of the particle [74].

Using Eqs. (28) and (35) we obtained the total wavefunction as

$$\psi_{nl}(s) = \sqrt{\frac{n! u \alpha \Gamma(u + \eta + n + 1)}{2\Gamma(u + n + 1)\Gamma(\eta + n + 1)}} e^{-ar\sqrt{\varepsilon - \beta_0 - \beta_2 + \gamma}} (1 - e^{-ar})^{\frac{1}{2} + \sqrt{\frac{1}{4} + \gamma + \beta_1}} P_n^{(2\sqrt{\varepsilon - \beta_0 - \beta_2 + \gamma}, 2\sqrt{\frac{1}{4} + \gamma + \beta_1})} (1 - 2e^{-ar}). \tag{41}$$

The normalized wave function for two low lying states $n = 0, 1$ is given as

$$\psi_0(s) = \sqrt{\frac{u \alpha \Gamma(u + \eta + 1)}{2\Gamma(u + 1)\Gamma(\eta + 1)}} e^{-ar\sqrt{\varepsilon - \beta_0 - \beta_2 + \gamma}} (1 - e^{-ar})^{\frac{1}{2} + \sqrt{\frac{1}{4} + \gamma + \beta_1}}, \tag{42}$$

and

$$\psi_1(s) = \frac{1}{1 + 2(\varepsilon - \beta_0 - \beta_2 + \gamma)} \sqrt{\frac{u \alpha (1 + 2(\varepsilon - \beta_0 - \beta_2 + \gamma)) \Gamma(u + \eta + 2)}{(1 + (\varepsilon - \beta_0 - \beta_2 + \gamma)) 2\Gamma(u + n + 1)\Gamma(\eta + n + 1)}} e^{-ar\sqrt{\varepsilon - \beta_0 - \beta_2 + \gamma}} (1 - e^{-ar})^{\frac{1}{2} + \sqrt{\frac{1}{4} + \gamma + \beta_1}} (1 - 2e^{-ar}), \tag{43}$$

where $\Gamma(x)$ is the gamma function given as $\Gamma(x) = \int_0^\infty t^{x-1} e^{-t} dt$ [76].

The corresponding normalized wave function in the momentum space for two low lying states $n = 0, 1$ is obtained as [77]

$$\psi_0(p) = \frac{1}{\sqrt{2\pi}} \int_0^\infty \psi_0(r) e^{-ipr} dr, \tag{44}$$

$$\psi_0(p) = \sqrt{\frac{u \alpha \Gamma(u + \eta + 1)}{2\Gamma(u + 1)\Gamma(\eta + 1)}} \frac{\Gamma\left(\frac{ip}{\alpha} + \varepsilon - \beta_0 - \beta_2 + \gamma\right) \Gamma(1 + \varepsilon - \beta_0 - \beta_2 + \gamma)}{\sqrt{2\pi} \alpha \Gamma\left(1 + \frac{ip}{\alpha} + \varepsilon - \beta_0 - \beta_2 + \gamma\right)}, \tag{45}$$

$$\psi_1(p) = \frac{1}{\sqrt{2\pi}} \int_0^\infty \psi_1(r) e^{-ipr} dr, \tag{46}$$

$$\psi_1(p) = \sqrt{\frac{u\alpha(1+2(\varepsilon-\beta_0-\beta_2+\gamma))\Gamma(u+\eta+2)}{(2(\varepsilon-\beta_0-\beta_2+\gamma))2\Gamma(u+n+1)\Gamma(\eta+n+1)}} \left(\begin{array}{c} (-2ip + \alpha(1+2(\varepsilon-\beta_0-\beta_2+\gamma))) \\ \Gamma\left(\frac{ip}{\alpha} + \varepsilon - \beta_0 - \beta_2 + \gamma\right) \\ \sqrt{2\pi\alpha^2(1+2(\varepsilon-\beta_0-\beta_2+\gamma))} \\ \Gamma\left(2 + \frac{ip}{\alpha} + \varepsilon - \beta_0 - \beta_2 + \gamma\right) \end{array} \right). \tag{47}$$

2.4. Fisher Information theory for the Eckart plus Hellmann potential

We examine the Fisher information in position and momentum spaces. Fisher information is the sole component of the local measure, and is mainly concerned with local changes that occur in probability density [57,78]. Density functional is important for the investigation of Fisher information [79]. It is stated as:

$$I_r = \int \frac{|\rho'(r)|^2}{\rho(r)} dr = 4 \int |\psi'(r)|^2 dr = 4\langle p^2 \rangle - 2(2l+1)|m|\langle r^{-2} \rangle, \tag{48}$$

$$I_p = \int \frac{|\rho'(p)|^2}{\rho(p)} dp = 4 \int |\psi'(p)|^2 dp = 4\langle r^2 \rangle - 2(2l+1)|m|\langle p^{-2} \rangle. \tag{49}$$

Fisher information inequality becomes [80]

$$I_r I_p \geq 9 \left[2 - \frac{2l+1}{l(l+1)} |m| \right]^2 \geq 36. \tag{50}$$

We solve Eqs. (48) and (49) numerically, which are complicated to solve analytically due to the form of the integral.

3. RESULTS AND DISCUSSION

In this section, we will discuss our numerical results. For both cases, the screening criterion was set to $0.1 \leq \alpha \leq 0.9$. These parameters were selected in order to compare results [57].

Our results were obtained numerically. Fisher information and Shannon entropy give important details about the precision and degree of uncertainty in particle localization predictions. Lower Shannon entropy denotes greater stability, higher localization, and reduced uncertainty. The kinetic energy and Fisher information are related, and more Fisher information indicates greater localization and energy fluctuation. For the various values of α , the numerical results for Shannon entropy and Fisher information are shown in Tables 1 and 2, respectively.

Table 1. Numerical values of Shannon entropy for Eckart plus Hellmann potential

n	α	S_r	S_p	S_T
0	0.1	5.78107	0.692356	6.4734260
	0.2	5.97095	0.498294	6.4692440
	0.3	6.20766	0.267158	6.4748180
	0.4	6.49426	-0.017446	6.4768131
	0.5	6.85881	-0.378718	6.4800920
	0.6	7.34806	-0.856921	6.4911890
	0.7	8.03556	-1.529530	6.5060300
	0.8	9.09978	-2.571370	6.5284100
	0.9	11.0879	-4.524130	6.5637700
1	0.1	9.67144	-2.915280	6.7561600
	0.2	11.7253	-5.091890	6.6334100
	0.3	11.4772	-4.873510	6.6036900
	0.4	8.71251	-2.048560	6.6639500
	0.5	7.39803	-0.709438	6.6885920
	0.6	6.50485	-0.198122	6.3067280
	0.7	5.82308	0.887327	6.7104070
	0.8	5.26825	1.445710	6.7139600
	0.9	4.80376	1.914240	6.7180000

The Shannon entropy values show a decreasing order in the position space, which signifies a lower uncertainty and higher accuracy in predicting localization and the stability. This is complimented in the momentum space by an increasing Shannon entropy. For $n = 1$, it increased and decreased afterward. This similar behavior is also observed in the momentum

spaces. Negative values mean that the Shannon entropy is highly localized [57]. The numerical analysis of Fisher information for $n = 0$ and $n = 1$ is shown in Table 2. Similar phenomena are seen in momentum spaces as well and negative values indicate a strongly localized Shannon entropy. Table 2 displays the numerical analysis of Fisher information for $n = 0$ and $n = 1$ indicating ground and first excited states respectively. Here, there was a similar pattern of behavior, and the alternative increase and decrease for $n = 1$ are noticed. The increasing Fisher information observed in these different states implies an increasing localization. In both cases, the Shannon entropy uncertainty relation condition is satisfied as seen in Eq. (40) and Fisher uncertainty relation is satisfied as seen in Eq. (50).

Table 2. Numerical values of Fisher information for Eckart plus Hellmann potential

n	α	I_r	I_p	$I_r I_p$
0	0.1	1.195670	33.4215	39.96108
	0.2	1.052470	38.0402	40.03616
	0.3	0.903119	44.4792	40.17001
	0.4	0.748496	54.0185	40.43263
	0.5	0.590304	69.2190	40.86025
	0.6	0.431695	96.4388	41.63214
	0.7	0.278445	154.136	42.91839
	0.8	0.141132	318.584	44.96239
	0.9	0.038628	1212.07	46.81983
1	0.1	0.137107	465.101	63.76860
	0.2	0.032212	1782.30	57.41144
	0.3	0.037720	1516.76	57.21218
	0.4	0.251035	241.175	60.54336
	0.5	0.606999	100.787	61.17761
	0.6	1.108780	55.6926	61.75084
	0.7	1.753940	35.4030	62.09332
	0.8	2.542350	24.5121	62.31833
	0.9	3.473940	17.9847	62.47776

4. CONCLUSION

In this research, the Schrödinger equation is solved with the Eckart plus Hellmann potential to obtain the energy equation and normalized wave function. We studied the characteristic properties of Shannon entropy and Fisher information for the position and momentum spaces for ground state and first excited state. Our results were presented numerically. We observed a similar behavior for Shannon entropy and Fisher information values. This behavior is related to the probability density distribution's concentration. Our findings showed that several eigenstates had negative values in the position space. This implies a higher localization for the collective potential models. The potential models also show increasing accuracy in predicting particle localization in the position space of Shannon entropy and Fisher information. This research can be extended to other global measures, such as Renyi entropy, Tsallis entropy etc.

Acknowledgement

The authors would like to thank the National Open University of Nigeria for the award of the Senate Research Grant. Also, thanked the referees for making impactful observations that lead to the improvement of the manuscript.

Funding.

The research was carried out under the National Open University of Nigeria Senate Research Grant: NOUN/DRA/LARTL/GN0026/VOL II.

Authors Contributions.

FA and EPI conceived and designed the study, acquired, analyzed and interpreted the data and handled the review; EAI and KML handled the computational analysis. All authors read and approved the final manuscript.

Competing interests.

The authors declare that they have no competing interests.

APPENDIX A

Review of Nikiforov-Uvarov (NU) method

The NU method was proposed by Nikiforov and Uvarov [1] to transform Schrödinger-like equations into a second-order differential equation via a coordinate transformation $s = s(r)$, of the form

$$\psi''(s) + \frac{\tilde{\tau}(s)}{\sigma(s)}\psi'(s) + \frac{\tilde{\sigma}(s)}{\sigma^2(s)}\psi(s) = 0, \tag{A1}$$

where $\tilde{\sigma}(s)$, and $\sigma(s)$ are polynomials, at most second degree and $\tilde{\tau}(s)$ is a first-degree polynomial. The exact solution of Eq.(A1) can be obtained by using the transformation.

$$\psi(s) = \phi(s)y(s). \quad (\text{A2})$$

This transformation reduces Eq.(A1) into a hypergeometric-type equation of the form

$$\sigma(s)y''(s) + \tau(s)y'(s) + \lambda y(s) = 0. \quad (\text{A3})$$

The function $\phi(x)$ can be defined as the logarithm derivative

$$\frac{\phi'(s)}{\phi(s)} = \frac{\pi(s)}{\sigma(s)}. \quad (\text{A4})$$

With $\pi(s)$ being at most a first-degree polynomial. The second part of $\psi(s)$ being $y(s)$ in Eq. (A2) is the hypergeometric function with its polynomial solution given by Rodrigues relation as

$$y(s) = \frac{B_{nl}}{\rho(s)} \frac{d^n}{ds^n} \left[\sigma^n(s) \rho(s) \right], \quad (\text{A5})$$

where B_{nl} is the normalization constant and $\rho(s)$ the weight function which satisfies the condition below;

$$(\sigma(s)\rho(s))' = \tau(s)\rho(s), \quad (\text{A6})$$

where also

$$\tau(s) = \tilde{\tau}(s) + 2\pi(s). \quad (\text{A7})$$

For bound solutions, it is required that

$$\tau'(s) < 0. \quad (\text{A8})$$

The eigenfunctions and eigenvalues can be obtained using the definition of the following function $\pi(s)$ and parameter λ , respectively:

$$\pi(s) = \frac{\sigma'(s) - \tilde{\tau}(s)}{2} \pm \sqrt{\left(\frac{\sigma'(s) - \tilde{\tau}(s)}{2} \right)^2 - \tilde{\sigma}(s) + k\sigma(s)}, \quad (\text{A9})$$

and

$$\lambda = k_- + \pi'_-(s). \quad (\text{A10})$$

The value of k can be obtained by setting the discriminant in the square root in Eq. (A9) equal to zero. As such, the new eigenvalues equation can be given as

$$\lambda + n\tau'(s) + \frac{n(n-1)}{2}\sigma''(s) = 0, (n = 0, 1, 2, \dots). \quad (\text{A11})$$

ORCID IDs

© Funmilayo Ayedun, <https://orcid.org/0000-0001-5421-9305>; © Etido P. Inyang, <https://orcid.org/0000-0002-5031-3297>

REFERENCES

- [1] S.K. Nikiforov, and V.B. Uvarov, *Special functions of mathematical Physics*, (Birkhauser, Basel, 1988)
- [2] P.O. Okoi, C.O. Edet, T.O. Magu and E.P. Inyang, "Eigensolution and Expectation values of the Hulthén and Generalized Inverse Quadratic Yukawa potential", *Jordan Journal of Physics*, **15**, 137 (2022). <https://doi.org/10.47011/15.2.4>
- [3] I.O. Akpan, E.P. Inyang, E.P. Inyang, and E.S. William, "Approximate solutions of the Schrödinger equation with Hulthén-Hellmann Potentials for a Quarkonium system", *Rev. Mex. Fis.* **67**, 490 (2021). <https://doi.org/10.31349/RevMexFis.67.482>
- [4] E.S. William, E.P. Inyang, and E.A. Thompson, "Arbitrary ℓ -solutions of the Schrödinger equation interacting with Hulthén-Hellmann potential model", *Rev. Mex. Fis.* **66**, 730 (2020). <https://doi.org/10.31349/RevMexFis.66.730>

- [5] E.P. Inyang, E.P. Inyang, J.E. Ntibi, E.E. Ibekwe, and E.S. William, "Approximate solutions of D-dimensional Klein-Gordon equation with Yukawa potential via Nikiforov-Uvarov method", *Ind. J. Phys.* **95**, 2793 (2021). <https://doi.org/10.1007/s12648-020-01933-x>
- [6] E. P. Inyang, E. S. William and J.A. Obu, "Eigensolutions of the N-dimensional Schrödinger equation interacting with Varshni-Hulthen potential model", *Rev. Mex. Fis.* **67** (2021), 193. <https://doi.org/10.31349/RevMexFis.67.193>
- [7] E.S. William, E.P. Inyang, I.O. Akpan, J.A. Obu, A.N. Nwachukwu, and E.P. Inyang, "Ro-vibrational energies and expectation values of selected diatomic molecules via Varshni plus modified Kratzer potential model", *Indian Journal of Physics*, **96**, 3461 (2022). <https://doi.org/10.1007/s12648-0222-02308-0>
- [8] E.P. Inyang, E.P. Inyang, E.S. William, and E.E. Ibekwe, "Study on the applicability of Varshni potential to predict the mass-spectra of the Quark-Antiquark systems in a non-relativistic framework", *Jord. J. Phys.* **14**, 345 (2021).
- [9] E.P. Inyang, A.N. Ikot, E.P. Inyang, I.O. Akpan, J.E. Ntibi, E. Omugbe, and E.S. William, "Analytic study of thermal properties and masses of heavy mesons with quarkonium potential", *Result in Physics*, **39**, 105754 (2022). <https://doi.org/10.1016/j.rinp.2022.105754>
- [10] E.P. Inyang, and E.O. Obisung, "The study of electronic states of NI and Scl molecules with screened Kratzer Potential", *East Eur. J. Phys.* **3**, 32 (2022). <https://doi.org/10.26565/2312-4334-2022-3-04>
- [11] C.O. Edet, S. Mahmoud, E.P. Inyang, N. Ali, S.A. Aljunid, R. Endut, A.N. Ikot, and M. Asjad, "Non-Relativistic Treatment of the 2D Electron System Interacting via Varshni-Shukla Potential Using the Asymptotic Iteration Method", *Mathematics*, **10**, 2824 (2022). <https://doi.org/10.3390/math10152824>
- [12] M. Abu-Shady, and A.N. Ikot, "Analytic solution of multi-dimensional Schrödinger equation in hot and dense QCD media using the SUSYQM method", *The European Physical Journal Plus*, **134**, 321 (2019). <https://doi.org/10.1140/epjp/i2019-12685-y>
- [13] A.N. Ikot, U.S. Okorie, P.O. Amadi, C.O. Edet, G.J. Rampho, and R. Sever, "The Nikiforov-Uvarov –Functional Analysis (NUFA) Method: A new approach for solving exponential – Type potentials", *Few-Body System*, **62**, 9 (2021). <https://doi.org/10.1007/s00601-021-021-01593-5>
- [14] E.P. Inyang, E.S. William, J.E. Ntibi, J.A. Obu, P.C. Iwuji, and E.P. Inyang, "Approximate solutions of the Schrödinger equation with Hulthén plus screened Kratzer Potential using the Nikiforov–Uvarov – functional analysis (NUFA) method: an application to diatomic molecules", *Can. J. Phys.* **100**(10), 473 (2022), <https://doi.org/10.1139/cjp-2022-003>
- [15] E.P. Inyang, P.C. Iwuji, J.E. Ntibi, E. Omugbe, E.A. Ibanga, and E.S. William, "Quark-antiquark study with inversely quadratic Yukawa potential using Nikiforov-Uvarov-Functional analysis method", *East Eur. J. Phys.* **2**, 51 (2022). <https://doi.org/10.26565/2312-4334-2022-2-05>
- [16] E.P. Inyang, E.S. William, E. Omugbe, E.P. Inyang, E.A. Ibanga, F. Ayedun, I.O. Akpan, and J.E. Ntibi, "Application of Eckart-Hellmann potential to study selected diatomic molecules using Nikiforov-Uvarov-Functional analysis method", *Revista Mexicana de Fisica*, **68**, 1 (2022). <https://doi.org/10.31349/RevMexFis.68.020401>
- [17] E.P. Inyang, E.P. Inyang, I.O. Akpan, J.E. Ntibi, and E.S. William, "Analytical solutions of the Schrödinger equation with class of Yukawa potential for a quarkonium system via series expansion method", *European Journal of Applied Physics*, **2**, 26 (2020). <http://dx.doi.org/10.24018/ejphysics.2020.2.6.26>
- [18] E.P. Inyang, P.C. Iwuji, J.E. Ntibi, E.S. William, and E.A. Ibanga, "Solutions of the Schrodinger equation with Hulthén–screened Kratzer potential: Application to diatomic molecules", *East Eur. J. Phys.* **1**, 11 (2022). <https://doi.org/10.26565/2312-4334-2022-2-02>
- [19] E.E. Ibekwe, U.S. Okorie, J.B. Emah, E.P. Inyang, and S.A. Ekong, "Mass spectrum of heavy quarkonium for screened Kratzer potential (SKP) using series expansion method", *European Physical Journal Plus*, **87**, 11 (2021). <https://doi.org/10.1140/epjp/s13360-021-01090-y>
- [20] E.P. Inyang, J. E.Ntibi, O.O. Akintola, E.A. Ibanga, F. Ayedun, and E.S. William, "Analytical solutions to the Schrödinger Equation with a Combined Potential using the Series Expansion Method to Study Selected Diatomic Molecules", *Communication in Physical Science*, **8**(2),244(2022).
- [21] E.P. Inyang, E.P. Inyang, J.E. Ntibi, and E.S. William, "Analytical solutions of Schrodinger equation with Kratzer-screened Coulomb potential for a Quarkonium system", *Bulletin of Pure and Applied Sciences*, **40**, 24 (2021). <https://doi.org/10.5958/2320-3218.2021.0002.6>
- [22] E. Omugbe, "Non-relativistic energy spectrum of the Deng-Fan Oscillator via the WKB Approximation method", *Asian Journal of Physical and Chemical Sciences*, **268**, 26 (2020). <https://doi.org/10.9734/ajopacs/2020/v8i130107>
- [23] E. Omugbe, O.E. Osafire, E.P. Inyang, and A. Jahanshir, "Bound state solutions of the hyper-radial Klein-Gordon equation under the Deng-Fan potential by WKB and SWKB methods", *Physica Scripta*, **96**(12), 125408 (2021). <https://doi.org/10.1088/1402-4896/ac38d4>
- [24] E. Omugbe, O.E. Osafire, I.B. Okon, E.P. Inyang, E.S. William, and A. Jahanshir, "Any L-state energy of the spinless Salpeter equation under the Cornell potential by the WKB Approximation method: An Application to mass spectra of mesons", *Few-Body Systems* **63**, 6 (2022). <https://doi.org/10.1007/s00601-021-01705-1>
- [25] S.H. Dong, and M. Cruz-Irisson, "Energy spectrum for a modified Rosen-Morse potential solved by proper quantization rule and its thermodynamic properties", *Journal of Mathematical Chemistry*, **50**, 881 (2012). <https://doi.org/10.1007/s10910-011-9931-3>
- [26] C.A. Onate, M.C. Onyeaju, E. Omugbe, I.B. Okon, and O.E. Osafire, "Bound-state solutions and thermal properties of the modified Tietz–Hua potential", *Sci. Rep.* **11**, 2129 (2021). <https://doi.org/10.1038/s41598-021-81428-9>
- [27] U.M. Ukewuihe, C.P. Onyenegecha, S.C. Udensi, C.O. Nwokocha, C.J. Okereke, I.J. Njoku, and A.C. Illoanya, "Approximate solutions of Schrodinger equation in D Dimensions with the modified Mobius square plus Hulthen potential", *Mathematics and computational science*, **3**, (2021). <https://doi.org/10.30511/mcs.2021.527027.1020>
- [28] R. Sahadevan, and P. Prakash, "Exact solution of certain time fractional nonlinear partial differential equations", *Nonlinear Dynamics*, **85**, 659 (2016). <https://doi.org/10.1007/s11071-016-2714-4>
- [29] R.L. Greene, and C. Aldrich, "Variational wave functions for a screened Coulomb potential", *Phys. Rev. A*, **14**, 2363 (1976). <https://doi.org/10.1103/PhysRevA.14.2363>
- [30] C.L. Pekeris, "The Rotation-Vibration Coupling in Diatomic Molecules", *Phys. Rev.* **45**, 98 (1934). <https://doi.org/10.1103/PhysRev.45.98>

- [31] C.S. Jia, T. Chen, and L.G. Cui, “Approximate analytical solutions of the Dirac equation with the generalized Poschl-Teller potential including the pseudo-centrifugal term”, *Phys. Lett. A*, **373**, 1621 (2009). <https://doi.org/10.1016/j.physleta.2009.03.006>
- [32] E.P. Inyang, E.O. Obisung, P.C. Iwuji, J.E. Ntibi, J. Amajama, and E.S. William, “Masses and thermal properties of a charmonium and Bottomonium mesons”, *J. Nig. Soc. Phys. Sci.* **4**, 884 (2022). <https://doi.org/10.46481/jnsps.2022.884>
- [33] E.P. Inyang, E.P. Inyang, I.O. Akpan, J.E. Ntibi, and E.S. William, “Masses and thermodynamic properties of a Quarkonium system”, *Canadian J. Phys.* **99**(11), (2021). <https://doi.org/10.1139/cjp-2020-0578>
- [34] E. Omugbe, O.E. Osafire, I.B. Okon, E.S. Eyube, E.P. Inyang, U.S. Okorie, A. Jahanshir, and C.A. Onate, “Non-relativistic bound state solutions with l -deformed Kratzer-type potential using the super-symmetric WKB method: application to theoretic-information measures”, *European Physical Journal D*, **76**, 72 (2022). <https://doi.org/10.1140/epjd/s10053-022-00395-6>
- [35] A. Nagy, and S. Liu, “Local wave-vector, Shannon and Fisher information”, *Phys. Lett. A*, **372**, 1654 (2008). <https://doi.org/10.1016/j.physleta.2007.10.055>
- [36] C.E. Shannon, “A Mathematical Theory of Communication”, *Bell System Technical Journal*, *Bell Syst. Tech. J.* **27**, 623 (1948). <https://doi.org/10.1002/j.1538-7305.1948.tb01338.x>
- [37] S. Kullberg, and R.A. Leibler, “On Information and Sufficiency”, *Ann. Math. Stat.* **22**, 79 (1951). <https://www.jstor.org/stable/2236703>
- [38] S. Kullberg, *Information Theory and Statistics*, (Wiley, New York, 1959).
- [39] R.A. Fisher, “Theory of Statistical Estimation”, *Mathematical Proceedings of the Cambridge Philosophical Society*, **22**(5), 700 (1925). <https://doi.org/10.1017/s0305004100009580>
- [40] S.B. Sears, R.G. Parr, and U. Dinur, “On the Quantum-Mechanical Kinetic Energy as a Measure of the Information in a Distribution”, *Israel J. Chem.* **19**, 165 (1980). <https://doi.org/10.1002/ijch.198000018>
- [41] S. Majumdar, N. Mukherjee, and A.K. Roy, “Information entropy and complexity measure in generalized Kratzer potential”, *Chem. Phys. Lett.* **716**, 257 (2019). <https://doi.org/10.1016/j.cplett.2018.12.032>
- [42] G.H. Sun, and S.H. Dong, “Quantum information entropies of the eigenstates for a symmetrically trigonometric Rosen–Morse potential”, *Phys. Scr.* **87**, 045003 (2013). <https://doi.org/10.1088/0031-8949/87/04/045003>
- [43] I. Bialynicki-Birula, and J. Mycielski, “Uncertainty relations for information entropy in wave mechanics”, *Commun. Math. Phys.* **44**, 129 (1975). <https://doi.org/10.1007/BF01608825>
- [44] R. Santana-Carrilloria, J.S. Gonzalez-Flores, E. Magana-Espinal, L.F. Quezada, G.-H. Sun, and S.-H. Dong, “Quantum Information Entropy of Hyperbolic potentials in Fractional Schrodinger equation”, *Entropy*, **24**, 1516 (2022). <https://doi.org/10.3390/e24111516>
- [45] A. Boumali, and M. Labidi, “The Solutions on One-Dimensional Dirac Oscillator with Energy-Dependent Potentials and Their Effects on the Shannon and Fisher Quantities of Quantum Information Theory”, *J. Low Temp. Phys.* **204**, 24 (2021). <https://doi.org/10.1007/s10909-021-02596-6>
- [46] C. Martinez-Flores, “Shannon entropy and Fisher information for endohedral confined one- and two-electron atoms”, *Physics Letters A*, **386**, 126988 (2021). <https://doi.org/10.1016/j.physleta.2020.126988>
- [47] C.O. Edet, E.B. Ettah, S.A. Aljunid, R. Endut, N. Ali, A.N. Ikot, and M. Asjad, “Global Quantum information-Theoretic measures in the Presence of magnetic and Aharonov-Bohm (AB) fields”, *Symmetry*, **14**(5), 976 (2022). <https://doi.org/10.3390/sym14050976>
- [48] O. Olendki, “Quantum information measures of the Aharonov-Bohm ring in uniform magnetic fields”, *Phys. Lett. A*, **383**, 1110 (2019). <https://doi.org/10.1016/j.physleta.2018.12.040>
- [49] C.A. Onate, M.C. Onyeaju, and I.B. Okon, “Shannon entropy for Feiberg-Horodecki equation and thermal properties of improved Wei potential model”, *Open Physics*, **19**, 519 (2021). <https://doi.org/10.1515/phys-2021-0038>
- [50] C.A. Onate, M.C. Onyeaju, D.T. Bankole, and A.N. Ikot, “Eigensolution techniques, expectation values and Fisher information of Wei potential function”, *J. Mol. Modeling*, **26**, 311 (2020). <https://doi.org/10.1007/s00894-020-04573-4>
- [51] C.A. Onate, M.C. Onyeaju, A.N. Ikot, O. Ebomwonyi, and J.O.A. Idiodi, “Fisher information and uncertainty relations for potential family”, *Int. J. Quantum Chem.* **119**(19), e25991 (2019). <https://doi.org/10.1002/qua.25991>
- [52] C.A. Onate, M.C. Onyeaju, E.E. Ituen, A.N. Ikot, O. Ebomwonyi, J.O. Okoro, and K.O. Dopamu, “Eigensolutions, Shannon entropy and information energy for modified Tietz-Hua potential”, *Indian J. Phys.* **92**, 487 (2018). <https://doi.org/10.1007/s12648-017-1124-x>
- [53] J.O.A. Idiodi, and C.A. Onate, “Entropy, Fisher information and Variance with Frost-Musulin Potential”, *Commun. Theor. Phys.* **66**, 269 (2016). <https://doi.org/10.1088/0253-6102/66/3/269>
- [54] C.A. Onate, O. Adebimpe, B.O. Adebisin, and A.F. Lukman, “Information-theoretic measure of the hyperbolic exponential-type potential”, *Turk. J. Phys.* **42**(4), 402 (2018). <https://doi.org/10.3906/fiz-1802-40>
- [55] C.O. Edet, F.C.E. Lima, C.A.S. Almeida, N. Ali, and M. Asjad, “Quantum information of the Aharonov-Bohm ring with Yukawa interaction in the Presence of Disclination”, *Entropy*, **24**, 1059 (2022). <https://doi.org/10.3390/e24081059>
- [56] A.N. Ikot, G.J. Rampho, P.O. Amadi, M.J. Sithole, U.S. Okorie, and M.L. Lekala, “Shannon entropy and Fisher information-theoretic measures for Mobius square potential”, *Eur. Phys. J. Plus*, **135**, 503 (2020). <https://doi.org/10.1140/epjp/s13360-020-00525-2>
- [57] P.O. Amadi, A.N. Ikot, A.T. Ngiangia, U.S. Okorie, G.J. Rampho, and H.Y. Abdullah, “Shannon entropy and Fisher information for screened Kratzer potential”, *Intl. J. Quantum Chem.* **120**(14), e26246 (2020). <https://doi.org/10.1002/qua.26246>
- [58] A.N. Ikot, G.J. Rampho, P.O. Amadi, U.S. Okorie, M.J. Sithole, and M.L. Lekala, “Quantum information-entropic measures for exponential – type potential”, *Results in Physics* **18**, 103150 (2020). <https://doi.org/10.1016/j.rinp.2020.103150>
- [59] A.N. Ikot, G.J. Rampho, P.O. Amadi, U.S. Okorie, M.J. Sithole, and M.L. Lekala, “Theoretic quantum information entropies for the generalized hyperbolic potential”, *Intl. J. Quantum Chem.* **120**(24), e26410 (2020). <https://doi.org/10.1002/qua.26410>
- [60] C. Eckart, “The penetration of a potential barrier by electrons”, *Phys. Rev.* **35**, 1303 (1930). <https://doi.org/10.1103/PhysRev.35.1303>
- [61] B.J. Falaye, “Any l-state solutions of the Eckart potential via asymptotic iteration method”, *Central Euro. J. Phys.* **10**, 960 (2012). <https://doi.org/10.2478/s11534-012-0047-6>
- [62] E.P. Inyang, J.E. Ntibi, E.P. Inyang, E.S. William, and C.C. Ekechukwu, “Any L-state solutions of the Schrödinger equation interacting with class of Yukawa-Eckart potentials”, *Int. J. Innov. Res. Sci. Eng. Tech.* **11**(7), (2020).

- [63] S.H. Dong, W.C. Qiang, G.H. Sun, and V.B. Bezerra, *J. Phys. A: Mathematical and Theoretical*, **40**, 10535 (2007). <https://doi.org/10.1088/1751-8113/40/34/010>
- [64] H. Hellmann, "A New Approximation Method in the Problem of Many Electrons", *J. Chem. Phys.* **3**, 61 (1935). <https://doi.org/10.1063/1.1749559>
- [65] C.A. Onate, J.O. Ojonubah, A. Adeoti, E.J. Eweh, and M. Ugboja, "Approximate Eigen Solutions of D.K.P. and Klein-Gordon Equations with Hellmann Potential", *Afr. Rev. Phys.* **9**, 497 (2014). <https://core.ac.uk/download/pdf/162156005.pdf>
- [66] S.M. Ikhdaïr, and R. Sever, "A perturbative treatment for the bound states of the Hellmann potential", *Journal of Molecular Structure, THEOCHEM*, **809**(1-3), 103 (2007). <https://doi.org/10.1016/j.theochem.2007.01.019>
- [67] Hamzavi, K.E. Thylwe, and A.A. Rajabi, "Approximate Bound States Solution of the Hellmann Potential", *Commun Theor Phys*, **60**, 8 (2013). <https://doi.org/10.1088/0253-6102/60/1/01>
- [68] C.A. Onate, O. Ebomwonyi, K.O. Dopamu, J.O. Okoro, and M.O. Oluwayemi, "Eigen solutions of the D-dimensional Schrodinger equation with inverse trigonometry scarf potential and Coulomb potential", *Chin. J. Phys.* **56**(5), 2538 (2018). <https://doi.org/10.1016/j.cjph.2018.03.013>
- [69] B.I. Ita, "Solutions of the Schrodinger equation with inversely quadratic Hellmann plus Mie-type potential using Nikiforov-Uvarov method", *International Journal of Recent Advances in Physics.* **2**(4), 25 (2013). <https://wireilla.com/physics/ijrap/papers/2413ijrap02.pdf>
- [70] E.P. Inyang, E.S. William, J.O. Obu, B.I. Ita, E.P. Inyang, and I.O. Akpan, "Energy spectra and expectation values of selected diatomic molecules through the solutions of Klein-Gordon equation with Eckart-Hellmann potential model", *Molecular Physics.* **119**(23), e1956615 (2021). <https://doi.org/10.1080/00268976.2021.1956615>
- [71] E.P. Inyang, E.O. Obisung, E.S. William, and I.B. Okon, "Non-Relativistic study of mass spectra and thermal properties of a quarkonium system with Eckart-Hellmann potential", *East Eur. J. Phys.* **3**, 114 (2022)114. <https://doi.org/10.26565/2312-4334-2022-3-14>
- [72] E.S. William, E.P. Inyang, J.E. Ntibi, J.A. Obu, and E.P. Inyang, "Solutions of the Non-relativistic Equation Interacting with the Varshni-Hellmann potential model with some selected Diatomic molecules", *Jordan Journal of Physics*, **15**, 193 (2022). <https://doi.org/10.47011/15.2.8>
- [73] E.P. Inyang, F. Ayedun, E.A. Ibang, K.M. Lawal, I.B. Okon, E.S. William, O. Ekwevugbe, C.A. Onate, A.D. Antia, and E.O. Obisung, "Analytical Solutions of the N-Dimensional Schrödinger equation with modified screened Kratzer plus Inversely Quadratic Yukawa potential and Thermodynamic Properties of selected Diatomic Molecules", *Results in Physics*, **43**, 106075 (2022). <https://doi.org/10.1016/j.rinp.2022.106075>
- [74] O. Ebomwonyi, C.A. Onate, M.C. Onyeaju, and A.N. Ikot, "Any l-states solutions of the Schrodinger equation interacting with Hellmann-generalized Morse potential model", *Karbala Intl. J. Mod. Sc.* **3**, 59 (2017). <http://eprints.lmu.edu.ng/1613/2/ONATE%2038.pdf>
- [75] C.O. Edet, and A.N. Ikot, "Shannon information entropy in the Presence of magnetic and Aharonov-Bohm (AB) fields", *Eur. Phys. J. Plus*, **136**, 432 (2021). <https://doi.org/10.1140/epjp/s13360-021-01438-4>
- [76] W.A. Yahya, K.J. Oyewuni, and K.D. Sen, "Position and momentum information-theoretic measures of the pseudoharmonic potential", *Int. J. Quantum Chem.* **115**, 1543 (2014). <https://doi.org/10.1002/qua.24971>
- [77] S.H. Patil, K.D. Sen, N.A. Watson, and H.E. Montgomery Jr, "Characteristic features of net information measures for constrained Coulomb potentials", *J. Phys. B: At. Mol. Opt. Phys.* **40**, 2147 (2007). <https://doi.org/10.1088/0953-4075/40/11/016>
- [78] Y.J. Shi, G.H. Sun, J. Jing, and S.H. Dong, "Shannon and Fisher entropy measures for a parity-restricted harmonic oscillator", *Laser Phys.* **27**, 125207 (2017).
- [79] D. Chakraborty, P.W. Ayers, in: *Statistical Complexity: Applications in Electronic Structure*, edited by K.D. Sen, (Springer, 2012).
- [80] E. Romera, P. Sanchez-Moreno, J.S. Dehesa, "The Fisher information of single-particle systems with a central potential", *Chem. Phys. Lett.* **414**, 468 (2005). <https://doi.org/10.1016/j.cplett.2005.08.032>



**АНАЛІТИЧНІ РІШЕННЯ РІВНЯННЯ ШРЕДІНГЕРА З МОДЕЛЯМИ КОЛЕКТИВНОГО ПОТЕНЦІАЛУ:
ЗАСТОСУВАННЯ ДО КВАНТОВОЇ ТЕОРІЇ ІНФОРМАЦІЇ**

Фунмілайо Аїедун, Етідо П. Іньянг, Ефіонг А. Ібанга, Колаволе М. Лавал
Факультет фізики, Національний відкритий університет Нігерії, Джабі, Абуджа

У цьому дослідженні шляхом аналітичного розв'язання рівняння Шредінгера з використанням потенціалу Екарта-Гельмана та методу Нікіфорова-Уварова були отримані рівняння енергії та нормалізована хвильова функція. Досліджено інформацію Фішера та ентропію Шеннона. Наші результати показали характерну поведінку вищого порядку для положення у просторі та імпульсу. Наші чисельні результати показали підвищення точності визначення місця розташування передбачуваних частинок, що зустрічаються у положенні в просторі. Крім того, наші результати показують, що сума ентропій позиції та імпульсу задовольняє нижню межу нерівності Беркнера, Бялиницького-Бірулі та Міческі, а інформація Фішера також задовольняється для різних власних станів. Висновки цього дослідження знайдуть застосування в квантовій хімії, атомній і молекулярній фізиці та квантовій фізиці.

Ключові слова: рівняння Шредінгера; потенціал Екарта-Гельмана; Інформація Фішера; ентропія Шеннона; Метод Нікіфорова-Уварова

A STUDY OF PHOTONEUTRON REACTIONS USING STATISTICAL ANALYSIS[†]

 Deniz Canbula^{a*},  Bora Canbula^b

^aDepartment of Alternative Energy Resources Technology, Manisa Celal Bayar University, Manisa, Turkey

^bDepartment of Computer Engineering, Manisa Celal Bayar University, Manisa, Turkey

*Correspondence Author: deniz.canbula@cbu.edu.tr

Received October 12, 2022; revised October 28, 2022; accepted November 9, 2022

The well-known inputs for determining the reaction cross section are nuclear level density (NLD) and γ -ray strength functions. In this work, effects of γ -ray strength functions and NLD models on photoneutron reactions of ^{76,77,78}Se isotopes are analyzed by using the latest version of TALYS computer code. For γ -ray strength functions, macroscopic and microscopic options which are available in the TALYS, are used in the calculations. Kopecky-Uhl and Brink Axel γ -ray strength function models as macroscopic options, Hartree-Fock BCS tables, Hartree-Fock Bogolyubov tables and Goriely's hybrid model as microscopic options are preferred. The statistical analysis is carried out to determine the γ -ray strength function that reproduces the experimental data quite well. And then, calculations of photoneutron cross section are redone by using the determined γ -ray strength function via the NLD models. The Constant Temperature Model (CTM), Back Shifted Fermi Gas Model (BSFGM) and Generalized Superfluid Model (GSM) are preferred to use in NLD calculations. The predictions are compared with each other and the available experimental data. EXFOR library is used to take all experimental data.

Keywords: Nuclear level density models; Cross section; γ -ray strength functions; Photoneutron reactions; TALYS

PACS: 21.10.Ma, 25.20.-x

The proton induced reactions are commonly used in variety of applications from astrophysics to transmutation of nuclear waste and can give beneficial knowledge about the data estimation of nuclear reactions. The most important channel of these reactions is gamma emission channel, which is defined by gamma ray strength functions. This channel can be observable in all other reactions and can called as universal channel. Therefore, it has a great importance to describe this channel. The well-known and useful inputs for theoretical calculations of the photon induced reactions are NLD and γ -ray strength functions. These functions can be selected as an optional input in the computer codes [1,2]. There are many theoretical [3-6] and experimental [7-10] works for photon induced reactions in the literature using these codes.

In the photon induced reactions, giant dipole resonance (GDR) is dominant at energies below 30 MeV. It is observable in the energy range 10–15 MeV, and 20–25 MeV for heavy and light nuclei, respectively. In GDR energies, maximum photoabsorption and cross section of other photonuclear reactions are observed. The aim of the work is to study the effect of the nuclear level density and γ -ray strength function on cross section of photoneutron reactions. To analyze these effects, best known computer code TALYS is used for the theoretical calculations [11-19]. This code is widely used code in the reaction analysis. The effect of γ -ray strength function is investigated by using Kopecky-Uhl generalized Lorentzian, Brink-Axel Lorentzian, Hartree-Fock BCS table, Hartree-Fock Bogolyubov tables and Goriely's hybrid models. The γ -ray strength function which give the closest result to the experimental data, is determined with the statistical calculations. Then, best strength function is used together with nuclear level density models and calculations are reperformed using TALYS code for each reaction. To analyze the effect of nuclear level density models, Constant Temperature Model (CTM), Back-Shifted Fermi Gas Model (BSFGM, and Generalized Superfluid Model (GSM) are used. The predictions are presented and discussed with the experimental data taken from EXFOR [20] library. The best combinations of models are decided by evaluating the statistical analysis.

The rest of this paper is organized as follows: In section "Materials and Methods", calculation method is presented. In section "Results and Discussion", I represent my results and their discussions. Finally, in section "Conclusion", I give some concluding remarks.

MATERIALS AND METHODS

For the gamma induced nuclear reactions, γ -ray strength functions are the key input. This function is used to calculate the reaction cross section with the statistical theory and defines the transmission coefficients.

The phenomenological model, Brink Axel is used to determine the γ -ray strength functions for $E1$, $E2$ and $M1$ modes [21,22]. According to this model, gamma ray strength function is given as a standard Lorentzian form below as

$$f_{\chi l}(E_{\gamma}) = \frac{1}{(2l+1)\pi^2 \hbar^2 c^2} \frac{\sigma_{\chi l} E_{\gamma} \Gamma_{\chi l}^2}{(E_{\gamma}^2 - E_{\chi l}^2)^2 + E_{\gamma}^2 \Gamma_{\chi l}^2}, \quad (1)$$

where $\sigma_{\chi l}$ is the strength, $E_{\chi l}$ is the energy, and $\Gamma_{\chi l}$ is the width of resonance. They are the giant dipole parameters.

[†] Cite as: D. Canbula, and B. Canbula, East Eur. J. Phys. 4, 99 (2022), <https://doi.org/10.26565/2312-4334-2022-4-08>
© D. Canbula, B. Canbula, 2022

For $E1$ radiation, this standard Lorentzian form is generalized and written as

$$f_{E1}(E_\gamma, T) = \frac{\sigma_{E1}\Gamma_{E1}}{(2l+1)\pi^2\hbar^2c^2} \left[\frac{E_\gamma\tilde{\Gamma}_{E1}(E_\gamma)}{(E_\gamma^2-E_{E1}^2)+E_\gamma^2\tilde{\Gamma}_{E1}(E_\gamma)^2} + \frac{0.7\Gamma_{E1}4\pi^2T^2}{E_{E1}^3} \right], \quad (2)$$

where $\tilde{\Gamma}_{E1}(E_\gamma)$ is temperature and energy dependent width [23] and given as

$$\tilde{\Gamma}_{E1}(E_\gamma) = \Gamma_{E1} \frac{E_\gamma^2+4\pi^2T^2}{E_{E1}^2}, \quad (3)$$

where T is a nuclear temperature and written below

$$T = \sqrt{\frac{E_n+S_n-\delta-E_\gamma}{a(S_n)}}, \quad (4)$$

where δ is the pairing correction, E_n is the neutron energy, S_n is the neutron separation energy, and a is the nuclear level density parameter.

Bardeen Cooper Schrieffer (BCS) [24] model is a microscopic option for $E1$ radiation. It can be found a detail information for this model and the other microscopic gamma ray strength function models (Hartree-Fock Bogolyubov and Goriely's hybrid) from Reference input Parameter library (RIPL-3) database [25].

Nuclear level density is the number of excited levels around an excitation energy. The first model of nuclear level density has been proposed by Bethe [26] called as Fermi gas model. According to this model, nucleons do not interact with each other, have equispaced single particle states, and collective levels are absent. The total nuclear level density formulation is given as

$$\rho^{tot}(U) = \frac{1}{12\sqrt{2}\sigma} \frac{\exp[2\sqrt{aU}]}{a^{1/4}U^{5/4}}, \quad (5)$$

where a is the main variable of the nuclear level density and called nuclear level density parameter, U is the excitation energy, and σ is the spin-cutoff parameter.

The default option of TALYS computer code is Constant Temperature Model (CTM) [27]. This model considers the energy region in two parts as low and high. For Back-Shifted Fermi Gas Model (BSFGM) [28] Fermi gas expression is used for all energy range. The other nuclear level density model, Generalized Superfluid Model (GSM) [29] based on BCS theory has a pairing correlation, and is characterized by a phase transition.

γ -ray strength functions and nuclear level density models are inputs to calculate the reaction cross sections. Therefore, if these two inputs are used together in the calculations, successful results can be obtained.

TALYS computer code is used for all calculations. It is a computer program which simulates nuclear reactions, which are caused by light particles such as gamma, proton, neutron, triton etc. from 1 keV to 1 GeV. γ -ray strength functions and nuclear level density models can be used as an optional input in TALYS.

RESULTS AND DISCUSSION

In this work, cross sections of $^{76}\text{Se}(g,n)^{75}\text{Se}$, $^{77}\text{Se}(g,n)^{76}\text{Se}$, and $^{78}\text{Se}(g,n)^{77}\text{Se}$ reactions are calculated with different γ -ray strength functions and nuclear level density models by using TALYS computer code. The predictions are shown in Figs. 1-6, and statistical results are presented in Tables 1 and 2.

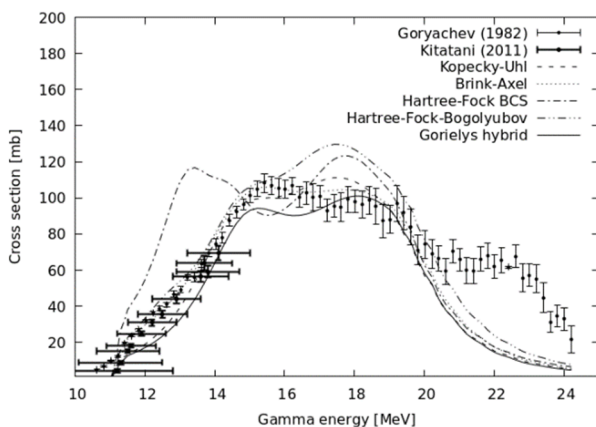


Figure 1. Comparison of gamma ray strength function calculations with the experimental data for $^{76}\text{Se}(g,n)^{75}\text{Se}$

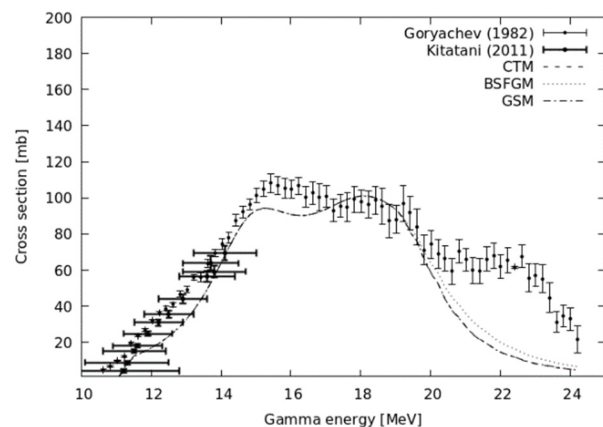


Figure 2. Comparison of nuclear level density calculations with the experimental data for $^{76}\text{Se}(g,n)^{75}\text{Se}$

$^{76}\text{Se}(g,n)^{75}\text{Se}$ reaction cross section calculations with γ -ray strength functions are given in Fig. 1. The results of Hartree-Fock BCS tables show two humps at the giant dipole resonance region. Hartree-Fock BCS and Hartree-Fock

Bogolyubov display the predictions far from the experimental data. According to the statistical analysis given in Table 1, Goriely's hybrid model are chosen the best γ -ray strength function, which reproduces the experimental data.

Table 1. Statistical analysis of (g,n) reaction cross section calculations using gamma ray strength functions.

Target	Kopecky-Uhl	Brink Axel	Hartree-Fock BCS	Hartree-Fock Bog.	Goriely's hybrid
^{76}Se	0.7179	0.7858	0.4743	0.8006	0.8127
^{77}Se	0.2166	0.7157	0.7780	0.8126	0.6675
^{78}Se	0.5019	0.4028	0.2210	0.6114	0.5925

The calculations for $^{76}\text{Se}(g,n)^{75}\text{Se}$ reaction are redone by using Goriely's hybrid model with nuclear level density models. The calculation results with nuclear level density models are given in Fig. 2. All models have close predictions. However, statistical analysis for nuclear level density models given in Table 2 is presented that for this reaction, best combination is Goriely's hybrid model and BSFGM.

Table 2. Statistical analysis of (g,n) reaction cross section calculations using nuclear level density models

Target	CTM	BSFGM	GSM
^{76}Se	0.8127	0.8467	0.8142
^{77}Se	0.8126	0.8433	0.8750
^{78}Se	0.6114	0.6526	0.5826

In Fig. 3, comparisons of $^{77}\text{Se}(g,n)^{76}\text{Se}$ reaction cross section calculations with γ -ray strength functions are shown. All predictions have higher peaks at 15 MeV-20 MeV energies. According to the statistical analysis table for γ -ray strength functions, Kopecky Uhl generalized Lorentzian form is the worst model, and Hartree-Fock Bogolyubov model has the best result compared the others. The cross sections are recalculated using Hartree-Fock Bogolyubov model with nuclear level density models. Predictions are compared with the experimental data and shown in Fig. 4. According to the statistical analysis for nuclear level density models, GSM has the best prediction to reproduce the experimental data.

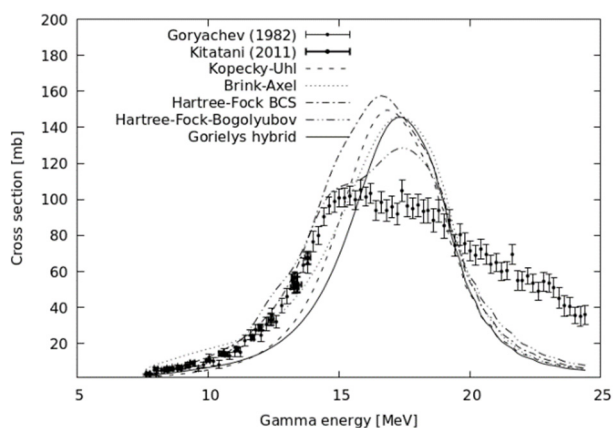


Figure 3. Comparison of gamma ray strength function calculations with the experimental data for $^{77}\text{Se}(g,n)^{76}\text{Se}$

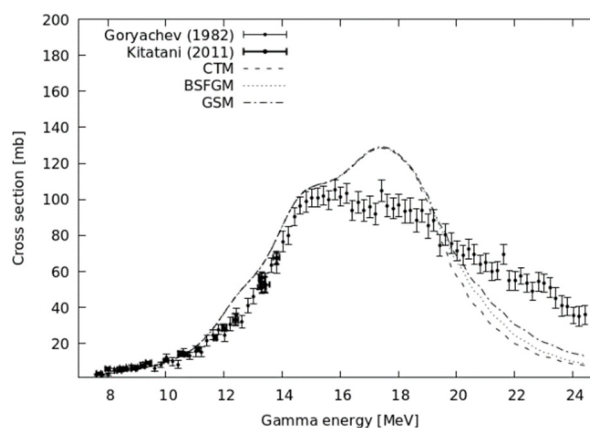


Figure 4. Comparison of nuclear level density calculations with the experimental data for $^{77}\text{Se}(g,n)^{76}\text{Se}$

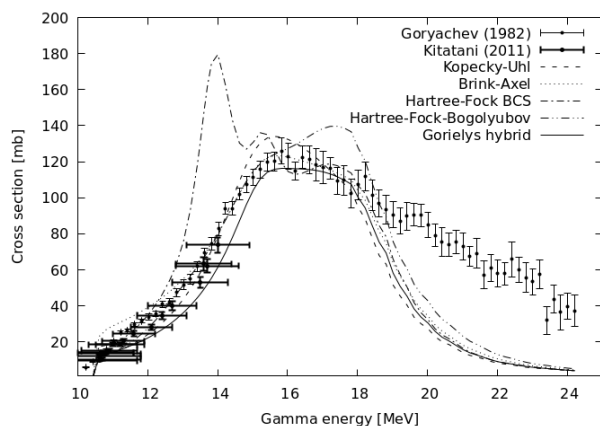


Figure 5. Comparison of gamma ray strength function calculations with the experimental data for $^{78}\text{Se}(g,n)^{77}\text{Se}$

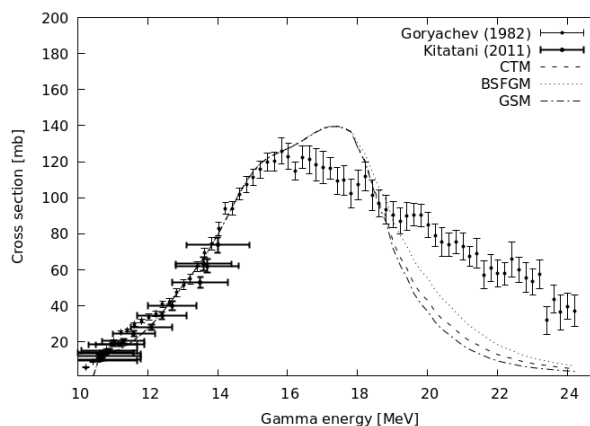


Figure 6. Comparison of nuclear level density model calculations with the experimental data for $^{78}\text{Se}(g,n)^{77}\text{Se}$

For $^{78}\text{Se}(g,n)^{77}\text{Se}$ reaction, calculations are performed with γ -ray strength functions and compared with the experimental data in Fig. 5. All models have similar geometries after 18 MeV gamma energy. Hartree-Fock BCS and Hartree-Fock Bogolyubov models are far away from the experimental data at between 13 MeV-18 MeV energies. According to the statistical analysis table, Hartree-Fock Bogolyubov is the closest model to the experimental data. After γ -ray strength function model is determined, calculations are redone for nuclear level density models and represented in Fig. 6. According to Table 2, BSFGM can be chosen as a suitable nuclear level density model for this reaction.

CONCLUSION

The photoneutron cross sections of $^{76,77,78}\text{Se}$ isotopes are analyzed using available γ -ray strength functions and nuclear level density models in TALYS computer code. The following concluding remarks can be written as:

- The results of nuclear level density model calculations performed with γ -ray strength function models agree with the experimental data for all reactions in this study.
- For all investigated reactions, microscopic γ -ray strength functions are more successful to reproduce the experimental data than the others.
- Hartree-Fock BCS is the worst model to explain the experimental data for all calculations.
- All nuclear level density models have close predictions with each other.

ORCID IDs

Deniz Canbula, <https://orcid.org/0000-0003-0283-2698>; Bora Canbula, <https://orcid.org/0000-0003-1088-2804>

Conflict of interest statement. The authors declare that they have no conflict interest.

REFERENCES

- [1] A. Koning, S. Hilaire, and S. Goriely, *TALYS A Nuclear Reaction Program, User Manual*, The Netherlands (2022).
- [2] M. Herman, et al., *EMPIRE, Rivoli Modular System for Nuclear Reaction Calculations and Nuclear Data Evaluation, User's Manual*, National Nuclear Data Center (2012).
- [3] D. Canbula, *International Journal of Pure and Applied Sciences*, **7**, 314 (2021). <https://doi.org/10.29132/ijpas.879068>
- [4] B. Canbula, Süleyman Demirel Üniversitesi Fen Bilimleri Enstitüsü Dergisi **24**, 138 (2020). <https://doi.org/10.19113/sdufenbed.639828>
- [5] İ.H. Sarpün, H. Özdoğan, K. Taşdöven, H.A. Yalim, and A. Kaplan, *Modern Physics Letters A*, **34**, 1950210 (2019).
- [6] P.V. Cuong, T.D. Thiep, L.T. Anh, T.T. An, B.M. Hue, K.T. Thanh, N.H. Tan, et al, *Instruments and Methods in Physics Research Section B: Beam Interactions with Materials and Atoms*, **479**, 68 (2020). <https://doi.org/10.1016/j.nimb.2020.06.011>
- [7] J. Arends, J. Eyink, A. Hegerath, K. G. Hilger, B. Mecking, G. Nöldeke, and H. Rost, *Physics Letters B*, **98**, 423 (1981). [https://doi.org/10.1016/0370-2693\(81\)90444-5](https://doi.org/10.1016/0370-2693(81)90444-5)
- [8] E. Vagena, and S. Stoulos, *Nuclear Physics A*, **957**, 259 (2017). <https://doi.org/10.1016/j.nuclphysa.2016.09.007>
- [9] F. Kitatani, H. Harada, S. Goko, H. Utsunomiya, H. Akimune, H. Toyokawa, and K. Yamada, *Journal of nuclear science and technology*, **48**, 1017 (2011). <https://doi.org/10.1080/18811248.2011.9711787>
- [10] A.M. Goryachev, *Issues of theoretical and nuclear physics*, **8**, 121 (1982). (in Russian)
- [11] D. Canbula, and B. Canbula, *Nuclear Physics and Atomic Energy*, **23**, 5 (2022). <https://doi.org/10.15407/jnpac2022.01.005>
- [12] D. Canbula, *International Journal of Pure and Applied Sciences*, **8**, 173 (2022). <https://doi.org/10.29132/ijpas.1081660>
- [13] D. Canbula, Afyon Kocatepe Üniversitesi Fen Ve Mühendislik Bilimleri Dergisi, **22**, 730 (2022). <https://doi.org/10.35414/akufemubid.1097069>
- [14] D. Canbula, *Nuclear Instruments and Methods in Physics Research Section B: Beam Interactions with Materials and Atoms*, **478**, 229 (2020). <https://doi.org/10.1016/j.nimb.2020.06.041>
- [15] B. Canbula, D. Canbula, and H. Babacan, *Physical Review C*, **91**, 044615 (2015). <https://doi.org/10.1103/PhysRevC.91.044615>
- [16] Y. Kucuk, M. B. Yücel, I. Boztosun, T.K. Zholdybayev, B. Canbula, Z. Mukan, and K.M. Ismailov, *European Physical Journal A, Hadrons, and nuclei*, **58**, 97 (2022). <https://doi.org/10.1140/epja/s10050-022-00740-8>
- [17] K. Azhdarli, Y. Kucuk, B. Canbula, T. Zholdybayev, Z. Mukan, B. Emre, B.I. Boztosun, et al, in: *Tenth AASPP Workshop on Asian Nuclear Reaction Database Development*, (IAEA, Almaty, Kazakhstan, 2019), pp. 53.
- [18] B. Canbula, *Nuclear Instruments and Methods in Physics Research Section B: Beam Interactions with Materials and Atoms*, **391**, 73 (2017). <https://doi.org/10.1016/j.nimb.2016.11.006>
- [19] B. Canbula, *Celal Bayar University Journal of Science*, **13**, 445 (2017). <https://doi.org/10.18466/cbayarfbe.319917>
- [20] EXFOR, Brookhaven National Laboratory, National Nuclear Data Center, Database, <https://www-nds.iaea.org/exfor/>
- [21] D.M. Brink, *Nuclear Physics*, **4**, 215 (1957). [https://doi.org/10.1016/0029-5582\(87\)90021-6](https://doi.org/10.1016/0029-5582(87)90021-6)
- [22] P. Axel, *Physical Review* **126**, 671 (1962). <https://doi.org/10.1103/PhysRev.126.671>
- [23] J. Kopecky, and M. Uhl, *Physical Review C*, **41**, 1941 (1990). <https://doi.org/10.1103/PhysRevC.41.1941>
- [24] S. Goriely, S. Hilaire, A.J. Koning, M. Sin, and R. Capote, *Physical Review C*, **79**, 024612 (2009). <https://doi.org/10.1103/PhysRevC.79.024612>
- [25] R. Capote, M. Herman, P. Obložinský, P.G. Young, S. Goriely, T. Belgya, A.V. Ignatyuk, et al, *Nuclear Data Sheets*, **110**, 3107 (2009). <https://doi.org/10.1016/j.nds.2009.10.004>
- [26] H.A. Bethe, *Reviews of Modern Physics*, **9**, 69 (1937). <https://doi.org/10.1103/RevModPhys.9.69>
- [27] A. Gilbert, and A.G.W. Cameron, *Canadian Journal of Physics*, **43**, 1446 (1965). <https://doi.org/10.1139/p65-139>
- [28] W. Dilg, W. Schantl, H. Vonach, and M. Uhl, *Nuclear Physics A*, **217**, 269 (1973). [https://doi.org/10.1016/0375-9474\(73\)90196-6](https://doi.org/10.1016/0375-9474(73)90196-6)
- [29] A.V. Ignatyuk, K.K. Istekov, and G.N. Smirenkin, (Kernforschungszentrum Karlsruhe GmbH, Germany, 1979). <https://inis.iaea.org/search/searchsinglerecord.aspx?recordsFor=SingleRecord&RN=11512726>

ДОСЛІДЖЕННЯ ФОТОНЕЙТРОННИХ РЕАКЦІЙ ЗА ДОПОМОГОЮ СТАТИСТИЧНОГО АНАЛІЗУ**Деніз Канбула^а, Бора Канбула^б***^аФакультет технології альтернативних джерел енергії, Університет Маніси Челал Баяр, Маніса, Туреччина**^бФакультет комп'ютерної інженерії, Університет Маніси Челал Баяр, Маніса, Туреччина*

Добре відомими вхідними даними для визначення перетину реакції є щільність ядерного рівня (NLD) і силові функції γ -променів. У цій роботі за допомогою останньої версії комп'ютерного коду TALYS проаналізовано вплив силових функцій γ -випромінювання та моделей NLD на фотонейтронні реакції ізотопів $^{76,77,78}\text{Se}$. Для силових функцій γ -променів у розрахунках використовуються макроскопічні та мікроскопічні параметри, доступні в TALYS. Моделі функції сили Копекі-Ула та Брінка Аксея як макроскопічні варіанти, таблиці Хартрі-Фока VCS, таблиці Хартрі-Фока Боголюбова та гібридна модель Горілі як мікроскопічні варіанти. Проведено статистичний аналіз для визначення силових функцій γ -променів, яка досить добре відтворює експериментальні дані. Потім розрахунки поперечного перерізу фотонейтронів переробляються за допомогою визначеної функції сили γ -випромінювання за допомогою моделей NLD. В NLD розрахунках краще використовувати модель постійної температури (CTM), модель газу Фермі зі зсувом назад (BSFGM) і узагальнену надтекучу модель (GSM). Прогнози порівнюються між собою та наявними експериментальними даними. Для отримання всіх експериментальних даних використовується бібліотека EXFOR.

Ключові слова: моделі густини ядерних рівнів; поперечний переріз; силові функції γ -променів; фотонейтронні реакції; TALYS

EFFECT OF ELECTRIC FIELD MODULATION ON THE ONSET OF ELECTROCONVECTION IN A COUPLE STRESS FLUID[†]

 Chandrappa Rudresha*,  Chandrashekar Balaji,  Venkatesh Vidya Shree,  Sokalingam Maruthamanikandan

Department of Mathematics, School of Engineering, Presidency University, Bengaluru, India

*Corresponding Author: rudresha.c@presidencyuniversity.in, E-mail: maruthamanikandan@presidencyuniversity.in

Received August 20, 2022; revised September 23, 2022; accepted September 30, 2022

The problem of convective instability in a horizontal dielectric couple stress fluid layer with electric field modulation is investigated. The horizontal dielectric upper boundary layer is cooled, and the lower boundary layer is subjected to an isothermal boundary condition. The regular perturbation method is used to calculate the critical Rayleigh number and the corresponding wavenumber based on the small magnitude of the modulation. The strength of the system is characterised by a correction Rayleigh number, which is calculated as a function of the thermal, electrical, and couple voltage parameters and the frequency of the electric field modulation. Some of the well-known findings are taken up as special cases in this study. It is shown that the onset of convection can be accelerated or delayed by proper adjustment of various control parameters. The results of this study have potential implications for controlling electroconvection with a time-dependent electric field.

Keywords: Convection, Couple Stresses, Dielectric fluid, Electric field, Modulation.

PACS: 47.55.P-, 46.25.Hf, 77.84.Nh, 77.22.-d, 41.20.-q, 47.65.-d

1. Introduction

Electrohydrodynamic deals with the justice of the motion of fluids under the influence of electric energy. In microchannels, the interaction of electric fields with fluid flow has led to a variety of complex and interesting unstable events. In addition, the use of electrical energy to control fluids has been shown to be a very effective way to achieve many goals and functions in microfluidic devices.

When we add additives to oils or liquids, the energy contained in the liquid conflicts with the strength of the additives. This conflict leads to less fluid, which in turn leads to more stress for the couple. Couple stress fluid is the name for this type of fluid. The particular effects of couple stress fluid pressure on fluid is considered [1-3], and the basic statistical calculations for forcing couple stress are presented. Couple stress slows the onset of convection, while central infiltration accelerates the onset of convection [4-6], which allows to conclude that the system of stability exchange was heated in the couple stress fluid below the perforated area. As we have seen [7], the instability thresholds are changed when the fluid filling the porous medium exhibits pair-voltage behavior. They also assume that porous behavior is subject to small amplitude perpendicular oscillations. The convection variability of a chemically reactive fluid with coupling stresses in a porous medium heated from below is studied using a modified Darcy model by Taj et al. [8]. Coupling stresses improve system stability, and the stabilizing effect of coupling stresses is not diminished by the counteracting influence of chemical reactions and vice versa. In Maxwell-Cattaneo law [9], George & Thomas studied the consequences of gravity modulation and formation in the early phase of modulation within couple voltages. It is shown that by controlling the various regulating factors, the execution of convection transfer can be enhanced or postponed. The horizontal connection emphasizes the effect of the horizontal wavenumber and coupling stress fluid factors on the fluid layer, while the perforated parameters have a strong influence on the predominant fluid layer [10].

Analysis of convective instability in a horizontal viscoelastic dielectric fluid layer under the synchronous action of a direct alternating electric field with a precise temperature gradient was dealt with by Takashima & Ghosh [11]. It has been demonstrated that oscillatory processes of uncertainty occur only when the density of the fluid layer is less than 0.5 mm, and that the power of the current source in such a thin layer is more important than renewable energy. Sharma & Thakur [12] studied a porous material using a bottom heated conductive coupling voltage fluid in the absence of a homogeneous magnetic field. The coupling fluid and magnetic field retard the onset of thermal convection in a downward heated coupling stress in a porous medium in hydromagnetism, while the permeability of the medium accelerates it. Rayleigh-Bénard and Marangoni convection in dielectric fluids was studied by Maruthamanikandan [13]. This statement refers to the effects of the same internal heat dissipation and radiation. Thermorheological and electrical effects are considered in the management of the actual viscosity, such as the temperature function and the magnitude of the electric field. Rudraiah et al. [14] used a power method to study the stability of an electrohydrodynamic linear conductor flowing a pair of viscous fluid streams across a perforated medium in the presence of a uniform flexible electric field. It has been shown that the interaction of the electric current with the pair voltage is more efficient in stabilizing the pair voltages than for the conventional viscous Newtonian fluid. Shivakumara et al. [15] discuss the conjugation effects of electric body force, buoyancy force, Coriolis force and couple stress of the fluid in the formation of EHD instability. It is shown that

[†] *Cite as:* C. Rudresha, C. Balaji, V.V. Shree, and S. Maruthamanikandan, East Eur. J. Phys. 4, 104 (2022), <https://doi.org/10.26565/2312-4334-2022-4-09>
© C. Rudresha, C. Balaji, V.V. Shree, S. Maruthamanikandan, 2022

the influence of the couple stress parameter as well as Taylor number of the system of stability properties is considered in the situation of isothermal boundary. Using the method of small perturbation [16], the influence of variations of thermal conductivity on the onset of Rayleigh-Bénard instability in a horizontal layer of a Cattaneo-dielectric fluid under the simultaneous action of an alternating electric field and a temperature gradient was studied. The Rayleigh-Bénard solution of the Cattaneo-dielectric fluid layer is more stable than the Fourier dielectric fluid problem. Nagouda & Maruthamanikandan [17] studied the effect of radiation on Darcy electroconvection in the presence of an alternating electric field. It has been shown that the system is more stable in the presence of radiative heat transfer.

The Navier-Stokes equations in the Boussinesq approximation and the heat conduction equation in the presence of rigid boundary conditions are explored by Andreeva & Tkachenko [18] and Patochkina [19] as a linear steady-state system of equations. At the onset of Rayleigh-Bénard convection, gravity migrates in a weakly conducting couple stress fluid with a saturated porous layer, as shown by Sameena & Pranesh [20]. Shankar et al [21] found that the buoyancy of a vertical dielectric fluid layer between vertical surfaces maintained at constant but different temperatures drive the combined influence of a couple stress and a horizontal AC field on the accompanying shear flow stability in the horizontal direction. The effect of radiant heat on a dielectric fluid filled with an anisotropic porous medium is evaluated according to the Milne-Eddington standard and treated by Myson and Nagouda [22]. They showed that the conduction and radiation parameters stabilize the system. In addition, the critical Darcy-Rayleigh number shows the effects of stabilization when there are no coupling stresses and dielectric boundaries. The suitability of the stability exchange policy is evaluated and it is found that the marginal strength is a preferred mode over the oscillatory mode. The effect of intermittent temperature fluctuations in the open unstable surface of the semiconductor layer of the fluid leading to the instability of the first quasi-equilibrium fluid is studied by Smorodin & Gershuni [23]. They found that if the Marangoni and Rayleigh numbers do not vanish, the results depend on the accuracy of the set temperature.

Smorodin & Velarde [24] and Smorodin [25] found that destabilization and stabilization of the basic state is possible depending on the frequency of the electric field and the number of Rayleigh numbers. In the horizontal layer, only the positive response to the outgoing electric field is considered, since the dielectrophoretic force does not depend on the direction of the electric field and consequently does not change its direction during the fluctuation period. The stability of a viscous incompressible conductive cylindrically structured fluid in the external magnetic field of a vacuum arc current flowing through it may be utilized to investigate many features of such processes [26] and [27]. Rudresha et al. [28] investigated the effect of electric modulation on the onset of electrothermal convective instability of the horizontal dielectric porous layer using a stability analysis based on the assumption that the amplitude of the peripheral power is very small.

In many practical scenarios, it is possible to postpone or accelerate the onset of convection by modifying one of the determining factors. Several studies of the effects of modulation have shown that by applying the proper transitions to a control parameter, the conduction state can be stabilized or destabilized. As a result, the concept of applying transitions to a control parameter is critical because it provides an effective tool for addressing the problem of Rayleigh-Bénard convection in a pair of stress fluids, which is particularly relevant to engineering applications. Many heat transfer applications involving these couple stresses as a function now recognize that this can improve or reduce heat transfer in parallel with the final Newtonian convection. In this paper, we have investigated the effects of modulating an electric field on the boundary at the onset of convection in the dielectric fluid layer with couple stresses.

2. MATHEMATICAL FORMULATION

The problem at hand considers boundless horizontal dielectric fluid layer of couple stress fluid of thickness d . The lower surface and the upper surfaces are $z = 0$ and $z = d$ and they are sustained at constant temperatures T_1 and T_0 respectively and modulation electric potential $\phi = \pm U(\eta_1 + \eta_2 \cos \omega t)$ is retained on boundaries (see **Figure. 1**), where U is the magnitude of the modulation of the potential, ω is the frequency of modulation and η_1 and η_2 are the relative amplitudes of the components of constant and reciprocating potential difference.

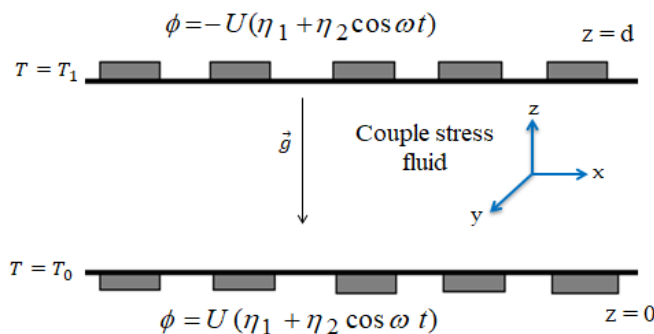


Figure 1. Schematic Diagram

The relationship between the shear tension and the flow field within a large fluid class is different from that of Newtonian fluids. These fluids are non-Newtonian in nature. The problem of Rayleigh-Bénard couple stress fluid

convection is particularly relevant in terms of technical applications. In heat transfer applications concerning this fluid as a functioning medium, it is now recognized that this might have improved or decreased heat transmission associated with the conventional Newtonian fluids. The relevant fundamental equations in the Boussinesq approximation [8], [11], and the dielectric constant are assumed to be linear functions of temperature.

$$\nabla \cdot \vec{q} = 0, \tag{1}$$

$$\rho_0 \left[\frac{\partial \vec{q}}{\partial t} + (\vec{q} \cdot \nabla) \vec{q} \right] = -\nabla p + \rho \vec{g} + (\mu_f \nabla^2 \vec{q} - \mu_c \nabla^4 \vec{q}) - \frac{1}{2} (\vec{E} \cdot \vec{E}) \nabla \varepsilon, \tag{2}$$

$$\rho_c \frac{\partial T}{\partial t} + \rho_c (\vec{q} \cdot \nabla) T = k \nabla^2 T, \tag{3}$$

where $\vec{q} = (x, y, z)$ is the velocity vector, T and \vec{E} are temperature and root mean square value of the electric field, p is the improved pressure, ε and ρ are respectively dielectric constant and the fluid density, μ_f and μ_c are viscosity of the fluid and constant of the material which determines the couple stress attribute called couple stress viscosity, k is thermal conductivity, \vec{g} is the gravity acceleration, ρ_0 is the density.

For most dielectric fluids, the dielectrophoretic force dominates the coulomb force. Hence the coulomb force has been omitted in Eq. (2). Consequently, the applicable Maxwell equations are

$$\nabla \cdot [\varepsilon \vec{E}] = 0, \tag{4}$$

$$\nabla \times \vec{E} = 0 \Rightarrow \vec{E} = -\nabla \phi, \tag{5}$$

$$\rho = \rho_0 [1 - \alpha (T - T_0)], \tag{6}$$

$$\varepsilon = \varepsilon_0 [1 - e (T - T_0)], \tag{7}$$

where α is the thermal expansion coefficient, ϕ is average quadratic value of the electric potential modulation. $e (> 0)$ is dielectric steady-state thermal expansion coefficient, which is tiny.

The fundamental condition is quiet and is provided by $\vec{q} = \vec{q}_b(z) = 0$; $\varepsilon = \varepsilon_b(z)$; $T = T_b(z)$; $\phi = \phi_b(z)$; $p = p_b(z)$; $\rho = \rho_b(z)$; and $\vec{E} = \vec{E}_b = [0, 0, E_b(z)]$, index b is a basic state and using these constraints we obtain

$$\phi_b = \frac{-2U(\eta_1 + \eta_2 \cos \omega t)}{\log(1 + e\beta d)} \log(1 + e\beta z) + U(\eta_1 + \eta_2 \cos \omega t), \tag{8}$$

and

$$E_b = \frac{2U(\eta_1 + \eta_2 \cos \omega t)}{d} (1 - e\beta z). \tag{9}$$

In order to investigate the stability of the basic state, we place over a negligible perturbation of the fundamental state of the form $\vec{q} = \vec{q}' = (u', v', w')$; $\varepsilon = \varepsilon_b + \varepsilon'$; $p = p_b + p'$; $T = T_b + T'$; $\vec{E} = \vec{E}_b + \vec{E}'$ and $\phi = \phi_b + \phi'$, where (u', v', w') , T' , p' , ε' , ϕ' and \vec{E}' are the velocity, temperature, pressure, dielectric constant, potential and electric field disturbances, respectively. Substituting these quantities into eqn. (1) to (7), and keeping the vertical component, the pressure from the momentum equation is removed. The resultant equations are nondimensionalized by using scalings $(x, y, z) = (dx^*, dy^*, dz^*)$; $\phi = 2U(\eta_1 + \eta_2 \cos \omega t) e \Delta T \phi^*$; $T = \Delta T T^*$; $t = d^2 t^* / \kappa$; and $w = \kappa w^* / d$. By eliminating (u', v', w') , T' , p' , ε' , ϕ' and \vec{E}' from the perturbation equations and to facilitate tilde suppression, we get the following nondimensionalized equations:

$$\left(\frac{1}{\text{Pr}} \frac{\partial}{\partial t} - \nabla^2 + C_s \nabla^4 \right) \nabla^2 w = R \nabla_1^2 T + R_e (1 + \eta_3 \cos \omega t)^2 \nabla_1^2 T + R_e (1 + \eta_3 \cos \omega t)^2 \frac{\partial}{\partial t} (\nabla_1^2 \phi), \tag{10}$$

$$\left(\nabla + \frac{\partial}{\partial z} \right) \phi = -\frac{\partial T}{\partial z}, \tag{11}$$

$$\left(\frac{\partial}{\partial t} - \nabla^2 \right) T = w, \tag{12}$$

where $R = \alpha\rho_0gd^3\Delta T/\mu_f\kappa$ is the thermal Rayleigh number, $Pr = \nu/\kappa$ is the Prandtl number, $C_s = \mu_c/\mu_f d^2$ is the couple stress parameter, $R_e = 4e^2U^2\beta\varepsilon_0\Delta Td\eta_1^2/\mu_f\kappa$ is the electrical Rayleigh number, $\eta_3 = \eta_2/\eta_1$ is the ratio of the amplitudes.

The assumed boundaries are stress-free and isothermal; therefore, the boundary conditions are given as follows.

$$w = \frac{\partial^2 w}{\partial z^2} = T = \phi = 0 \quad \text{at } z = 0 \quad \text{and } z = 1. \tag{13}$$

After eliminating the coupling between the Eqns. (10) to (12) we obtain the single equation for vertical component of velocity in the form

$$\left(\frac{1}{Pr} \frac{\partial}{\partial t} - 1 + C_s \nabla^2\right) \left(\frac{\partial}{\partial t} - \nabla^2\right) \nabla^6 w = \left[R \nabla^2 + R_e \nabla_1^2 (1 + \eta_3 f)^2\right] \nabla_1^2 w, \tag{14}$$

where $f = \cos \omega t$.

Also, the boundary conditions of the fluid layer are supposed to be isothermally free at temperature disturbances with decreasing couple stress and the following are the boundary conditions [28]:

$$w = \frac{\partial^2 w}{\partial z^2} = \frac{\partial^4 w}{\partial z^4} = \frac{\partial^8 w}{\partial z^8} = \frac{\partial^{10} w}{\partial z^{10}} = 0 \quad \text{at } z = 0, 1. \tag{15}$$

3. METHOD OF SOLUTION

We wish to determine the value of w and R of Eq. (14) by utilizing the control quantity η_3 . Thus, the values proper to the current problem differ from those of the ordinary orders of Bénard convection of magnitude η_3 . We wish to come up with the solution Eq. (14) by way of

$$\left. \begin{aligned} w &= w_0 + \eta_3 w_1 + \eta_3^2 w_2 + \dots \\ R &= R_0 + \eta_3 R_1 + \eta_3^2 R_2 + \dots \end{aligned} \right\}, \tag{16}$$

where R_0 is the unmodulated Rayleigh number ($\eta_3 = 0$), and R_i ($i \geq 2$) are the modulation adjustments to the critical Rayleigh number.

The odd powers of η_3 appearing in the second equation of (16) are not addressed because altering the sign of η_3 just alters the temporal origin, which has no effect on the stability problem. Therefore, R is independent of η_3 , and any odd powers of η_3 should be equal to zero (see [28]). To get the following system of equations, the extension (16) is changed into Eq. (14) and the coefficients of the different powers of η_3 are assimilated into one or another of the equations.

$$L w_0 = 0, \tag{17}$$

$$L w_1 = R_1 \nabla^2 \nabla_1^2 w_0 + 2 R_e f \nabla_1^2 w_0, \tag{18}$$

$$L w_2 = R_1 \nabla^2 \nabla_1^2 w_1 + R_2 \nabla^2 \nabla_1^2 w_0 + 2 R_e f \nabla_1^4 w_1, \tag{19}$$

where

$$L = \left(\frac{1}{Pr} \frac{\partial}{\partial t} - 1 + C_s \nabla^2\right) \left(\frac{\partial}{\partial t} - \nabla^2\right) \nabla^6 - R_0 \nabla_1^2 \nabla^2 - R_e \nabla_1^4. \tag{20}$$

Each of w_n is necessary to meet the boundary criteria (15). The marginal stable solution to the problem is overall solution of Eq. (17), i.e.

$$w_0 = \sin \pi z. \tag{21}$$

In the deficiency of electric field modulation, the zeroth order solution is like the Rayleigh-Bénard problem of the dielectric fluid with couple stress fluid. Shivakumara & Akkanagamma [15] carefully examined Rayleigh Bénard analysis of linear and nonlinear electroconvection in couple stress fluid without modulation. The system of stability is explored in

the absence of electric field modulation by introducing a vertical temperature perturbation with w_0 corresponding to the lowest mode of convection and the related eigenvalue. The associated eigenvalues are provided by

$$R_0^n = \frac{(\alpha^2 + n^2 \pi^2)^3 + C_s (\alpha^2 + n^2 \pi^2)^4}{\alpha^2} - \frac{R_e \alpha^2}{(\alpha^2 + n^2 \pi^2)}. \tag{22}$$

The least eigenvalue occurs at $n = 1$ for a fixed value of the wave number and is given by

$$R_0 = \frac{(\alpha^2 + \pi^2)^3 + C_s (\alpha^2 + \pi^2)^4}{\alpha^2} - \frac{R_e \alpha^2}{(\alpha^2 + \pi^2)}. \tag{23}$$

The solution to Eq. (18) is inhomogeneous due to the inclusion of reverberation factors. To satisfy the solvency condition, the time-independent element of the right part of Eq. (18) must be orthogonal to w_0 . $R_1 L_1 \nabla^2 \nabla_1^2 w_0$ is the time free term on the right side, hence $R_1 = 0$, as a result, all the odd coefficients, in other words, R_1, R_3, R_5, \dots in Eq. (16) should disappear. If we expand the right-hand side of Eq. (18), we obtain

$$Lw_1 = 2R_e \alpha^4 R_{eal} \left[\sum_{n=1}^{\infty} e^{-i\omega t} \sin n\pi z \right]. \tag{24}$$

We get w_1 by flipping the operator L term by term, as in

$$w_1 = 2R_e \alpha^4 R_{eal} \left[\sum_{n=1}^{\infty} \frac{e^{-i\omega t}}{L(\omega, n)} \sin n\pi z \right], \tag{25}$$

where

$$L(\omega, n) = - \left[\frac{\omega^2}{Pr} (n^2 \pi^2 + \alpha^2)^2 - (n^2 \pi^2 + \alpha^2)^4 - C_s (n^2 \pi^2 + \alpha^2)^5 \right] - i\omega \left\{ (n^2 \pi^2 + \alpha^2)^3 \left[1 + \frac{1}{Pr} \right] + C_s (n^2 \pi^2 + \alpha^2)^4 \right\} + R_0 \alpha^2 (n^2 \pi^2 + \alpha^2) + R_e \alpha^4$$

A term proportionate to $\sin(\pi z)$ is intervened in the solution of the homogenous equation corresponding to Eq. (24). Including this term for the overall solution of Eq. (24), on the other hand, it is equal to the reconfiguration of w_n as all the equals of $\sin(\pi z)$ may be combined to describe the new w_0 with the same meanings of w_1, w_2, \dots . As a result, we may conclude that w_0 is orthogonal to all other w_n 's. We find from Eq. (19)

$$Lw_2 = R_2 \nabla^2 \nabla_1^2 w_0 + 2R_e f \nabla_1^4 w_1. \tag{26}$$

We don't need to solve this equation; we just need to know R_2 , the first nonzero adjustment to R . The stable component of right-hand side should be orthogonal to $\sin(\pi z)$ for the solvability requirement to be met. Thus,

$$R_{2c} = \frac{2R_e^2 \alpha^6}{(\alpha^2 + \pi^2)} \left[\sum_{n=1}^{\infty} \frac{C_n}{D_n} \right], \tag{27}$$

where

$$C_n = \frac{\omega^2}{Pr} (n^2 \pi^2 + \alpha^2)^2 - (n^2 \pi^2 + \alpha^2)^4 - C_s (n^2 \pi^2 + \alpha^2)^5 + R_0 \alpha^2 (n^2 \pi^2 + \alpha^2) + R_e \alpha^4,$$

$$D_n = \left[\frac{\omega^2}{Pr} (n^2 \pi^2 + \alpha^2)^2 - (n^2 \pi^2 + \alpha^2)^4 \right] + \omega^2 \left\{ \frac{(n^2 \pi^2 + \alpha^2)^3 \left(1 + \frac{1}{Pr} \right)}{+ C_s (n^2 \pi^2 + \alpha^2)^4} \right\}^2.$$

4. RESULTS AND DISCUSSION

The perturbation procedure method is used to study the stability condition of a modulated dielectric fluid layer with a couple stress and an electric field. This approach is used to determine the Rayleigh number, wave number, and correction Rayleigh number. The present analysis assumes that the amplitude of the electric field modulation is very small in comparison to the central electric field, that convective currents are weak, allowing indirect effects to be ignored, and that the dielectric constant is considered to be a linear function of temperature. When the modulating frequency ω is low, violating these assumptions has a major impact on the outcomes. This is because the perturbation technique requires that amplitude of $\eta_3 w_1$ not exceeding that of w_0 , resulting in the condition $\omega > \eta_3$. As a result, the validity of the results is dependent on the modulating frequency value. When $\omega \ll 1$, the modulation time is large and impacts the full volume of the fluid. The impact of the modulation decreases at high frequencies because the electric force takes an average value, resulting in an unmodulated equilibrium state. Consequently, modulation has a significant effect only in small and moderate quantities of ω .

Before delving into the results displayed in Fig. 2-4, it is worth noting that the oscillatory mode will not be present in couple stresses (see [8]), and these figures demonstrate the fluctuation of R_{2c} versus ω for various parameters. As we can observe that, R_{2c} is always positive for entire array of ω values, showing that the effect of electric field modulation and couple stresses are causing the system to stabilize. Convection occurs later in the modulated system than in the unmodulated system. Fig. 2 depicts a plot of the critical correction Rayleigh number R_{2c} vs frequency modulation ω for different electrical Rayleigh number R_e values. In this picture, we see that the amplitude of the correction Rayleigh number R_{2c} decreases positively as the electrical Rayleigh number R_e climbs. This shows that R_e decreases the stabilizing effect for low values of frequency ω . However, the same pattern is seen for high values of ω . For large values of frequency, the modulation effect vanishes.

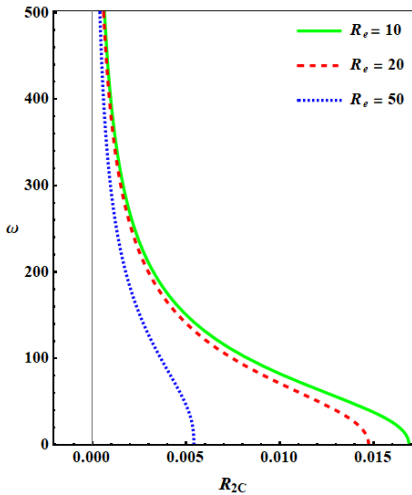


Figure 2. Variation R_{2c} vs ω for a different value of R_e with $C_s = 0.005$ and $Pr = 5$

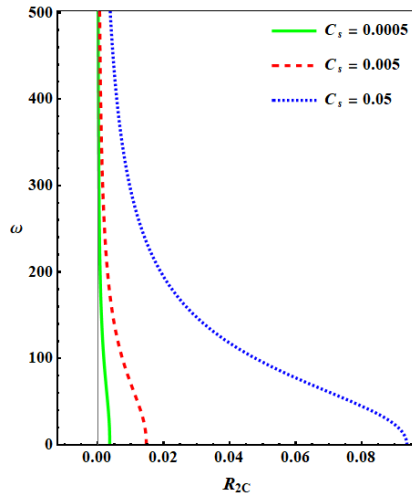


Figure 3. Variation R_{2c} vs ω for a different value of C_s with $R_e = 20$ and $Pr = 5$

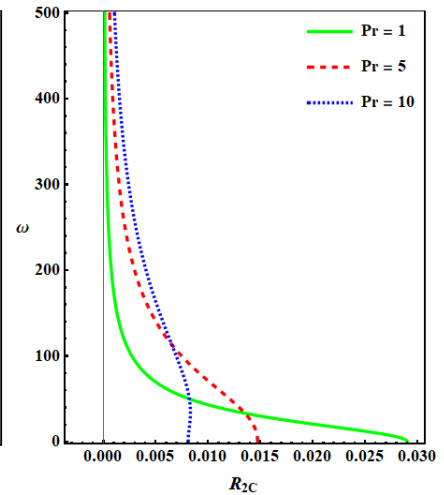


Figure 4. Variation R_{2c} vs ω for an individual values of Pr with $R_e=20$ and $C_s=0.005$

Fig. 3 depicts a plot of the critical correction Rayleigh number R_{2c} vs frequency ω for a different value of the couple stress parameter C_s . We observe from this graph that when the couple stress parameter C_s grows, so does R_{2c} , stabilizing the system. The concentration of suspended particles is represented by C_s . An explanation can be given to elucidate the impact of C_s on R_{2c} using Einstein's rule on suspension viscosity. Einstein's equation for suspended particles is $\mu = \mu_0(1 + 2.5\alpha\delta)$, where μ and μ_0 are the viscosity of the suspension and clean fluid, respectively, α is the form factor, and δ is the volume ratio of suspended particles. α equals 1 for spherical particles and exceeds 1 for other structures such as ellipsoids, rods, etc. To comprehend a change in the viscosity of a suspension with concentration, remember that the viscosity of any fluid is related to the intertempance of mechanical energy into heat inside the fluid. Other parameters influencing suspension viscosity include the viscosity of the carrier liquid, particle contact, particle stiffness or deformability, temperature, and electrical conductivity. We simply assume that the viscosity of a suspension is greater than the viscosity of the carrier liquid. For low concentrations, the assumed viscosity concentration relation holds true. In the event of larger concentrations, the Einstein relation must be supplemented with a quadratic term. Given the preceding explanation, we believe that the Prandtl numbers of fluids containing suspended particles are greater than those of fluids without suspended particles. The modulation effect, on the other hand, fades away at a high frequency. This is because the electric force adopts a mean value, resulting in the unmodulated case's equilibrium condition. As a result, in our research, we only employed a moderate value. It should be noted that the value of the Prandtl number is assumed to be larger than that of clean fluid due to the existence of suspended particles in the fluid and Einstein's connection to viscosity.

Fig. 4 depicts the R_{2c} against ω for various Prandtl numbers Pr . When Pr increases for small values of ω , R_{2c} decreases, but increases for moderate and large values of frequencies, indicating that the effect of Pr on the electric field

modulation on a couple stress fluid is to reduce the stabilizing effect for small values of ω , and to increase the stabilising effect for large values of ω .

5. CONCLUSIONS

We conclude from the research carried out that the effects of electric field modulation and couple stress fluid on the commencement of electroconvection in a dielectric fluid layer cause convection to be delayed. Depending on frequency, the electrical Rayleigh number has a stabilizing and destabilizing impact. The system stability is strongly influenced by the couple stress parameter, and the Prandtl number diminishes the stabilizing impact. At intermediate frequencies, this impact is stronger. Finally, it is discovered that electric field modulation may either stabilize or destabilize the system depending on the values of the parameters, and that it disappears for high frequency values.

ORCID IDs

- 📍 Chandrappa Rudresha, <https://orcid.org/0000-0002-0958-4220>
- 📍 Chandrashekar Balaji, <https://orcid.org/0000-0002-3832-935X>
- 📍 Venkatesh Vidya Shree, <https://orcid.org/0000-0003-1554-8258>
- 📍 Sokalingam Maruthamanikandan, <https://orcid.org/0000-0001-9811-0117>

REFERENCES

- [1] V.K. Stokes, "Couple stresses in fluids", *Phys. Fluids*, **9**(9), 1709 (1966). <https://doi.org/10.1063/1.1761925>
- [2] T. Ariman, "Couple Stresses in Fluids", *Phys. Fluids*, **10**(11), 2497 (1967). <https://doi.org/10.1063/1.1762061>
- [3] V.K. Stokes, "Effects of couple stresses in fluids on the creeping flow past a sphere", *Phys. Fluids*, **14**(7), 1580 (1971). <https://doi.org/10.1063/1.1693645>
- [4] R.C. Sharma, and S. Sharma, "On couple-stress fluid heated from below in porous medium", *Indian J. Phys.* **75**(2), 137 (2001).
- [5] M.S. Malashetty, S.N. Gaikwad, and M. Swamy, "An analytical study of linear and non-linear double diffusive convection with Soret effect in couple stress liquids", *Int. J. Therm. Sci.* **45**(9), 897 (2006). <https://doi.org/10.1016/j.ijthermalsci.2005.12.005>
- [6] M.S. Malashetty, I.S. Shivakumara, and S. Kulkarni, "The onset of convection in a couple stress fluid saturated porous layer using a thermal non-equilibrium model", *Phys. Lett. Sect. A Gen. At. Solid State Phys.* **373**(7), 781 (2009). <https://doi.org/10.1016/j.physleta.2008.12.057>
- [7] S. Saravanan, and D. Premalatha, "Effect of couple stress on the onset of thermovibrational convection in a porous medium", *Int. J. Therm. Sci.* **57**, 71 (2012). <https://doi.org/10.1016/j.ijthermalsci.2012.02.013>
- [8] M. Taj, S. Maruthamanikandan, and S.K. Akbar, "Effect of Chemical Reaction on Convective Instability in a Horizontal Porous Layer Saturated with a Couple-Stress Fluid", *Int. J. Eng. Res. Appl.* **3**(2), 1742 (2013). <https://citeseerx.ist.psu.edu/viewdoc/download?jsessionid=26C9EE742F44CA86219F8CA53B476180?doi=10.1.1.414.6306&rep=rep1&type=pdf>
- [9] S. George and M. Thomas, "Effect of Gravity Modulation and Internal Heat Generation on Rayleigh-Bénard Convection in Couple Stress Fluid with Maxwell-Cattaneo Law", *Int. J. Appl. Eng. Res.* **13**(5), 2688 (2018).
- [10] R. Sumithra and S. Venkatraman, "Darcy-Benard Marangoni Convection in a Composite Layer Comprising of Couple Stress Fluid", *Int. J. Appl. Eng. Res.* **15**(7), 659 (2020). https://www.ripublication.com/ijaer20/ijaerv15n7_07.pdf
- [11] M. Takashima, and A. K. Ghosh, "Electrohydrodynamic Instability in a Viscoelastic Liquid Layer", *J. Phys. Soc. Japan*, **47**(5), 1717 (1979). <https://doi.org/10.1143/JPSJ.47.1717>
- [12] R.C. Sharma, and K.D. Thakur, "On couple stress fluid heated from below in porous medium in hydromagnetics", *Czechoslov. J. Phys.* **50**(6), 753 (2000). <https://doi.org/10.1023/A:1022886903213>
- [13] S. Maruthamanikandan, "Convective instabilities in Newtonian ferromagnetic, dielectric and other complex liquids", PhD Thesis, Bangalore University, Bangalore, India, 2005.
- [14] N. Rudraiah, B.M. Shankar, and C.O. Ng, "Electrohydrodynamic stability of couple stress fluid flow in a channel occupied by a porous medium", *Spec. Top. Rev. Porous Media: An International Journal*, **2**(1), 11 (2011). <https://doi.org/10.1615/SpecialTopicsRevPorousMedia.v2.i1.20>
- [15] I.S. Shivakumara, M. Akkanagamma, and C.O. Ng, "Electrohydrodynamic instability of a rotating couple stress dielectric fluid layer", *Int. J. Heat Mass Transf.* **62**(1), 761 (2013). <https://doi.org/10.1016/j.ijheatmasstransfer.2013.03.050>
- [16] S. Maruthamanikandan, and S.S. Nagouda, "Convective Heat Transfer in Maxwell-Cattaneo Dielectric Fluids", *Int. J. Comput. Eng. Res.* **3**, 347 (2013). <https://cutt.ly/AVrcoGi>
- [17] S.S. Nagouda, and S. Maruthamanikandan, "Rayleigh-Bénard Convection in a Horizontal Layer of Porous Medium Saturated with a Thermally Radiating Dielectric Fluid", *IOSR J. Math.* **11**(3), 01 (2015). <https://www.iosrjournals.org/iosr-jm/papers/Vol11-issue3/Version-3/A011330110.pdf>
- [18] O.L. Andreeva, and V.I. Tkachenko, "Analytical Solution and Neutral Curves of the Stationary Linear Rayleigh Problem with Rigid or Mixed Boundary Conditions in Cylindrical Geometry", *East Eur. J. Phys.* **2**(4), 52 (2015). <https://periodicals.karazin.ua/eejp/article/view/5118/4672>
- [19] O.L. Patochkina, Yu.G. Kazarinov, and V.I. Tkachenko, "Physical model of the dependence of the Nusselt number on the Rayleigh number", *ZhTF*, **66**(11), 23 (2016). (in Russian).
- [20] S. Tarannum, and S. Pranesh, "Effect of Gravity Modulation on the Onset of Rayleigh-Bénard Convection in a Weak Electrically Conducting Couple Stress Fluid with Saturated Porous Layer", *Int. J. Eng. Res.* **5**(01), 2016. <https://cutt.ly/7VrvvJY>
- [21] B.M. Shankar, J. Kumar, and I.S. Shivakumara, "Stability of natural convection in a vertical dielectric couple stress fluid layer in the presence of a horizontal AC electric field", *Appl. Math. Model.* **40**(9-10), 5462 (2016). <https://doi.org/10.1016/j.apm.2016.01.005>
- [22] S. Myson, and S.S. Nagouda, "Convective instability analysis of couple-stress dielectric fluid saturated anisotropic porous medium with radiation effect", *Multidiscip. Model. Mater. Struct.* **16**(5), 1019 (2020). <https://doi.org/10.1108/MMMS-08-2019-0149>

- [23] B.L. Smorodin, G.Z. Gershuni, and M.G. Velarde, "On the parametric excitation of thermoelectric instability in a liquid layer open to air", *Int. J. Heat Mass Transf.* **42**, 3159 (1999). [https://doi.org/10.1016/S0017-9310\(98\)00351-2](https://doi.org/10.1016/S0017-9310(98)00351-2)
- [24] B.L. Smorodin, and M.G. Velarde, "On the parametric excitation of electrothermal instability in a dielectric liquid layer using an alternating electric field", *J. Electrostat.* **50**, 205 (2001). [https://doi.org/10.1016/s0304-3886\(00\)00036-x](https://doi.org/10.1016/s0304-3886(00)00036-x)
- [25] B.L. Smorodin, "The Behaviour of Low Conducting Liquid in Modulated Electric Field", in: *Proc. 14th International Conf. Dielectr. Liq.*, (IEEE, Graz, Austria, 2002). pp. 425–428, 2002. <https://doi.org/10.1109/ICDL.2002.1022783>
- [26] L. Bozbiei, B. Borts, Y. Kazarinov, A. Kostikov, and V.I. Tkachenko, "Experimental Study of Liquid Movement in Free Elementary Convective Sells", *Energetika*, **61**(2), 45 (2015). (in Russian)
- [27] O.L. Andrieieva, B.V. Borts, A.F. Vanzha, I.M. Korotkova, and V.I. Tkachenko, "Stability of a Viscous Incompressible Conducting Liquid Layer of a Cylindrical Shape in an Inhomogeneous Temperature Field and a Magnetic Field of a Vacuum Arc Current Through It", *PAST*. **3**, 91 (2021). https://vant.kipt.kharkov.ua/ARTICLE/VANT_2021_3/article_2021_3_91.pdf
- [28] C. Rudresha, C. Balaji, V. Vidya Shree, S. Maruthamanikandan, "Effect of Electric Field Modulation on Electroconvection in a Dielectric Fluid-Saturated Porous Medium", *Journal of Mines Metals and Fuels*. **70**(3A), 35 (2022). <https://doi.org/10.18311/jmmf/2022/30665>
- [29] S. Maruthamanikandan, N.M. Thomas, and S. Mathew, "Bénard-Taylor ferroconvection with time-dependent sinusoidal boundary temperatures", *J. Phys. Conf. Ser.* **1850**(1), 012061 (2021). <https://doi.org/10.1088/1742-6596/1850/1/012061>

ВПЛИВ МОДУЛЯЦІЇ ЕЛЕКТРИЧНОГО ПОЛЯ НА ПОЧАТОК ЕЛЕКТРОКОНВЕКЦІЇ В ПАРНІЙ НАПРУЖЕНІЙ РІДИНІ

Чандраппа Рудреша, Чандрашекар Баладжі, Венкатеш Відья Шрі, Сокалінгам Марутаманікандан

Факультет математики, Інженерна школа, Президентський університет, Бенгалуру, Індія

Досліджено проблему конвективної нестійкості в горизонтальному діелектричному парному напруженому шарі рідини з модуляцією електричного поля. Горизонтальний діелектричний верхній граничний шар охолоджується, а нижній граничний шар піддається ізотермічним граничним умовам. Для обчислення критичного числа Релея та відповідного хвильового числа використовується метод регулярних збурень на основі малої величини модуляції. Міцність системи характеризується коригувальним числом Релея, яке розраховується як функція теплових, електричних параметрів, параметрів напруги пари та частоти модуляції електричного поля. В цьому дослідженні деякі з добре відомих висновків розглядаються як окремі випадки. Показано, що початок конвекції можна прискорити або відстрочити належним налаштуванням різних контрольних параметрів. Результати цього дослідження мають потенційні наслідки для керування електроконвекцією за допомогою залежного від часу електричного поля.

Ключові слова: конвекція, парна напруга, діелектрична рідина, електричне поле, модуляція

EFFECT OF MAGNETIC FIELD DEPENDENT VISCOSITY ON DARCY-BRINKMAN FERROCONVECTION WITH SECOND SOUND[†]

✉ Venkatesh Vidya Shree, ✉ Chandrappa Rudresha, ✉ Chandrashekar Balaji,
✉ Sokalingam Maruthamanikandan

Department of Mathematics, School of Engineering, Presidency University, Bangalore 560064, India

Phone No.: 7975996012, 8951364117, 9066348664, 763926678

**Correspondence Author: vidya.shreev@presidencyuniversity.in,*

E-mail: rudresha.c@presidencyuniversity.in, E-mail: balaji.c@presidencyuniversity.in,

E-mail: maruthamanikandan@presidencyuniversity.in

Received September 8, 2022; accepted November 12, 2022

The problem of buoyancy-driven convection in a ferromagnetic fluid saturated porous medium with the Maxwell-Cattaneo law and MFD viscosity is investigated by the method of small perturbation. The fluid motion is described using the Brinkman model. It is assumed that the fluid and solid matrices are in local thermal equilibrium. For simplified boundary conditions, the eigenvalue problem is solved exactly and closed form solutions for stationary instability are obtained. Magnetic forces and second sound were found to enhance the beginning of Brinkman ferroconvection. However, ferroconvection is hampered when the porous parameters are increased. The results show that MFD viscosity inhibits the beginning of Darcy-Brinkman ferroconvection and that MFD viscosity stabilizing effect is decreased when the magnetic Rayleigh number is significant. Furthermore, it is demonstrated that oscillatory instability arises before stationary instability, assuming that the Prandtl and Cattaneo numbers are sufficiently large.

Keywords: Ferrofluid, MFD viscosity, Porous Media, Magnetic Field, Second Sound

PACS: 47.65. Cb; 83.80. Gv; 47.56. +r; 47.65Cb;

1. INTRODUCTION

The term "ferromagnetism" refers to materials that have a significant magnetic attraction to other materials that have permanent magnetic characteristics. The presence of spontaneous magnetization caused by the parallel spin alignment of molecular magnetization causes significant magnetism in ferromagnetic materials. In 1907, Weiss suggested an instrument for the appearance of spontaneous magnetic induction. He believed that ferromagnetic materials have an effective field called the molecular field. As a result of their extraordinary physical features, the thermoconvective instability of magnetic fluids is becoming more important. The viscosity of ferrofluid appears to be a well-defined concept. Magnetic liquids are used in a variety of fields, including variable-speed machine tools, pharmaceuticals, high-speed noiseless printers and other equipment. Convective phenomena are studied in high-capacity capacitor devices because ferrofluid is used as both a core material and a transformer coolant.

When an external magnetic field is imposed on a horizontal layer of ferromagnetic fluid having a changing attractive susceptibility, Finlayson [1] described how a temperature gradient generates an unequal attractive body force, which leads to thermomagnetic convection. Gotoh and Yamada [2] looked into the fluctuation of a uniform magnetic fluid layer that was confined between strong magnets and heated from below. In the presence of a uniform vertical magnetic field and a strong vertically attractive field, Stiles and Kagan [3] studied the heat conductivity instability of flat film ferrofluids. Venkatasubramanian and Kaloni [4] explored how rotation affects the initiation of convection in a horizontal layer of ferrofluids revolving about their vertical axis and heated from below. Sekar et al. [5] analyzes the linear theory, which has been applied to how rotation affects ferrothermohaline convection. When comparing the stationary and oscillatory modes for heat transfer, it was discovered that the stationary mode is favored.

Porous media is a substance composed of a solid matrix with a network of voids. The firm structure would either be stiff or slightly deformable. In a natural porous medium, the arrangement of pores is unusual in terms of shape and size. Natural porous media include beach stone, mudstone, granite, rye bread, wood and the human lung.

Lapwood [6] investigated the distribution firmness of a fluid layer in a permeable material exposed to a vertical temperature gradient as well as the prospect of convective movement. Wooding [7] explores the circumstances that lead to instability. Kordylewski and Karjewski [8] studied the relationship between synthetic reactions and free advection in permeable media scientifically. Using the Brinkman model, Vaidyanathan et al. [9] analyzed the performance of MFD viscosity on ferroconvection. Ramanathan and Suresh [10] studied the impact of MFD viscosity on the initiation of ferroconvection in an anisotropic, closely packed porous material. Nisha Mary Thomas and Maruthamanikandan [11] studied the effect of a time-periodically varying gravity field on the initiation of convective flow in a magnetic fluid-saturated porous surface. The value of the Darcy-Rayleigh number and the resultant wavenumber are estimated using the regular perturbation method based on the tiny amplitude of modulation. Sekhar et al. [12] investigates the effect of throughflow on the beginning of thermal convection in ferromagnetic liquids with temperature and magnetic field

[†] **Cite as:** V.S. Venkatesh, R. Chandrappa, B. Chandrashekar, M. Sokalingam, East Eur. J. Phys. 4, 112 (2022), <https://doi.org/10.26565/2312-4334-2022-4-10>

© V.V. Shree, C. Rudresha, C. Balaji, S. Maruthamanikandan, 2022

dependent viscosity for all feasible barrier configurations. Soya Mathew and Maruthamanikandan [13] discuss the subject of ferroconvective porous medium uncertainty using an inverse linear viscosity-temperature relationship. The Galerkin procedure is utilized to govern the critical values of porous media magnetic volatility under more accurate boundary circumstances. Vidya Shree et.al [14] study the effect of variable viscosity on the convective instability of a fluid saturated a porous medium subject to gravitational filed.

Thermal wave propagation is also known as the second sound effect. The non-classical Maxwell-Cattaneo heat flux law employs wave-type heat transport to avoid the physically unacceptable problem of infinite heat propagation speed. The energy equation in this study is essentially a damped wave equation, making it hyperbolic rather than parabola. Knowledge of second sounds has provided a rich source of information through the study and understanding of the superfluid state. Sound is not a sound wave in any sense, but rather a temperature or entropy wave. It was recently discovered that this is more than just a low temperature, but that it has important applications in fields such as skin burns, phase changes, biological materials, and nanofluids.

Gurtin and Pipkin [15] investigated a general principle of thermal conduction in nonlinear analysis, including memories, a concept having a finite propagation speed. Straughan and Franchi [16] address Benard advection when the Maxwell-Cattaneo heat flow law is utilized in place of the ordinary Fourier theory of thermal conductivity. Dauby et al. [17] studied the impact of applying general Fourier equalities instead of Fourier’s regulation. The problem of thermal convection is investigated for a layer of fluid when the heat flux law of Cattaneo is adopted by Straughan [18]. Soya Mathew [19] studied free convection in a ferrous liquid-filled porous material subjected to the non-classical Maxwell Cattaneo law, focusing on how the presence of both pore spaces and second sound affected the stability threshold for the onset of ferroconvection. Mahanthesh [20] examines the instability caused by the Maxwell–Cattaneo heat flux, along with internal heat generation and absorption, in non-Newtonian Casson dielectric fluid. Soya Mathew and Maruthamanikandan [21] are exploring the problem of porous medium convectonal fluctuation in a second sound ferromagnetic fluid in order to investigate the possible range of variables that might result in oscillatory porous medium ferroconvection.

Under these conditions, the current paper is devoted to investigating qualitatively the effect of thermal wave propagation on the onset of ferroconvection in a horizontal porous layer. The normal mode technique is used in the linear stability analysis. The Galerkin technique is used to determine the critical values of porous media thermomagnetic instability while taking into account more realistic boundary conditions. The modified Darcy-Brinkman law is used to model the momentum equation, and the heat flux model of Cattaneo is used to account for a thermal wave of finite speed.

2. MATHEMATICAL FORMULATION

A Cattaneo magnetic fluid saturated permeable film is considered, which is surrounded by two infinitely long horizontal surfaces of finite thickness. From Fig.1, the liquid film is cool at a temperature of T_0 from above and hot at a temperature of T_1 from below. A magnetic field behaves as though it is equal to the vertical z-axis and gravity is a vertically behaving downward force.

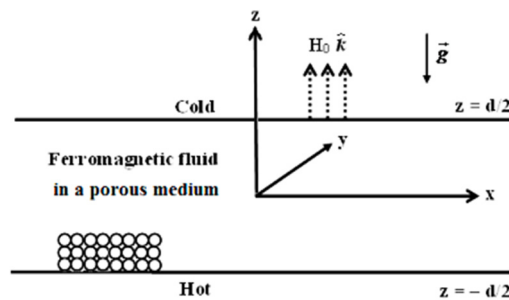


Figure 1. Schematic of the Problem

The problem of governing equations is as follows:

$$\nabla \cdot \vec{q} = 0 \tag{1}$$

$$\rho_0 \left[\frac{1}{\varepsilon} \frac{\partial \vec{q}}{\partial t} + \frac{1}{\varepsilon^2} (\vec{q} \cdot \nabla) \vec{q} \right] = -\nabla p + \rho \vec{g} - \frac{\mu_f}{k} \vec{q} + \nabla \cdot (\vec{H}\vec{B}) + \nabla \cdot \left[\vec{\mu}_f (\nabla \vec{q} + \nabla \vec{q}^T) \right] \tag{2}$$

$$\begin{aligned} \varepsilon \left[\rho_0 C_{v,H} - \mu_0 \vec{H} \cdot \left(\frac{\partial \vec{M}}{\partial T} \right)_{v,H} \right] \left[\frac{\partial T}{\partial t} + (\vec{q} \cdot \nabla) T \right] + (1-\varepsilon) (\rho_0 C)_s \frac{\partial T}{\partial t} \\ + \mu_0 T \left(\frac{\partial \vec{M}}{\partial T} \right)_{v,H} \cdot \left[\frac{\partial \vec{H}}{\partial t} + (\vec{q} \cdot \nabla) \vec{H} \right] = -\nabla \cdot \vec{Q} \end{aligned} \tag{3}$$

$$\tau \left[\frac{\partial \bar{Q}}{\partial t} + (\bar{q} \cdot \nabla) \bar{Q} + \bar{\omega} \times \bar{Q} \right] = -\bar{Q} - k_1 \nabla T \tag{4}$$

$$\rho = \rho_0 \left[1 - \alpha (T - T_a) \right] \tag{5}$$

$$M = M_0 + \chi (H - H_0) - K (T - T_a) \tag{6}$$

In equations 1–6, numerous physical quantities appear and the fundamental assumptions have their usual meaning. Finlayson [1], Soya Mathew and Maruthamanikandan [11]. Following examination, Maxwell's approximations suitable for the problem exist.

$$\nabla \cdot \bar{B} = 0, \quad \nabla \times \bar{H} = 0, \quad \bar{B} = \mu_0 (\bar{H} + \bar{M}) \tag{7}$$

3. Stability analysis

The following dimensionless equations can be obtained by applying the stability analysis of small perturbations encompassing normal modes (Finlayson [1], Soya Mathew and Maruthamanikandan [13]).

$$\begin{aligned} \frac{\sigma}{Pr} (D^2 - a^2) W &= -(R + N) a^2 \theta - Da^{-1} g(z) (D^2 - a^2) W + Na^2 D\phi \\ + 2\Lambda V^2 g^3(z) (D^2 + a^2) W &- 2\Lambda V g^2(z) (D^2 - a^2) DW \\ + \Lambda g(z) (D^2 - a^2) W & \end{aligned} \tag{8}$$

$$(1 + 2C\sigma)(\lambda\sigma\theta - W) + C(D^2 - a^2) - (D^2 - a^2)\theta = 0 \tag{9}$$

$$(D^2 - M_3 a^2)\phi - D\theta = 0 \tag{10}$$

where N is the magnetic Rayleigh number, R is the thermal Rayleigh number, Da^{-1} is the inverse Darcy number, Λ is the Brinkman number, C is the Cattaneo number, Pr is the Prandtl number, M_3 is the magnetization parameter.

The boundary conditions encompassing Rigid-Rigid and isothermal surfaces are

$$\begin{aligned} W = DW = \theta = 0 \quad \text{at } z = \pm \frac{1}{2} \\ D\phi + \frac{a\phi}{1 + \chi} = 0 \quad \text{at } z = \frac{1}{2} \\ D\phi - \frac{a\phi}{1 + \chi} = 0 \quad \text{at } z = -\frac{1}{2} \end{aligned} \tag{11}$$

4. Stationary instability

It can be shown that the principle of exchange of stabilities is valid. Hence the onset of the stationary mode of convection ($\sigma = 0$), has been analyzed.

$$\begin{aligned} \Lambda g(z) (D^2 - a^2) W - 2\Lambda V g^2(z) (D^2 - a^2) DW + 2\Lambda V^2 g^3(z) (D^2 + a^2) W \\ - Da^{-1} g(z) (D^2 - a^2) W - (R + N) a^2 \theta + Na^2 D\phi = 0 \end{aligned} \tag{12}$$

$$W - C(D^2 - a^2)W + (D^2 - a^2)\theta = 0 \tag{13}$$

$$(D^2 - M_3 a^2)\phi - D\theta = 0 \tag{14}$$

5. Method of Solution

The governing equations (12) – (14) together with the boundary condition (11) constitute an eigenvalue problem with R and N as an eigenvalue. To solve the resulting eigenvalue problem, Galerkin method is used. According, the variables are written in a series of trial functions as

$$W_i = \left(z^2 - \frac{1}{4} \right)^{i+1}, \quad \theta_i = \left(z^2 - \frac{1}{4} \right)^i, \quad \phi_i = z^{2i-1} \tag{15}$$

W_i, θ_i and ϕ_i will be represented by the power series satisfying the respective boundary conditions.

RESULTS AND DISCUSSION

The research concerns the effects of MFD viscosity on Darcy-Brinkman ferromagnetic instability with the Maxwell-Cattaneo heat conduction law. The non-classical Maxwell-Cattaneo heat flux law includes a wave type heat transfer and does not suffer from the physically unacceptable drawback of infinite heat propagation speed. The eigenvalues are obtained for rigid-rigid, isothermal boundary conditions. The thermal Rayleigh number R , describing the stability of the system, is taken as a function of the different parameters of the study. The fixed values of C , M_3 , Da^{-1} , V , χ , Λ are taken to be 0.001, 5, 5, 0.5, 3 and 3 respectively. The numerical implementation package MATHEMATICA is used to define the eigenvalue expressions and the associated critical numbers. The numerical values are given in tables 1 and 2 respectively.

Fig. 2 depicts the dependency of the critical thermal Rayleigh number R_c on the magnetic Rayleigh number N for varying values of C and fixed values of M_3 , Da^{-1} , V , χ and Λ respectively. The ratio of the magnetic and dissipative forces is known as the magnetic Rayleigh number. It is shown that R_c reduces monotonically as N and C levels rise, illustrating that N and C both enhance ferroconvection at lower values of R_c . As a result, the two physical mechanisms, second sound and magnetic mechanism destabilize the system. In other words, the existence of a magnetic field and second sound improves heat transport and hence speeds up the commencement of Darcy-Brinkman ferroconvection. It is important to note that the effect of C enhances the destabilizing effect of N simultaneously. The destabilizing effect of C is due to the fact that the energy equation under consideration is functionally a damped wave equation and so hyperbolic rather than parabolic.

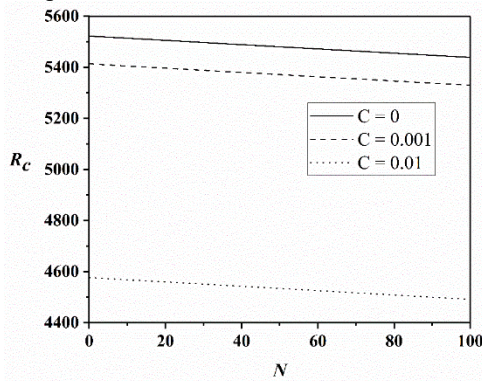


Figure 2. Variation of R_c with N for different values of the Cattaneo number C

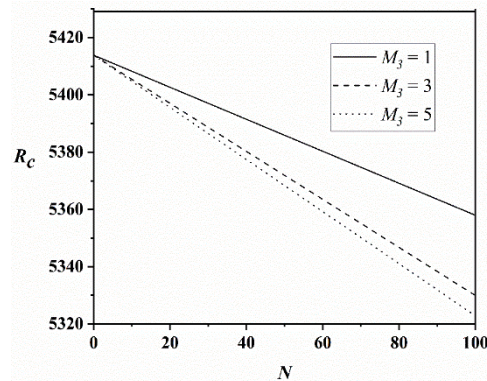


Figure 3. Variation of R_c with N for different values of the magnetization parameter M_3

The magnetic equation of state's departure from linearity is represented by the parameter M_3 (See Fig. 3). We observe that when M_3 increases, R_c monotonically decreases. As the magnetic equation of state gets more nonlinear, the threshold of ferroconvection in a porous layer with second sound advances. Furthermore, when N is small, the destabilizing effect of M_3 is almost minor.

Figs. 4 and 5 show how porosity factors Da^{-1} and Λ affect the start of ferroconvection. When both Da^{-1} and Λ are raised, the onset of ferroconvection is significantly inhibited. It could be attributable to the fact that increasing Da^{-1} reduces the permeability of the porous material, which slows fluid movement. However, it is important to emphasize that the Brinkman model is based on an effective viscosity $\bar{\mu}_f$ that differs from the fluid viscosity μ_f denoted by the Brinkman number. As a result, increasing Λ increases the viscous effect, which slows fluid movement. Therefore, in the presence of a Darcy-Brinkman porous medium, greater heating is necessary to initiate ferroconvection. It is worth noting that when both Da^{-1} and Λ are large, the ferrofluid layer is slightly destabilized by the magnetic process.

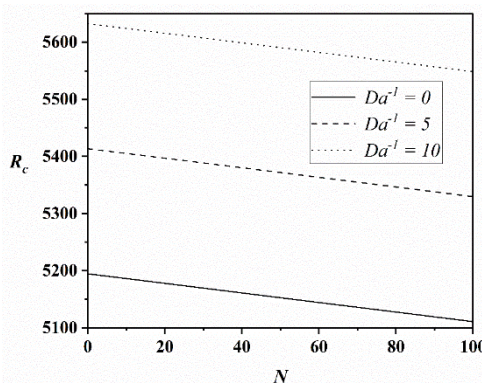


Figure 4. Variation of R_c with N for different values of inverse Darcy number Da^{-1} .

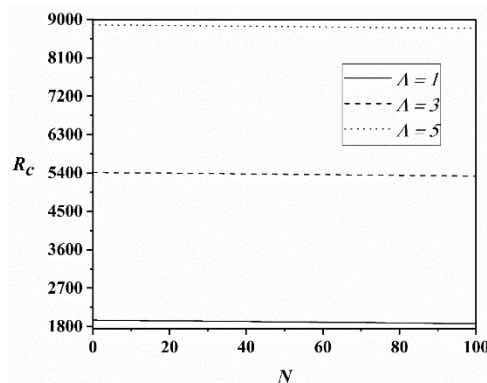


Figure 5. Variation of R_c with N for different values of Brinkman Number Λ .

Fig. 6 demonstrates that an increase in the magnetic susceptibility χ results in the same trend for R_c , indicating that the stabilizing effects confining nature is minimal. Computations also show that the convection cell size is more sensitive to the porous parameters Λ and Da^{-1} , while the magnetic parameters M_3 and χ are the inverse.

In Fig. 7, the magnetic field dependent variable viscosity parameter increases from 0 to 1, it stabilizes the system. If we increase the variable viscosity, the critical thermal Rayleigh number also increases. This is because the magnetization of the magnetic fluid increases as the strength of the magnetic field increases.

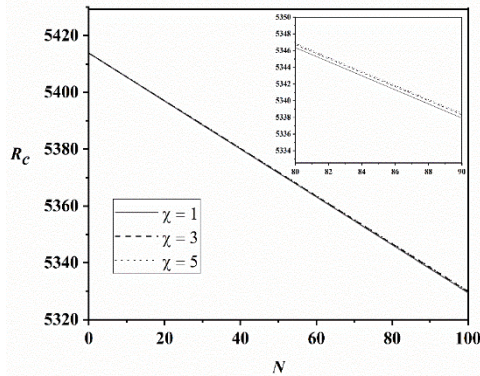


Figure 6. Variation of R_c with N for different values of magnetic susceptibility χ .

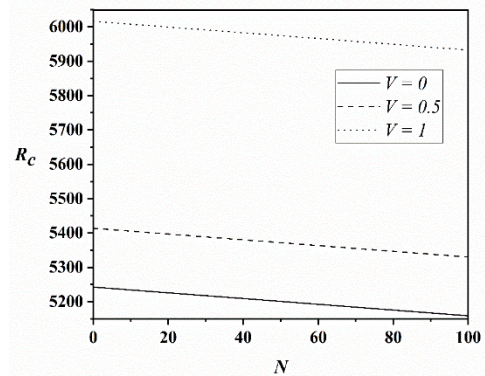


Figure 7. Variation of R_c with N for different values of variable viscosity V .

Table 1. Dependence of a_c with N and C

N	a_c		
	$C = 0$	$C = 0.001$	$C = 0.01$
0	3.1267	3.1485	3.3324
20	3.1278	3.1496	3.3337
40	3.1288	3.1507	3.3349
60	3.1299	3.1517	3.3363
80	3.1309	3.1528	3.3377
100	3.132	3.1539	3.3389

Table 2. Dependence of a_c with N and V

N	a_c		
	$V = 0$	$V = 0.5$	$V = 1$
0	3.1443	3.1485	3.1653
20	3.1454	3.1496	3.1663
40	3.1466	3.1506	3.1673
60	3.1477	3.1517	3.1683
80	3.1488	3.1528	3.1693
100	3.1499	3.1539	3.1703

CONCLUSIONS

The effect of variable viscosity in non-classical heat conduction on the onset of Rayleigh-Bénard instability in a horizontal layer of Darcy-Brinkman porous medium saturated with a Boussinesq-Cattaneo-ferromagnetic liquid and subjected to the simultaneous action of a vertical magnetic field and a vertical temperature gradient is studied analytically using the small perturbation method. A linearized convective instability analysis is performed since both the magnetic and buoyancy mechanisms are operative. Because the principle of exchange of stabilities applies to the current investigation, instability criteria are derived in terms of the stationary Rayleigh number R , wavenumber a , Cattaneo number C and magnetic and porous properties. The following conclusions have been reached:

- In a sparsely dispersed porous layer, the Cattaneo heat flow equation has a significant effect on ferroconvection. For a Maxwell-Cattaneo ferromagnetic fluid, the Rayleigh-Bénard problem is always less stable than for a Fourier magnetic fluid.
- The flow is significantly influenced by magnetic and porous effects in the presence of a second sound.
- As the magnetic field strength and Cattaneo number increase, the threshold of the stationary instability drops. Thus, magnetic forces and second sound destabilize the system, causing convective motion to occur at shorter wavelengths.
- The inverse Darcy number and the Brinkman number are increased, which strengthens the ferromagnetic fluid's stability.
- The aspect ratio of the convection cell is particularly sensitive to the porous medium influence.
- The onset of convection is always advanced due to the presence of variable viscosity.

ORCID IDs

🇮🇳 Venkatesh Vidya Shree, <https://orcid.org/0000-0003-1554-8258>; 🇮🇳 Chandrappa Rudresha, <https://orcid.org/0000-0002-0958-4220>

🇮🇳 Chandrashekar Balaji, <https://orcid.org/0000-0002-3832-935X>

🇮🇳 Sokalingam Maruthamanikandan, <https://orcid.org/0000-0001-9811-0117>

REFERENCES

- [1] B.A. Finlayson, "Convective instability of ferromagnetic fluids", J. Fluid Mech. **40**(4), 753 (1970). <https://doi.org/10.1017/S0022112070000423>
- [2] K. Gotoh, and M. Yamada, "Thermal Convection in a Horizontal Layer of Magnetic Fluids", Journal of the Physical Society of Japan, **51**(9), 3042 (1982). <https://doi.org/10.1143/JPSJ.51.3042>
- [3] P.J. Stiles, and M. Kagan, "Thermoconvective instability of a horizontal layer of ferrofluid in a strong vertical magnetic field", Journal of Magnetism and Magnetic Materials, **85**, 196 (1990). [https://doi.org/10.1016/0304-8853\(90\)90050-Z](https://doi.org/10.1016/0304-8853(90)90050-Z)
- [4] S. Venkatasubramanian, and P.N. Kaloni, "Effects of rotation on the thermoconvective instability of a horizontal layer of ferrofluids", Int. J. Eng. Sci. **32**(2), 237 (1994). [https://doi.org/10.1016/0020-7225\(94\)90004-3](https://doi.org/10.1016/0020-7225(94)90004-3)
- [5] R. Sekar, G. Vaidyanathan, and A. Ramanathan, "Effect of rotation on ferrothermohaline convection", Journal of Magnetism and Magnetic Materials, **218**(2), 266 (2000). [https://doi.org/10.1016/S0304-8853\(00\)00358-9](https://doi.org/10.1016/S0304-8853(00)00358-9)
- [6] E.R. Lapwood, "Convection of a fluid in a porous medium", Math. Proc. Cambridge Philos. Soc. **44**(4), 508 (1948). <https://doi.org/10.1017/S030500410002452X>
- [7] R.A. Wooding, "Rayleigh instability of a thermal boundary layer in flow through a porous medium", J. Fluid Mech. **9**(2), 183 (1960). <https://doi.org/10.1017/S0022112060001031>
- [8] K. Kordylewski, "Convection effect on thermal ignition in porous medium", Chem. Eng. Sci. **39**(3), 610 (1983).
- [9] G. Vaidyanathan, A. Ramanathan, and S. Maruthamanikandan, "Effect of magnetic field dependent viscosity on ferroconvection in sparsely distributed porous medium", Indian Journal of Pure and Applied Physics, **40**, 166 (2001).
- [10] A. Ramanathan, and G. Suresh, "Effect of magnetic field dependent viscosity and anisotropy of porous medium on ferroconvection", Int. J. Eng. Sci. **42**(1-3), 411 (2004). [https://doi.org/10.1016/S0020-7225\(02\)00273-2](https://doi.org/10.1016/S0020-7225(02)00273-2)
- [11] N.M. Thomas, and S. Maruthamanikandan, "Effect of Gravity Modulation on the Onset of Ferroconvection in a Densely Packed Porous Layer", IOSR Journal of Applied Physics (IOSR-JAP), **3**(2278-4861), 30 (2013). [https://doi.org/10.1016/s0020-7225\(97\)80002-x](https://doi.org/10.1016/s0020-7225(97)80002-x)
- [12] G.N. Sekhar, P.G. Siddheshwar, G. Jayalatha, and R. Prakash, "Throughflow Effects on Thermal Convection in Variable Viscosity Ferromagnetic Liquids", International Journal of Mechanical and Mechatronics Engineering, **11**(6), (2017). <https://doi.org/10.5281/zenodo.1131971>
- [13] S. Mathew, and S. Maruthamanikandan, "Darcy-Brinkman Ferro convection with temperature dependent viscosity", J. Phys. Conf. Ser. **1139**(1), (2018). <https://doi.org/10.1088/1742-6596/1139/1/012023>.
- [14] V. Vidya Shree, C. Rudresha, C. Balaji, and S. Maruthamanikandan, "Effect of MFD viscosity on ferroconvection in a fluid saturated porous medium with variable gravity", Journal of Mines, Metals and Fuels (JMMF), **70**(3A), 98 (2022). <https://doi.org/10.18311/jmmf/2022/30675>
- [15] M.E. Gurtin, and A.C. Pipkin, "A general theory of heat conduction with finite wave speeds", Arch. Ration. Mech. Anal., **31**(2), 113 (1968). <https://doi.org/10.1007/BF00281373>
- [16] B. Straughan and F. Franchi, "Benard convection and the Cattaneo law of heat conduction", Proc. R. Soc. Edinburgh Sect. A Math. **96**(1-2), 175 (1984). <https://doi.org/10.1017/S0308210500020564>
- [17] P. C. Dauby, M. Nélis, and G. Lebon, "Generalized Fourier equations and thermoconvective instabilities", Revista Mexicana de Fisica, **48**(1), 57 (2002).
- [18] B. Straughan, "Oscillatory convection and the Cattaneo law of heat conduction", Ricerche Mat. **58**, 157 (2008). <https://doi.org/10.1007/s11587-009-0055-z>.
- [19] S. Mathew, S. Maruthamanikandan, S.S. Nagouda, "Gravitational Instability in a Ferromagnetic Fluid Saturated Porous Medium with Non-Classical Heat Conduction", IOSR J. Math. **6**(1), 7 (2013). <https://doi.org/10.9790/5728-0610718>
- [20] R. Keerthi, B. Mahanthes, and S.S. Nagouda, "Rayleigh-Bénard convection in a non-Newtonian dielectric fluid with Maxwell-Cattaneo law under the effect of internal heat generation/consumption", Multidiscip. Model. Mater. Struct. **16**(5), 1175 (2020). <https://doi.org/10.1108/MMMS-09-2019-0174>
- [21] S. Mathew, and S. Maruthamanikandan, "Oscillatory porous medium ferroconvection with Maxwell-Cattaneo law of heat conduction", J. Phys. Conf. Ser. **1850**(1), 2021. <https://doi.org/10.1088/1742-6596/1850/1/012024>

ВПЛИВ ЗАЛЕЖНОЇ ВІД МАГНІТНОГО ПОЛЯ В'ЯЗКОСТІ НА ФЕРОКОНВЕКЦІЮ ДАРСІ-БРІНКМАНА З ДРУГИМ ЗВУКОМ

Відья Шрі Венкатеш, Чандраппа Рудреша, Чандрасекар Баладжи, Солікангам Марутаманікандан

Факультет математики, Інженерна школа, Президентський університет, Бангалор 560064, Індія

Методом малого збурення досліджено задачу про конвекцію під дією плавучості в насиченому феромагнітній рідині пористому середовищі з законом Максвелла-Каттанео та МФД в'язкістю. Рух рідини описується за допомогою моделі Брінкмана. Передбачається, що рідка і тверда матриці знаходяться в локальній тепловій рівновазі. Для спрощених граничних умов проблема власних значень розв'язується точно й отримані розв'язки замкнутої форми для стаціонарної нестійкості. Було виявлено, що магнітні сили та другий звук підсилюють початок фероконвекції Брінкмана. Однак фероконвекція ускладнюється при збільшенні параметрів пористості. Результати показують, що в'язкість MFD гальмує початок фероконвекції Дарсі-Брінкмана і що ефект стабілізації в'язкості MFD зменшується, коли магнітне число Релея є значним. Крім того, показано, що коливальна нестійкість виникає перед стаціонарною нестійкістю, за припущення, що числа Прандтля і Каттанео є достатньо великими.

Ключові слова: ферорідина, в'язкість МФД, пористе середовище, магнітне поле, другий звук

EFFECT OF SILVER NANOPARTICLES SILAR CYCLE ON TiO₂ NANOPARTICLES THIN FILM: OPTICAL AND STRUCTURAL STUDY[†]

Daniel Thomas^a,  Eli Danladi^{b,*}, Mary T. Ekwu^c, Philibus M. Gyuk^a,
 Muhammed O. Abdulmalik^d, Innocent O. Echi^e

^aDepartment of Physics, Kaduna State University, Kaduna, Nigeria

^bDepartment of Physics, Federal University of Health Sciences, Otuopko, Benue State, Nigeria

^cDepartment of Physics, Airforce Institute of Technology, Kaduna, Nigeria

^dDepartment of Physics, Confluence University of Science and Technology, Osara, Kogi State, Nigeria

^eDepartment of Applied Physics, Kaduna Polytechnic, Kaduna, Nigeria

*Corresponding Author: danladielibako@gmail.com, tel.: +2348063307256

Received September 20, 2022; revised September 29, 2022; accepted October 7, 2022

Titanium dioxide (TiO₂) has gained a lot of research interests due to its applicability in electronic materials, energy, environment, health & medicine, catalysis etc as a result of its high permittivity, refractive index, efficiency, low-cost chemical inertness, eco-friendliness, photocatalytic activity, photostability and ability of decomposing a wide variety of organic compounds. In this study, the effect of silver nanoparticles (AgNPs) deposited through Successive Ionic Layer Adsorption and Reaction (SILAR) on the optical, structural and morphological properties of TiO₂ was explored systematically. The investigation was achieved via a combined effect of UV-vis spectroscopy, Scanning Electron Microscope (SEM) and X-ray Diffractometer (XRD) characterizing tools. As illustrated from the SEM micrographs, introduction of AgNPs result to enhanced nucleation and films growth with presence of shining surface which can be seen to contribute to good photon management through enhanced light scattering. The XRD results showed that, the presence of AgNPs on TiO₂ results to peaks corresponding to that of the TiO₂ crystallographic planes with no silver peaks detected due to its low concentration in the nanocomposite which shows that it was just homogeneously distributed on the surface of the TiO₂ nanoparticles. The UV-Vis results show a red shift to higher wavelength, showing an increase in visible light absorption which can be ascribed to the strong field effect of the Localized Surface Plasmon Resonance (LSPR). There was a decrease in band gap edge with introduction of AgNPs which indicated an increase in the optical conductivity of the AgNPs modified film.

Keywords: AgNPs, TiO₂, Nanocomposites, LSPR Effect, SILAR

PACS: 61.05.C-, 78.20.-e, 68.37.-d, 81.07.-b, 88.40.H-, 87.64.Ec

1. INTRODUCTION

The wide band gap energy of titanium dioxide prevents it from being active under ultraviolet (UV) light [1-3]. The solar spectrum is composed of 3–5 % UV light and around 40% visible (Vis) light [4]. As such, the photocatalytic properties of TiO₂ observed under sunlight irradiation is less active. There is need for modification of TiO₂ to improve its photocatalytic efficiency under sunlight visible irradiation. Several works have been done to improve TiO₂ so as to render it active in the visible light (400-800 nm) [5-7]. These include: (a) sensitization of TiO₂ with photosensitizers to absorb light in the visible region [8-12], (b) doping TiO₂ with metallic nanoparticles (MNPs) [13,14], and (c) doping TiO₂ with non-metals [15]. Presently, most researchers focus their attention on the MNPs approach by incorporating the metallic nanoparticles to the dense surface of TiO₂ to increase the photoactive wavelength range and enhance the photocatalytic activity under UV irradiation [5-7,13]. Among the doped metals (Ag, Au, Cu, Pt, Nb, Al, B, S, N, Zn, etc), noble metals have attracted significant attentions because of their enhanced properties through Surface Plasmon Resonance (SPR) effect [5,6]. These noble metals serve as scattering centers and sub-wavelength antennas in which the confined electromagnetic energy based on LSPR may greatly improve the absorption factor of the active medium surrounding the NPs [5,13].

Some current reports have shown that metal nanoparticles, such as Ag nanoparticles, augment the catalytic movement in the visible region of the electromagnetic spectrum [16,17]. The results disclosed that the existence of AgNPs is accountable for increasing the photocatalytic activity of TiO₂ in the visible region of sunlight [18].

There are some contradictory results that also reported showing the decreased activity of silver modified titania [12,19]. This may be due to their preparation method, nature of organic molecules, photoreaction medium, or the metal content and its dispersion. Even though there are many studies show the photocatalytic activity of silver doped titania [20-22], the exact mechanism and the role of silver is under debate. In this paper we reported a systematic study of photons initiated photocatalytic activity of screen-printed titania with silver nanoparticles. We discussed the effect on the optical and structural properties and the results show that the introduction of silver nanoparticle in the TiO₂ enhances the optical-response and contributes to the band gap narrowing and also enhances nucleation and grain growth.

[†] **Cite as:** D. Thomas, E. Danladi, M.T. Ekwu, P.M. Gyuk, M.O. Abdulmalik, and I.O. Echi, East Eur. J. Phys. 4, 118 (2022), <https://doi.org/10.26565/2312-4334-2022-4-11>

© D. Thomas, E. Danladi, M.T. Ekwu, P.M. Gyuk, M.O. Abdulmalik, I.O. Echi, 2022

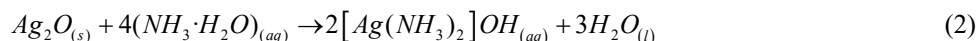
2. MATERIALS AND METHODS

2.1. Preparation of the Cationic Precursor

The AgNPs was prepared by dissolving 0.05 g of silver nitrate in 30 ml of deionized water. Ammonium hydroxide (NH₄OH) was added dropwise. When small amount of NH₄OH was added, Brownish precipitate appears which resulted in silver (I) oxide (Ag₂O_(s)) formation:



When excess NH₄OH was added to silver (I) oxide (Ag₂O_(s)), colorless solution of diammine silver complex ion was formed:

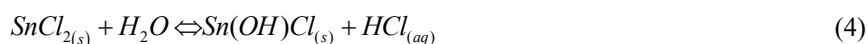


The equation that describes the ionic state of the complex system is given as:

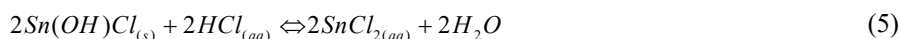


2.2 Preparation of the anionic precursor

0.1m (1.13g) Tin (II) chloride was added to 50 ml of distilled water resulting to insoluble $Sn(OH)Cl_{(s)}$:



2 ml of HCl was added in excess:



where



2.3 Deposition of TiO₂

The TiO₂ was used as received at its analytical grade level. The TiO₂ was deposited using screen printing technique where a 120 mesh device was used to directly screen print Ti-Nanoxide D/SP on four glass slides. They were dried at 150°C then annealed at 450°C.

2.4 Deposition of AgNPs using SILAR procedure

The glass slide with TiO₂ was immersed in $[Ag(NH_3)_2]^+$ solution for 2 minutes which describes the adsorption process, then rinsed with distilled water for 1 minute to remove excess adsorbed ions from the diffusion layer, and thereafter, it was then transferred to the tin chloride solution for 2 minutes which describes the reduction process. At this point the film turns brownish due to the reduction from Ag⁺ to Ag, it was then rinsed in distilled water for 1 minute to remove excess unreacted specie. This process is called one (1) SILAR cycle and is as shown in Figure 1 below. The process was repeated for two and three SILAR cycles.

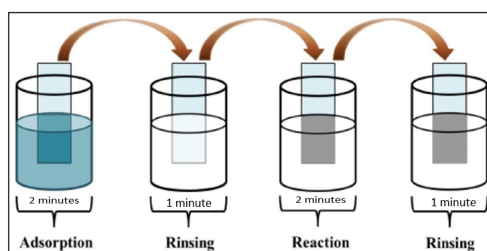


Figure 1. Demonstration of SILAR procedure

3.0 RESULTS AND DISCUSSION

3.1 Scanning Electron Microscopy (SEM)

Figure 2a-d show the micrographs of TiO₂ and TiO₂ with 1, 2 and 3 SILAR cycles of silver nanoparticles. The image of the TiO₂ film in Figure 2(a) demonstrates a dense and compact surface which shows a uniformly distributed nanoparticles with pores for infiltration of introduced materials. As shown from the images (Figure 2b-d), there are presence of shining surfaces which shows a distinct difference with the surface without AgNPs. The presence of the shining particles is an indication of the photocatalytic properties of the introduced AgNPs and also show that it can act as subwavelength antenna to channel incident photons for activation of semiconductor in the visible region for photon management.

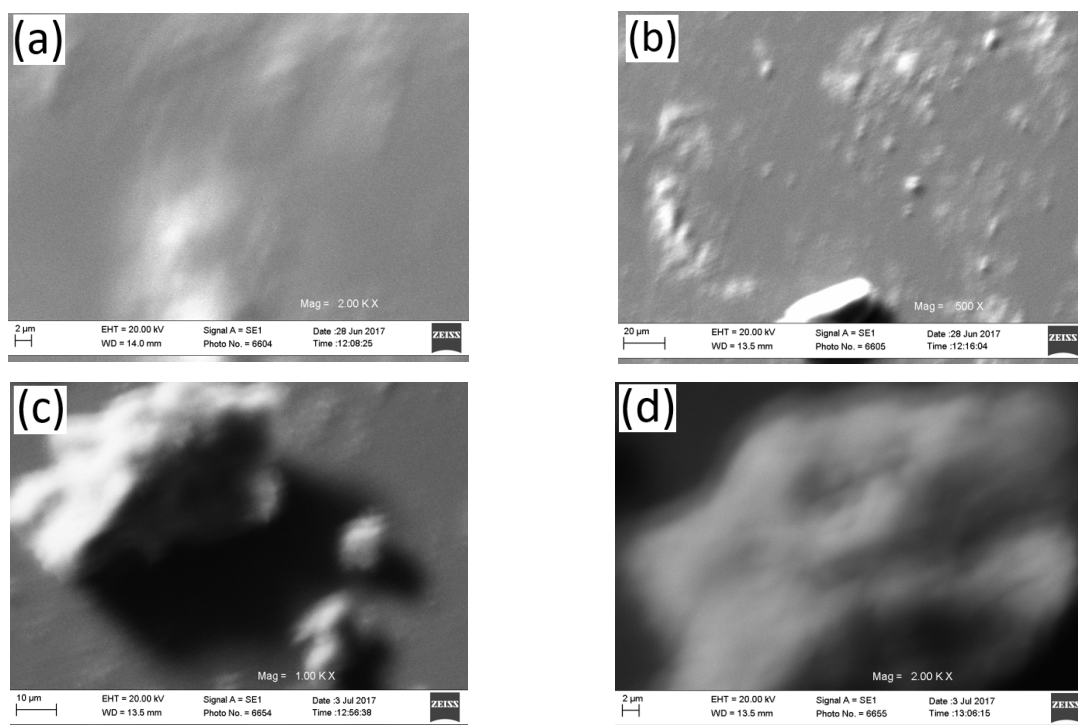


Figure 2. SEM images of: (a) bare TiO₂, (b) TiO₂/1cycle, (c) TiO₂/2cycle, and (d) TiO₂/3cycle at operating voltage of 10 Kv

This AgNPs can broaden the active area of TiO₂ through the introduction of localized surface plasmon resonance (LSPR) effect. When 1 SILAR cycle of AgNPs is introduced, a relatively symmetric distribution of shining particles were observed which can be speculated to contribute to good photon management through enhanced light scattering. The result demonstrates a sample size in the range of 25-55 nm as obtained from Isolution image analyzer with a smooth surface with no aggregated islands. Increasing the number of SILAR cycle from 2 to 3 cycles resulted to formation of significant islands with inhomogeneous distribution of nanoparticles leading to lesser transmittance of light.

3.2. X-ray Diffractometer (XRD)

The XRD pattern of TiO₂, TiO₂ with 1, 2 and 3 SILAR cycles are as shown in Figure 3a-d.

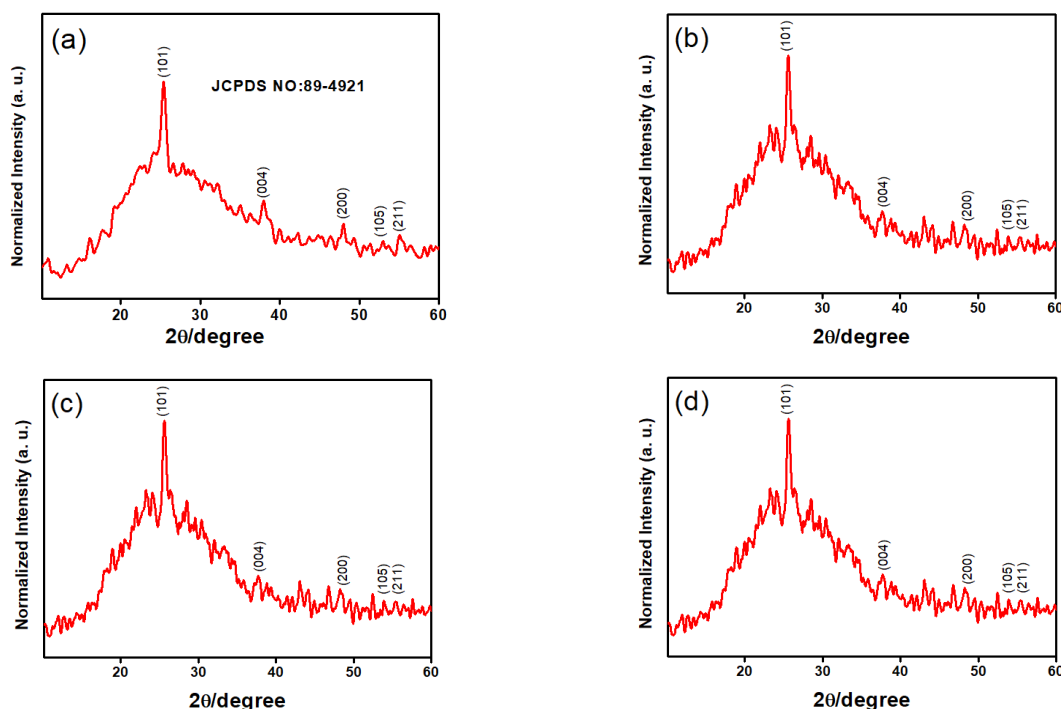


Figure 3. XRD Pattern of: (a) bare TiO₂, (b) TiO₂/1AgNP, (c) TiO₂/2AgNP, and (d) TiO₂/3AgNP

It shows clearly the major peaks at the 2 theta (2θ) angle of 25.36°, 37.87°, 47.97°, 54.93° and 55.45° which corresponds to the planes (101), (004), (200), (105) and (211) respectively. This agrees with the anatase phase of TiO₂ in accordance with JCPDS Card No. 89-4921 with unit cell parameters of 4.9619 Å for TiO₂. This result clearly shows that the TiO₂ nanoparticles were preferentially oriented with (101) face [23]. The anatase phase of TiO₂ is preferred over rutile and brookite for photocatalytic degradation of organic compounds [6,24]. The Fermi level of anatase is ~0.1 eV which is considered higher than that of the rutile phase and as such preferred as a photoelectrode material due to its generation of higher photovoltage over the rutile [25].

After depositing AgNPs on the TiO₂ nanoparticles surface, the observed peaks at the 2 theta angles correspond to that of the TiO₂ crystallographic planes. The peaks due to AgNPs was not detected due to its low concentration which shows that it was just homogeneously distributed on the surface of the TiO₂ nanoparticles [6]. Hence, the peaks are identical for TiO₂ and TiO₂ with 1, 2 and 3 SILAR cycles of AgNPs which shows that TiO₂ was effectively passivated with the AgNPs.

3.3. Optical study

The optical absorbance, transmittance, and reflectance bands of pure TiO₂ and TiO₂ with 1, 2 and 3 SILAR cycles of AgNPs are shown in Figure 4a-c. The measurement was taken at room temperature over the wavelength range of 200-1200 nm.

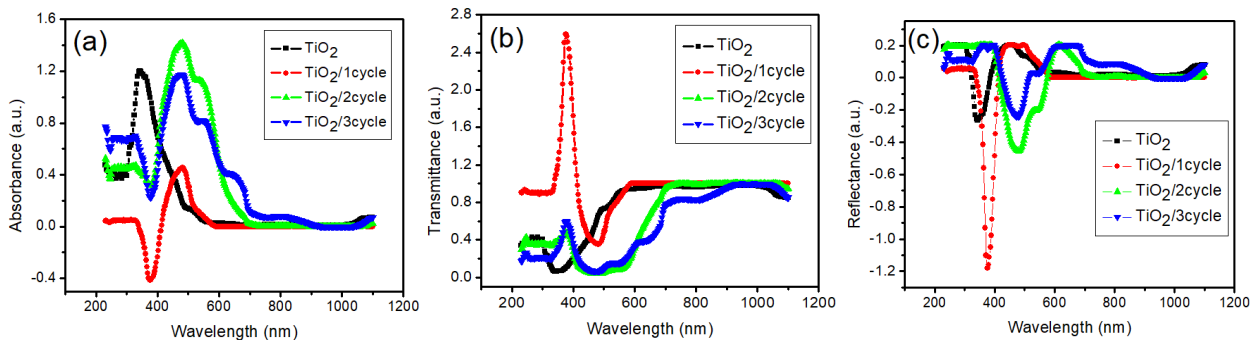


Figure 4 (a) absorbance, (b) transmittance and (c) reflectance against Wavelength

As shown in Figure 4a, the pure TiO₂ can be seen to be absorbing in the UV region with peak around 317 nm which can be attributed to its high refractive index. This property displayed suggests that, modification of the TiO₂ is desirable to make it activated in the visible region. Furthermore, Figure 4a also shows a red-shift towards higher wavelength after introducing AgNPs. This enhanced behavior can be seen to arise significantly through the introduction of LSPR from the deposited AgNPs.

Figure 4(b) presents typical transmittance spectra, which was obtained from the absorbance plot using equation (7).

$$T = 10^{-A} \quad (7)$$

where T is transmittance and A is absorbance.

There was a relatively constant transmittance in the visible to infrared region from 580 nm for TiO₂ and TiO₂ with 1 SILAR cycle of AgNPs. For the 2 SILAR cycle, the constant transmittance was observed from 650 nm. In TiO₂/3cycles nanocomposite, we observed variation in transmittance from the wavelength range of ~739 nm to ~1025 nm. It was observed generally, that transmittance intensity was inversely proportional to increase in the AgNPs SILAR cycle. For the reflectance properties, the reflectance was obtained from Equation (8).

$$R = 1 - (A + T) \quad (8)$$

As observed in the micrographs, there was presence of valleys and peaks in the profile with cycle increase. The red shift and the increase in optical path length is attributed to the non-uniform aggregation of the dispersed AgNPs forming the clusters [26] and the effect of interstitial dominance due to introduction of localized defect states during film formation [18].

The refractive index, Extinction coefficient and optical conductivity against photon energy ($h\nu$) is as shown in Figure 5a-c.

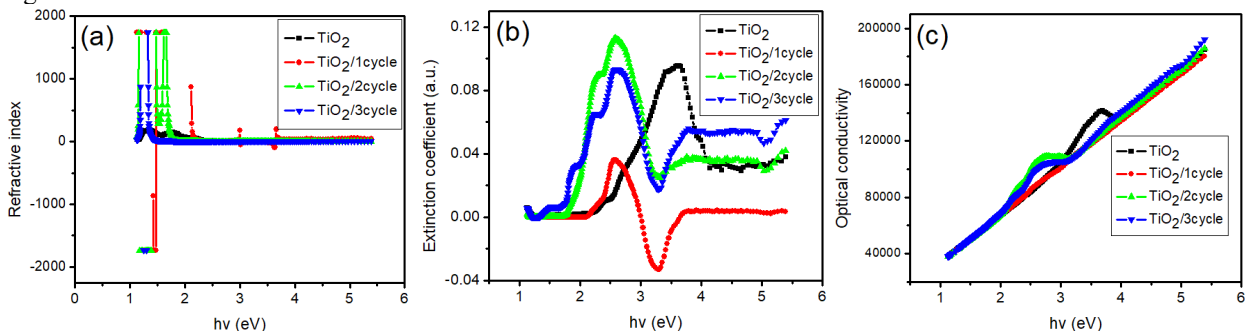


Figure 5. (a) optical refractive index, (b) extinction coefficient, and (c) optical conductivity against photon energy

The refractive index (n) shows the frequencies within a range in which films are not absorbing strongly [27]. The refractive index is crucial in characterizing photonic materials and it was estimated using equation (9), where R is the reflectance.

$$n = \frac{1 + \sqrt{R}}{1 - \sqrt{R}} \tag{9}$$

$$\alpha = \frac{A}{\lambda} \tag{10}$$

$$k = \frac{\alpha\lambda}{4\pi} \tag{11}$$

$$\sigma = \frac{\alpha nc}{4\pi} \tag{12}$$

The optical behavior of refractive index against photon energy of TiO_2 and TiO_2 with 1, 2 and 3 SILAR cycles of AgNPs is shown in Figure 5a. The results obtained show that the refractive index decreases with the increasing photon energy slightly before maintaining a constant value after 2.3 eV. The observation that the refractive index decreases with increasing photon energy is attributed to the dispersion of light at various interstitial layers present in the composite films.

Figure 5b shows the extinction coefficient versus photon energy as calculated from equation (11), where α is the coefficient of absorption obtained from equation (10) and λ is the wavelength.

The extinction coefficient is referred to the measure of the fractional light loss as a result of scattering and absorption per unit distance of the medium of penetration [27].

It is seen from Figure 5b that the extinction coefficient of all AgNPs modified TiO_2 increases with the increase in the photon energy up to 2.5 eV before it starts decreasing to form a valley at 3.4 eV. This decrease indicates that the fractional loss of light as a result of scattering and absorbance decreases between the range of 2.5 and 3.4 eV. It can also be noted from the figure that the value of extinction coefficient maintains a constant value from ~ 3.7 to 4.9 eV.

The Optical Conductivity was calculated from equation (12), where σ is the optical conductivity, α is the coefficient of absorption, n is the refractive index and c is the speed of light with magnitude of 3×10^8 m/s.

The variation of optical conductivity with the incident photon energy is shown in Figure 5c. The rise in optical conductivity when the energies of the photon is increasing can be attributed to high absorbance of the films in regions with higher photon energies and also due to increase in absorption coefficient. This can also be seen to arise from increased in density of localized states in the boundaries due to the rise in new defect states [28].

The energy bandgap has been evaluated from the absorption spectra.

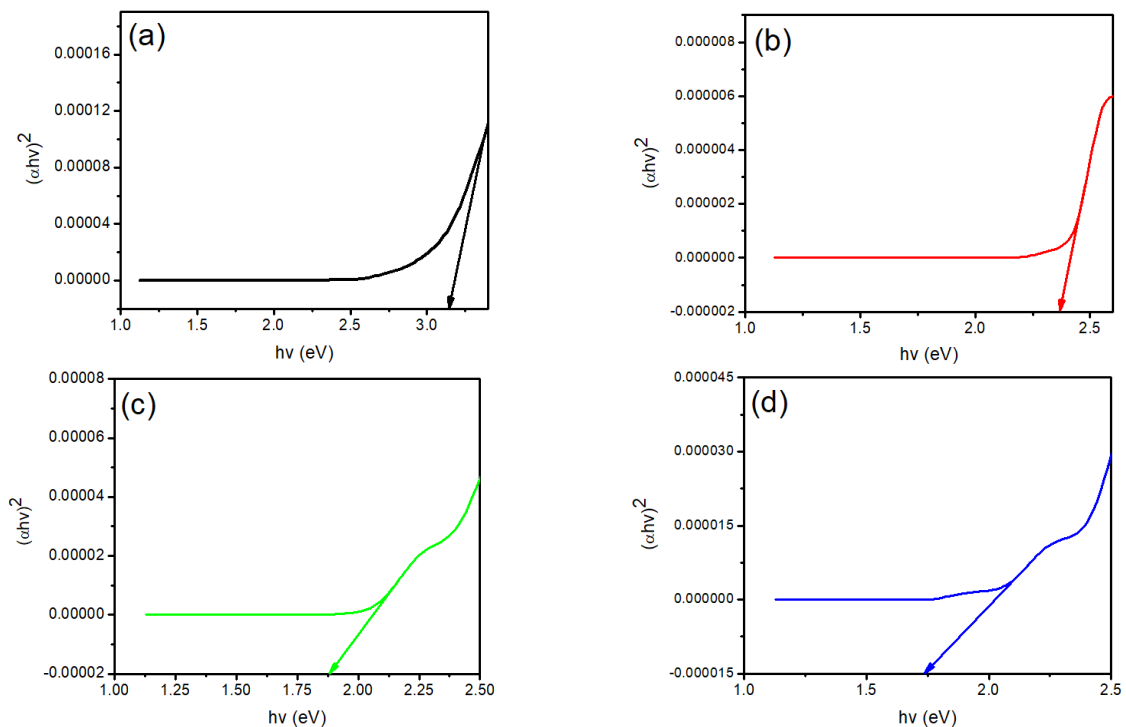


Figure 6. Plot of $(\alpha hv)^2$ against hv for (a) bare TiO_2 , (b) $\text{TiO}_2/1$ cycle, (c) $\text{TiO}_2/2$ cycle, and (d) $\text{TiO}_2/3$ cycle

The photocatalytic ability of TiO₂ photocatalyst under visible light is determined by lower bandgap energy (E_g) or absorption in visible light. The energy bandgap (E_g) was determined based on the wavelength of maximum absorption (λ) according to equation (13).

$$E_g = \frac{1240}{\lambda}, \quad (13)$$

here, the maximum absorption wavelength is obtained from the absorption wavelength data.

The E_g was obtained in the formula describes as Tauc plot [29]. The E_g can be obtained from extrapolation of the linear part, $(\alpha hv)^2$ versus hv or $(\alpha hv)^{1/2}$ versus hv plot to $hv = 0$.

Figure 6a-d show the optical band gap of TiO₂ and TiO₂ loaded with 1, 2 and 3 SILAR cycle of AgNPs. As shown from the results, increase in number of SILAR cycles of AgNPs leads to decrease in band gap of the film. A reduction in the band gap demonstrates an increase in the optical conductivity of the material, this is because the electrons will require less energy to cross the fermi energy level of the material [7]. this shows that, a reduction in the band gap energy of the modified samples will yield a better electron transport capability to the conduction band of the pure TiO₂. The band gap of TiO₂, TiO₂/Ag, TiO₂/2Ag, and TiO₂/3Ag nanocomposites are: 3.23 eV, 2.27 eV, 1.88 eV and 1.74 eV.

4. CONCLUSION

The optical, structural and morphological properties of TiO₂ and TiO₂ with 1, 2, and 3 SILAR cycles were investigated using the combined effect of UV-vis spectroscopy, Scanning Electron Microscope and X-ray Diffractometer. The results obtained show that TiO₂ was significantly enhanced to absorb photons at higher wavelength with silver nanoparticles inclusion which is attributed to localized surface plasmon resonance phenomenon from AgNPs. The band gap of TiO₂ was dramatically reduced from 3.23 to 1.74 eV when AgNPs was introduced. The morphological structures of the prepared samples show improved film with uniform distribution of nanoparticles. The structural analyses of the fabricated films show prominent diffraction peaks at 25.36°, 37.87°, 47.97°, 54.93° and 55.45° which corresponds to the planes (101), (004), (200), (105) and (211) respectively. This agrees with the anatase phase of TiO₂ with unit cell parameters of 4.9619 Å for TiO₂. These results clearly show that silver nanoparticles can enhance optical and structural properties of TiO₂.

Acknowledgement

The authors are grateful to Physics Advanced Laboratory, Sheda Science Technology Complex (SHESTCO) and Namiroch research Laboratory, Abuja for the use of their equipment.

Conflict of interest. Authors have declared that there was no conflict of interest.

Funding. This article did not receive any funding support.

ORCID IDs

©Eli Danladi, <https://orcid.org/0000-0001-5109-4690>; ©Muhammed O. Abdulmalik, <https://orcid.org/0000-0002-3250-7864>

REFERENCES

- [1] M. Pelaez, N.T. Nolan, S.C. Pillai, M.K. Seery, P. Falaras, A.G. Konto, P.S.M. Dunlop, J.W. Hamilton, J.A. Byrne, K. O'shea, M.H. Entezari, and D.D. Dionysiou, *Applied Catalysis B: Environmental*, **125**, 331 (2012). <https://doi.org/10.1016/j.apcatb.2012.05.036>
- [2] M.K. Seery, R. George, P. Floris, and S.C. Pillai, *Journal of Photochemistry and Photobiology: A Chemistry*, **189**, 258 (2007). <https://doi.org/10.1016/j.jphotochem.2007.02.010>
- [3] S. Sontakke, C. Mohan, J. Modak, and G. Madras, *Chemical Engineering Journal*, **189-190**, 101 (2012). <https://doi.org/10.1016/j.cej.2012.02.036>
- [4] M.Y. Onimisi, E. Danladi, T. Jamila, S. Garba, G.J. Ibeh, O.O. Ige, and E. Lucky, *Journal of the Nigerian Association of Mathematical Physics*, **10**, 177 (2019). <http://e.nampjournals.org/product-info.php?pid4037.html>
- [5] J. Tasiu, E. Danladi, M. T. Ekwu, and L. Endas, *Journal of nano and materials science research*, **1**, 16 (2022). <http://journals.nanotechunn.com/index.php/jnmsr/article/view/1/10>
- [6] E. Danladi, M. Y. Onimisi, S. Garba, and J. Tasiu, *SN Applied Sciences*, **2**, 1769 (2020). <https://doi.org/10.1007/s42452-020-03597-y>
- [7] G.A. Alamu, O. Adedokun, I.T. Bello, and Y.K. Sanusi, *Chemical Physics Impact*, **3**, 100037 (2021). <https://doi.org/10.1016/j.chphi.2021.100037>
- [8] H.M. Chenari, C. Seibelb, D. Hauschild, and H. Abdollahiand, *Materials Research*, **19**(6), 1319 (2016). <https://doi.org/10.1590/1980-5373-MR-2016-0288>
- [9] K. Nakata, and A. Fujishima, *Journal of Photochemistry and Photobiology C: Photochemistry Reviews*, **13**, 169 (2012). <https://doi.org/10.1016/j.jphotochemrev.2012.06.001>
- [10] M.R. Hoffmann, S.T. Martin, W. Choi, and W.D. Bahnemann, *Chemical Reviews*, **95**, 69 (1995). <https://doi.org/10.1021/cr00033a004>
- [11] G. Govindasamy, P. Murugasen, and S. Sagadevan, *Materials Research*, **19**(2), 413 (2016). <https://doi.org/10.1590/1980-5373-MR-2015-0411>

- [12] T. Daniel, P. M. Gyuk, S. Alhassan, E. Danladi, N. J. Gyuk, P. Anthony, Journal of the Nigerian Association of Mathematical Physics, **54**, 179 (2020). <http://e.nampjournals.org/product-info.php?pid4068.html>
- [13] S. Sreeja, and B. Pesala, Scientific Reports, **10**, 8240 (2020). <https://doi.org/10.1038/s41598-020-65236-1>
- [14] M. Jacob, H. Levanon, and P.V. Kamat, Nano letters, **3**, 353 (2003). <https://doi.org/10.1021/nl0340071>
- [15] J.C. Colmenares, M.A. Aramedia, A. Marinas, J.M. Marinas, and F.J. Ubano, Applied Catalysis A: General, **306**, 120 (2006). <https://doi.org/10.1016/j.apcata.2006.03.046>
- [16] F.L. Yap, P. Thoniyot, S. Krishnan, and S. Krishnamoorthy, ACS Nano, **6**(3), 2056 (2012). <https://doi.org/10.1021/nn203661n>
- [17] G. Kovacs, Z. Pap, C. Cotet, V. Cosoveanu, L. Baia, and V. Danciu, Materials, **8**, 1059 (2015). <https://doi.org/10.3390/ma8031059>
- [18] W.J. Cho, Y. Kim, and J.K. Kim, ACS Nano **6**, 249 (2012). <https://doi.org/10.1021/nn2035236>
- [19] V. Vamathevan, R. Amal, D. Beydoun, G. Low, and S. McEvoy, Journal of Photochemistry and Photobiology A: **148**, 303 (2002). <https://doi.org/10.1016/j.cj.2003.05.004>
- [20] M. Sökmen, D.W. Allen, F. Akkaş, N. Kartal, and F. Acar, Water, Air, and Soil Pollution, **132**, 153 (2001). <https://doi.org/10.1023/A:1012069009633>
- [21] H.M. Sung-Suh, J.R. Choi, H.J. Hah, S.M. Koo, and Y.C. Bae, Journal of Photochemistry and Photobiology A, **163**, 37-44 (2004). [https://doi.org/10.1016/S1010-6030\(03\)00428-3](https://doi.org/10.1016/S1010-6030(03)00428-3)
- [22] L. Zhang, J.C. Yu, H.Y. Yip, Q. Li, K.W. Kwong, A. Xu, and P.K. Wong, Langmuir, **19**, 10372 (2003). <https://doi.org/10.1021/la035330m>
- [23] S. Kalaiarasi, and M. Jose, Applied Physics A, **123**, 512 (2017). <https://doi.org/10.1007/s00339-017-1121-0>
- [24] M. Sahu, B. Wu, L. Zhu, C. Jacobson, W.N. Wang, N. Jones, Y. Goyal, Y.J. Tang, and P. Biswas, Nanotechnology, **22**, 415704 (2012). <https://doi.org/10.1088/0957-4484/22/41/415704>
- [25] K.M. Mansoob, A. Sajid, M. Ansari, A. Ikhlasul, L. Jintae, and H.C. Moo, Nanoscale, **5**, 4427 (2013). <https://doi.org/10.1039/C3NR00613A>
- [26] C. Chambers, S.B. Stewart, B. Su, H.F. Jenkinson, J.R. Sandy, and A.J. Ireland, Dental Materials, **33**, e115–e123 (2017). <https://doi.org/10.1016/j.dental.2016.11.008>
- [27] I.L. Ikhioya, E. Danladi, O.D. Nnanyere, and A.O. Salawu, Journal of the Nigerian Society of Physical Sciences, **4**(1), 123 (2022). <https://doi.org/10.46481/jnsps.2022.502>
- [28] N.F. Mott, and E.A. Davis, *Electronic processes in non-crystalline materials*, 2nd edition, (Clarendon, Oxford, 1979).
- [29] J. Tauc, editor, *Amorphous and Liquid Semiconductors*, vol.159, (Plenum Press, NewYork, 1974).

ВПЛИВ СИЛІРНОГО ЦИКЛУ НАНОЧАСТИНОК СРІБЛА НА ТОНКУ ПЛІВКУ НАНОЧАСТИНОК TiO₂: ОПТИЧНЕ ТА СТРУКТУРНЕ ДОСЛІДЖЕННЯ

Деніел Томас^a, Елі Данладі^b, Мері Т. Екву^c, Філібус М. Гюк^d, Мухаммед О. Абдулмалік^d, Інокентій О. Ечі^e

^aФізичний факультет Державного університету Кадуна, Кадуна, Нігерія

^bФізичний факультет Федерального університету наук про здоров'я, Отукпо, штат Бенуе, Нігерія

^cФізичний факультет, Технологічний інститут ВПС, Кадуна, Нігерія

^dФізичний факультет, Об'єднаний університет науки і технологій, Осара, штат Когі, Нігерія

^eФакультет прикладної фізики, Кадуна Політехніка, Кадуна, Нігерія

Діоксид титану (TiO₂) викликав значний дослідницький інтерес через його застосування в електронних матеріалах, енергетиці, навколишньому середовищі, здоров'ї та медицині, каталізі, що є результатом його високої діелектричної проникності, показника заломлення, ефективності, низької вартості хімічної інертності, екологічності, фотокаталітичної активності, фотостабільності і здатності розкласти широкий спектр органічних сполук. У цьому дослідженні було систематично досліджено вплив наночастинок срібла (AgNP), нанесених шляхом послідовної адсорбції та реакції (SILAR), на оптичні, структурні та морфологічні властивості TiO₂. Дослідження було досягнуто за допомогою комбінованого ефекту ультрафіолетової спектроскопії, скануючої електронної мікроскопії (SEM) і рентгенівської дифракції (XRD). Як видно з мікрофотографій SEM, введення AgNPs призводить до посиленого зародження та росту плівок із наявністю блискучої поверхні, яка, як можна побачити, сприяє хорошему управлінню фотонами через посилене розсіювання світла. Результати XRD показали, що наявність AgNPs на TiO₂ призводить до піків, що відповідають пікам кристалографічних площин TiO₂, без піків срібла через низьку концентрацію срібла в нанокompозиті, що показує, що він просто рівномірно розподілений на поверхні наночастинок TiO₂. Результати UV-Vis показують червоний зсув у бік вищої довжини хвилі, показуючи збільшення поглинання видимого світла, яке можна віднести до сильного ефекту ближнього поля та ефекту дальнього поля локалізованого поверхневого плазмонного резонансу (LSPR). Спостерігалось зменшення краю забороненої зони із введенням AgNP, що вказує на збільшення оптичної провідності плівки, модифікованої AgNP.

Ключові слова: AgNPs, TiO₂, нанокompозити, LSPR ефект, SILAR

NUMERICAL STUDY OF 25.459% ALLOYED INORGANIC LEAD-FREE PEROVSKITE CsSnGeI₃-BASED SOLAR CELL BY DEVICE SIMULATION[†]

✉ **Muhammed O. Abdulmalik^a, Eli Danladi^{b,*}, Rita C. Obasi^c, Philibus M. Gyuk^d, Francis U. Salifu^a, Suleiman Magaji^e, Anselem C. Egbugha^f, Daniel Thomas^d**

^aDepartment of Physics, Confluence University of Science and Technology, Osara, Kogi State, Nigeria

^bDepartment of Physics, Federal University of Health Sciences, Otukpo, Benue State, Nigeria

^cCentre for Satellite Technology Development-NASRDA, Abuja, Nigeria

^dDepartment of Physics, Kaduna State University, Kaduna, Nigeria

^eDepartment of Electronics and Communications Engineering, Nigerian Defence Academy, Kaduna, Nigeria

^fOperations Unit, Starsight Energy, Nigeria

*Corresponding Author: danladielibako@gmail.com, tel.: +2348063307256

Received October 16, 2022; revised November 10, 2022; accepted November 12, 2022

The toxic lead component as well as the expensive and less stable spiro-OMeTAD in perovskite solar cells (PSCs) pose a great deal of hindrance to their commercial viability. Herein, a computational approach towards modeling and simulation of all inorganic cesium tin-germanium triiodide (CsSnGeI₃) based perovskite solar cell was proposed and implemented using solar cell capacitance simulator (SCAPS-1D) tool. Aluminium doped zinc oxide (ZnO:Al) and Copper Iodide (CuI) were used as electron and hole transport layers (ETL and HTL) respectively. The initial device without any optimization gave a power conversion efficiency (PCE) of 24.826%, fill factor (FF) of 86.336%, short circuit current density (J_{sc}) of 26.174 mA/cm² and open circuit voltage (V_{oc}) of 1.099 V. On varying the aforementioned parameters individually while keeping others constant, the optimal values are 1000 nm for absorber thickness, 10¹⁴ cm⁻³ for absorber layer defect density, 50 nm for ETL thickness, 10¹⁷ cm⁻³ for ETL doping concentration and 260 K for temperature. Simulating with these optimized values results to PCE of 25.459%, V_{oc} of 1.145 V, J_{sc} of 25.241 mA/cm², and a FF of 88.060%. These results indicate that the CsSnGeI₃ is a viable alternative absorbing layer for usage in the design of a high PCE perovskite solar cell device.

Keywords: Perovskite solar cells, SCAPS-1D, CsSnGeI₃, hole transport material, electron transport material

PACS: 41.20.Cv; 61.43.Bn; 68.55.ag; 68.55.jd; 73.25.+i; 72.80.Tm; 74.62.Dh; 78.20.Bh

1. INTRODUCTION

Metal halide perovskite solar cells (PSCs) belong to one of the most promising photovoltaic technologies for next-generation solar cells. The PSC works based on the following principles: (i) excitons generation when photon energy is absorbed, (ii) excited electrons being drifted into the conduction band (CB) of the electron transport layer (ETL), (iii) holes transferred into the hole transport layer (HTL), and (iv) holes injection into the back-metal electrode [1].

The high power conversion efficiency exceeding 25% from its original value of 3.8% and simple fabrication process of PSCs have triggered the interest of researchers in the photovoltaic community [2–5]. The remarkable performance of PSCs are attributed to high absorption coefficients, a balanced excitons transport, high charge carrier mobilities, long carrier diffusion lengths, and direct and tunable band gaps [6, 7]. However, the presence of toxic lead in perovskite absorber is considered as one of the significant impediments towards its commercial exploitation. In an attempt to replace lead with other less or non-poisonous materials, researchers have considered other divalent metal cations such as tin (Sn²⁺) and germanium (Ge²⁺), which have an oxidation state of +2 with an outer layer properties similar to that of Pb²⁺ [8, 9].

The radius of Sn²⁺ (1.35 Å) which is smaller than that of Pb²⁺ (1.49 Å), has resulted to non-distortion of the perovskite nano crystal structure when it is replaced as a divalent cation in lead-based perovskite absorber [10]. Furthermore, due to its narrow band gap of 1.3 eV, it allows high theoretical PCE value to be obtained [11]. A study by Sabba et al. [12] using CsSnI₃, CsSnI₂Br, CsSnIBr₂ and CsSnBr₃ as absorbing materials, an interesting band gap of 1.27 eV with outstanding optoelectronic properties for CsSnI₃ was obtained. High PCEs were obtained with the lead-free inorganic absorbing material [13, 14]. But Sn²⁺ oxidizes to Sn⁴⁺ very easily. Therefore, the Sn-based PSCs are susceptible to degradation under ambient environment and hence their efficiencies are affected. The formation energy of Sn vacancies is very low. The formation energy and the change in oxidation state from Sn²⁺ to Sn⁴⁺ leads to self-doping and also brings about a p-type metallic behaviour [15]. Another candidate for the replacement of Pb²⁺ as a divalent metal cation is Ge²⁺ which has a smaller ionic radius (0.73 Å) than that of Sn²⁺ and Pb²⁺. Higher conductivity is shown by Ge-based perovskites as compared to the Pb-based perovskites and Sn-based perovskites. Better conductivity and other optoelectronic properties are expected when Ge-Sn alloy is used as replacement of Pb. Chen et al [16] reported a perovskite absorbing material, CsSnGeI₃ by alloying CsSnI₃ with Ge (II). The device demonstrated excellent stability in air and it outperformed the CsSnI₃ and CsGeI₃ pristine counterparts, with a PCE of 7%.

The instability caused by organic compounds in PSC has been a major concern for researchers [17, 18]. The vastly used state-of-art hole transport material (HTM), Spiro-OMeTAD demonstrates hygroscopic nature, tendency to crystallize,

[†] **Cite as:** M.O. Abdulmalik, E. Danladi, R.C. Obasi, P.M. Gyuk, F.U. Salifu, S. Magaji, A.C. Egbugha, and D. Thomas, East Eur. J. Phys. 4, 125 (2022), <https://doi.org/10.26565/2312-4334-2022-4-12>

© M.O. Abdulmalik, E. Danladi, R.C. Obasi, P.M. Gyuk, F.U. Salifu, S. Magaji, A.C. Egbugha, D. Thomas, 2022

and vulnerability to both moisture and heat, as such must be replaced with a cost-effective and stable HTM having high hole mobility with ease of synthesis [19, 20].

The ETL influences the PCE of PSCs by blocking holes, thereby minimizing the charge carrier recombination from the perovskite active layer and hence, providing the photogenerated electrons a pathway to the electrode [21]. A high performing ETL have attributes of high electrical conductivity and high electron mobility which should be comparable to those of the perovskite layer. The most commonly used ETLs are metal oxides such as TiO_2 , ZnO and SnO_2 , their electrical properties can be tailored by doping [22]. The impact of Aluminium (Al) on zinc oxide (ZnO) as ETL in PSCs was studied by Alias et al [23]. In their study, only the properties of the ETL and interface were explored and a PCE, up to 17.59% was obtained for 1 mol% Al concentration in ZnO . Several properties of PSCs can be studied to give better performance as such necessitated this research.

In the present work, an inorganic, CsSnGeI_3 -based PSC was studied by utilizing inorganic HTM (CuI) and inorganic electron transport materials (ZnO:Al). By optimizing various properties like thickness of the perovskite absorbing layer, its defect density, the thickness of the electron transport layer, the doping concentration of the electron transport layer, the back-metal contact and temperature, a PCE of 25.459%, with an open circuit voltage of 1.145 V, a short circuit current density of 25.241 mA/cm^2 , and a fill factor of 88.060% were obtained. The present work may be helpful in designing and implementing eco-friendly lead free Sn-Ge-alloyed-based PSCs in the future.

2. THEORETICAL METHODS AND DEVICE STRUCTURE

Device simulation is a powerful tool that gives an insight for understanding the electrical and optical properties of solar cells and ultimately providing useful information for design of photovoltaic devices experimentally. In this study, we used the SCAPS-1D software version 3.3.10 to carry out our simulation. This software is designed to simulate multilayer (up to seven layers) solar cells, in which holes and electrons transport are considered by solving the basic semiconductor equations: the Poisson equation and the continuity equation of both charge carriers (holes and electrons) under steady-state condition.

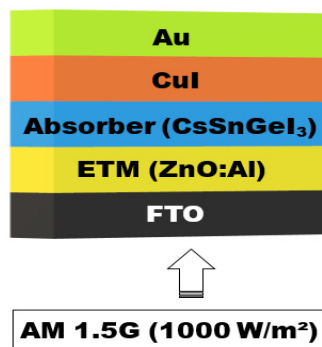


Figure 1. Device structure

This simulation was carried out in the n-i-p configuration of $\text{FTO}/\text{ZnO:Al}/\text{CsSnGeI}_3/\text{CuI}/\text{Au}$, which is represented in Figure 1. Starting from illumination point, fluorine-doped tin oxide (FTO) is used as a front contact, ETL as ZnO:Al , the absorber layer as CsSnGeI_3 , HTL as CuI, and gold (Au) as the back metal-electrode. The work function of the front and counter electrode are 4.4 eV and 5.1 eV, respectively. The simulation was done with A.M. 1.5 spectrum ($1000 \text{ W}/\text{m}^2$) light source, the temperature of the simulation was set at 300 K, the frequency at 1×10^{16} Hz, and a scanning voltage of 0-1.50 V. The details for each layer is as summarized in Table 1. The properties of the defect interface $\text{ZnO:Al}/\text{CsSnGeI}_3$ and $\text{CsSnGeI}_3/\text{CuI}$ are shown in Table 2.

Table 1. Parameters used for simulation of perovskite solar cell structures using SCAPS-1D [19, 23-26]

Parameters	FTO	ZnO:Al	CsSnGeI ₃	CuI
Thickness (μm)	0.4	0.22	1.50	0.10
Band gap energy E_g (eV)	3.5	3.25	1.50	2.98
Electron affinity χ (eV)	4.3	4.0	3.9	2.10
Relative permittivity ϵ_r	9	9	28	6.5
Effective conduction band density N_c (cm^{-3})	2.2×10^{18}	2.0×10^{18}	3.1×10^{18}	2.8×10^{19}
Effective valance band density N_v (cm^{-3})	1.8×10^{19}	1.8×10^{19}	3.1×10^{18}	1.0×10^{19}
Electron thermal velocity (cm/s)	1.0×10^7	1.0×10^7	1.0×10^7	1.0×10^7
Hole thermal velocity (cm/s)	1.0×10^7	1.0×10^7	1.0×10^7	1.0×10^7
Electron mobility μ_n ($\text{cm}^2 \text{ V}^{-1} \text{ s}^{-1}$)	2.0×10^1	3.0×10^2	9.74×10^2	1.69×10^{-4}
Hole mobility μ_p ($\text{cm}^2 \text{ V}^{-1} \text{ s}^{-1}$)	1.0×10^1	2.5×10^1	2.13×10^2	1.69×10^{-4}
Donor concentration N_D (cm^{-3})	1.0×10^{18}	7.25×10^{18}	0	0
Acceptor concentration N_A (cm^{-3})	0	0	1×10^{19}	1×10^{18}
Defect density N_t (cm^{-3})	1×10^{15}	1×10^{14}	1×10^{11}	1×10^{12}

Table 2. Defect parameter values of the interfaces of the device

Parameters	ZnO:Al/CsSnGeI ₃ interface	CsSnGeI ₃ /CuI interface
Defect type	Neutral	Neutral
Capture cross section for electrons (cm ²)	1×10 ⁻¹⁵	1×10 ⁻¹⁸
Capture cross section for holes (cm ²)	1×10 ⁻¹⁵	1×10 ⁻¹⁶
Energetic distribution	Single	Single
Energy level with respect to E _v (eV)	0.600	0.600
Characteristic energy (eV)	0.1	0.1
Total density (cm ⁻³)	1×10 ¹¹	1×10 ¹²

3. RESULTS AND DISCUSSION

3.1. Performance study of the initial device, quantum efficiency and energy band profile

The current-voltage (*J-V*) characteristics of the initial perovskite solar cell device simulated under illumination is shown in Figure 2(a).

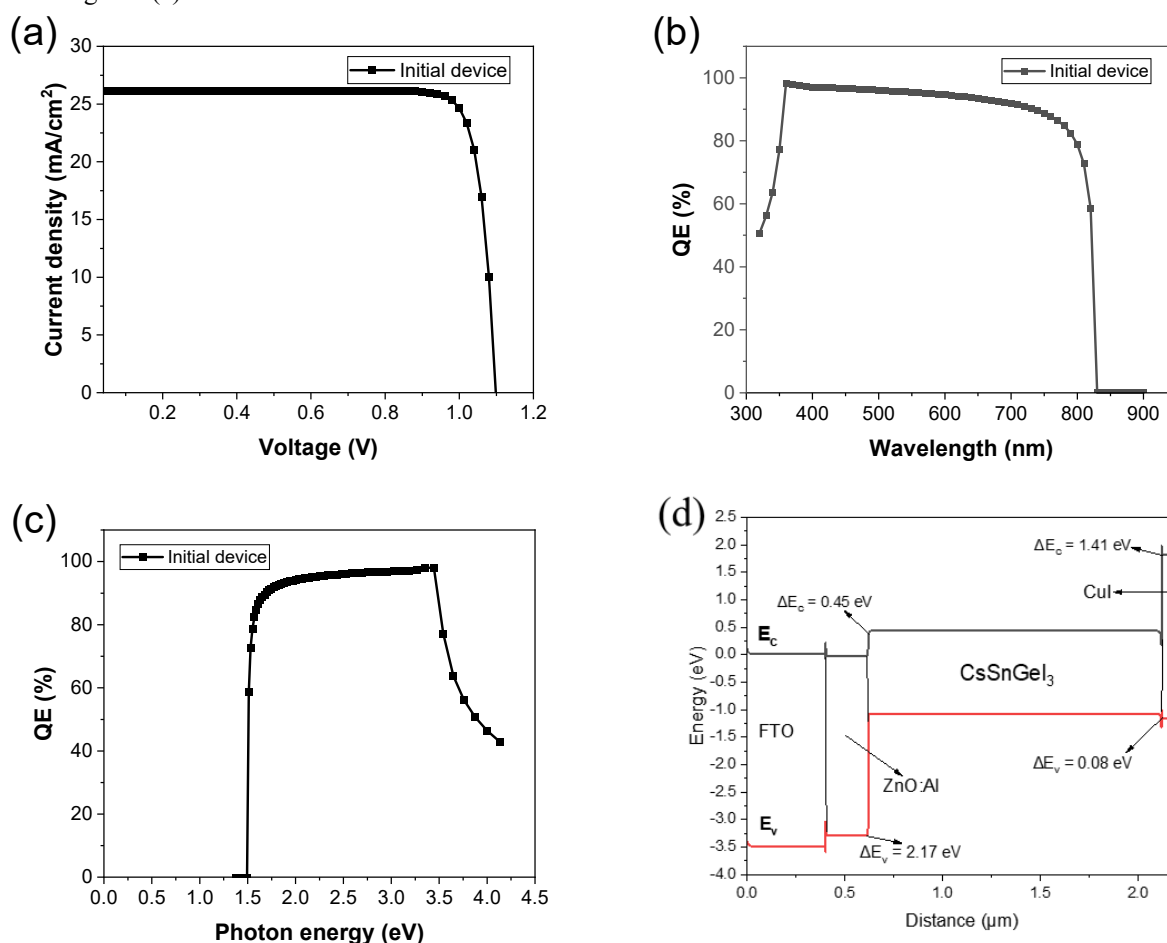


Figure 2. (a) *J-V* curve of PSC with initial solar cell characteristics, (b) quantum efficiency against wavelength, (c) quantum efficiency against photon energy and (d) energy profile band diagram

Under illumination, a V_{oc} of 1.099 V, J_{sc} of 26.174 mA/cm², FF of 86.336%, and PCE of 24.826% were obtained. Comparing these solar cell characteristics with simulated work on CsSnGeI₃ perovskite obtained by a group of researchers [26], comparable V_{oc} (1.00 V) and J_{sc} (25.75 mA/cm²) were obtained. In our simulation, we obtained appreciable values of FF, PCE which are higher than those from their simulated research work. This could be attributed to the increase in conductivity of the ETL due to doping and different HTL used. Figure 2b & c shows the quantum efficiency against wavelength and photon energy. It is within the range of 300 to 900 nm, which has maximum attained value of 98% observed at 360 nm. It sweeps across the visible region which satisfies the device's requirement. The strong absorption at the visible region of the QE curve is a factor that determines the light absorption strength at the various wavelengths of light and the cut-off region at 850 nm which certified the band gap of 1.5 eV for CsSnGeI₃ [25]. Figure 2d shows the energy band diagram of ETL/perovskite/HTL materials in the device structure, with the interface conduction and valence band offset at the ZnO:Al/CsSnGeI₃ interface of 0.45 eV and 2.17 eV while at the CsSnGeI₃/CuI interface,

the interface conduction and valence band offset are 1.41 eV and 0.08 eV respectively. These values are beneficial for flow of charge carriers within the interface and subsequently result to enhanced device performance.

3.2. Effect of the absorbing layer thickness

The absorbing layer thickness is one of the important parameters having a significant impact on the device's performance. A good choice of this thickness is very essential to determine better device's performance. In order to study its impact on the perovskite solar cell, the CsSnGeI₃ layer thickness was varied in the range of 100–1000 nm while keeping all other parameters untouched as detailed in Tables 1 and 2. The *J-V* curve and the quantum efficiency of the performance with varied device is shown in Figure 3a & b. The effect of the variation of the absorbing layer thickness on the device parameters; V_{oc} , J_{sc} , FF and PCE are shown in Figures 3c & d.

The V_{oc} and J_{sc} rise sharply with corresponding increase in thickness of absorbing layer up to a thickness of 500 nm, and rises steadily from 600 to 1000 nm as shown in Figure 3(d). PCE of the device is low when thickness of the absorbing layer is too small as shown in Figure 3(c), which is evident to poor absorption of light by the material. As the thickness of the absorbing layer increases, the number of photo-generated charge carriers increases leading to greater PCE of device, due to more photons being absorbed by the material [27].

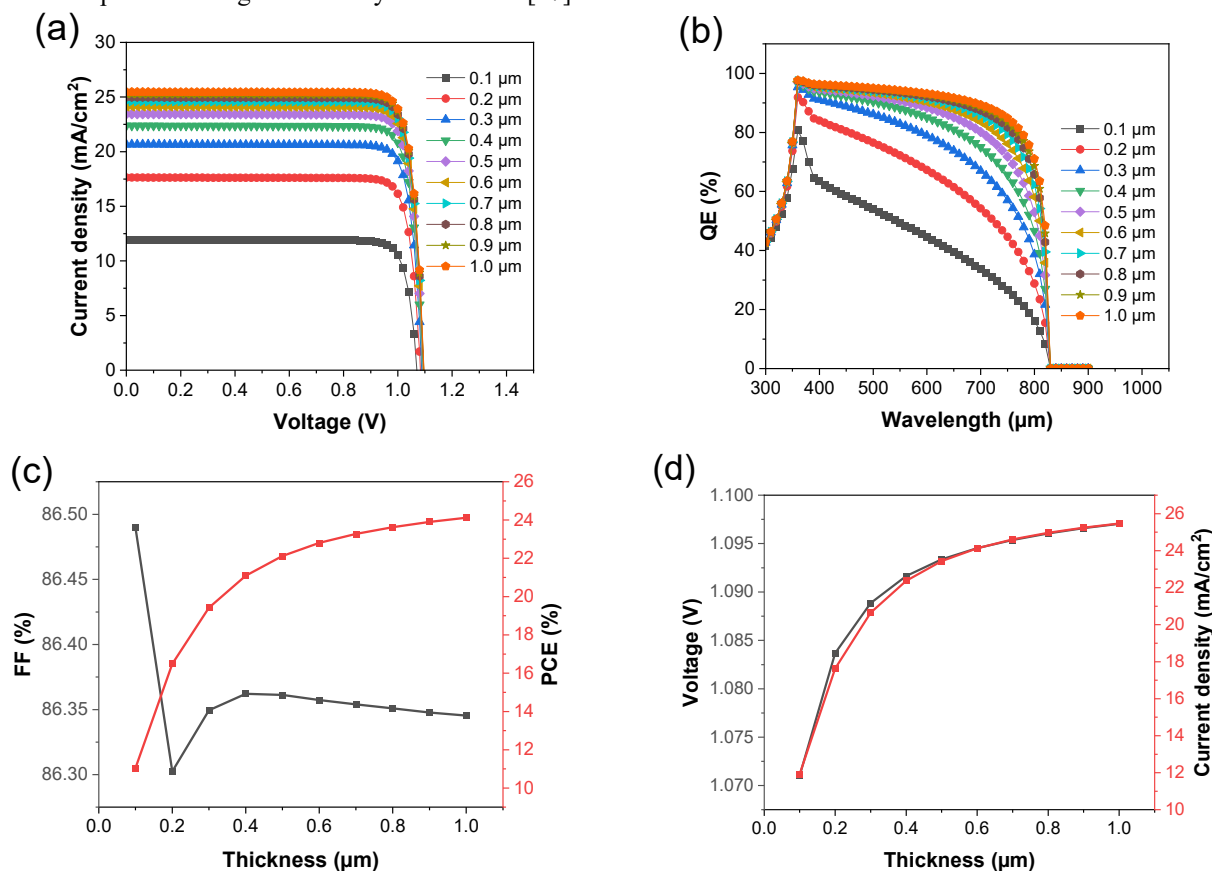


Figure 3. (a) *J-V* curve with varied absorber thickness under illumination, (b) QE curve with respect to wavelength, (c) PCE and FF with respect to thickness and (d) J_{sc} and V_{oc} with respect to varied absorber thickness

The fill factor decreases rapidly from 100 to 200 nm of absorbing layer thickness, before increasing slightly to a peak value of 400 nm of thickness, and finally decreases steadily when the absorbing layer thickness increases beyond 400 nm. The decrease in the value of FF in relation to absorber layer thickness is due to an increase in series resistance [28].

Therefore, the optimal thickness of the CsSnGeI₃ in our research work was 1000 nm and as such considered for further simulation. The device performance at that thickness gave the following metric performance: PCE = 24.122%, FF = 86.345%, J_{sc} = 25.466 mA/cm², and V_{oc} = 1.097 V.

The quantum efficiency versus wavelength plot for the device with varied thickness is shown in Figure 3b. The QE increases with increasing thickness of CsSnGeI₃ from 80% at 100 nm to 99.4% at 1000 nm. The strong QE is due to increase in absorption coefficient as the thickness increases [20].

3.3. Effect of absorbing layer defect density

The surface and bulk of the absorbing layer are prone to defects which are unavoidably present. In perovskite layers, lattice vacancy, interstitial, schottky, and frenkel defects are such defects which can be found as point defects [29]. When PSCs absorb

light, the absorbing layer in turn generates photoelectrons, and if the film quality is poor, there will be an increase in defect density, leading to quenching losses in absorbing layer which is a determining factor for the V_{oc} of the solar cell [19]. From research findings, in lead-free perovskites films, minimal grain boundary length and the carrier recombination occur due to their improved quality crystal grains. Long carrier diffusion length is responsible for decrease in further recombination which is observed in perovskite films with lesser defects [30, 31]. The Shockley-Read-Hall (SRH) recombination model can be used to study the impact of the absorbing layer defect density on the performance of a solar cell [32].

The defect density (N_t) of the absorbing layer was varied from 10^{14} to 10^{19} cm^{-3} and its impact on the device photovoltaic parameters is explored systematically. The $J-V$ curve and QE for varied N_t is shown in Figures 4a & b. Figures 4c & d show the correlation between PCE, FF, J_{sc} and V_{oc} with N_t . Increase in defect density of the absorbing layer, results to decrease in the photovoltaic parameters of the cell. This can be attributed to increase in the carrier recombination of the device [19]. From the values of 10^{16} to 10^{17} cm^{-3} , slight decrease was observed across all photovoltaic parameters. From the values of 10^{17} to 10^{18} cm^{-3} of defect density, a sharp decline across all photovoltaic parameters were observed, and finally a drastic fall in the performance of the device from 10^{18} to 10^{19} cm^{-3} . The optimized value of absorbing layer defect density was chosen as 10^{14} cm^{-3} with photovoltaic parameters: V_{oc} of 1.099 V, J_{sc} of 26.213 mA/cm^2 , FF of 86.336%, and PCE of 24.866%.

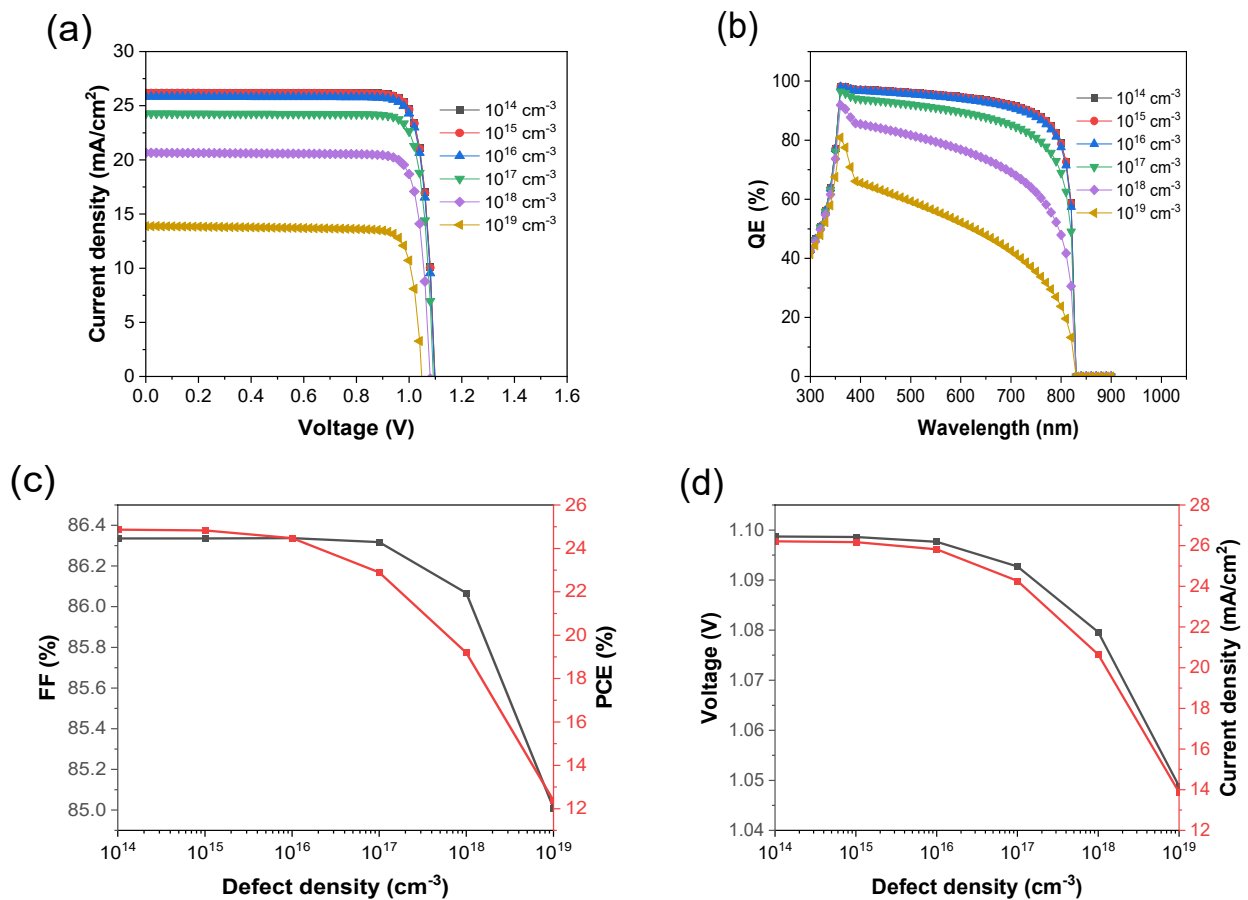


Figure 4. (a) $J-V$ curve with varied absorber defect density under illumination, (b) QE curve with respect to wavelength, (c) PCE and FF with respect to absorber defect density and (d) J_{sc} and V_{oc} with respect to varied absorber defect density

3.4. Effect of ETL thickness

The thickness of ETL can greatly affect the performance of solar devices [33]. The function of the ETL is tasked with blocking holes, extraction and transporting the photo-electrons in the absorbing layer and prevention of the charge carrier recombination of holes and electrons in the front electrode in the absorbing layer [34]. This parameter is very important for device optimization in order to enhance the performance of PSCs. The thickness of ETL was varied from 50 to 500 nm and the resulting variation in device photovoltaic parameters is shown in Figures 5a-d. Figures 5a & b show the $J-V$ plot and QE curve with varied ETL thickness while Figures 5c & d show the correlation of photovoltaic parameters with ETL thickness. It is observed that as the thickness of ETL increases, the performance of the device for simulated PSCs decreases. Steady decrease was observed through the V_{oc} , J_{sc} , and PCE of the device, as the thickness of the ETL increases. However, the FF increases steadily as there was increment in the ETL thickness. Optimal values were observed at the thickness value of 50 nm with V_{oc} of 1.099 V, J_{sc} of 26.190 mA/cm^2 , FF of 86.336%, and PCE of 24.841%. The optimal value was used for further simulation.

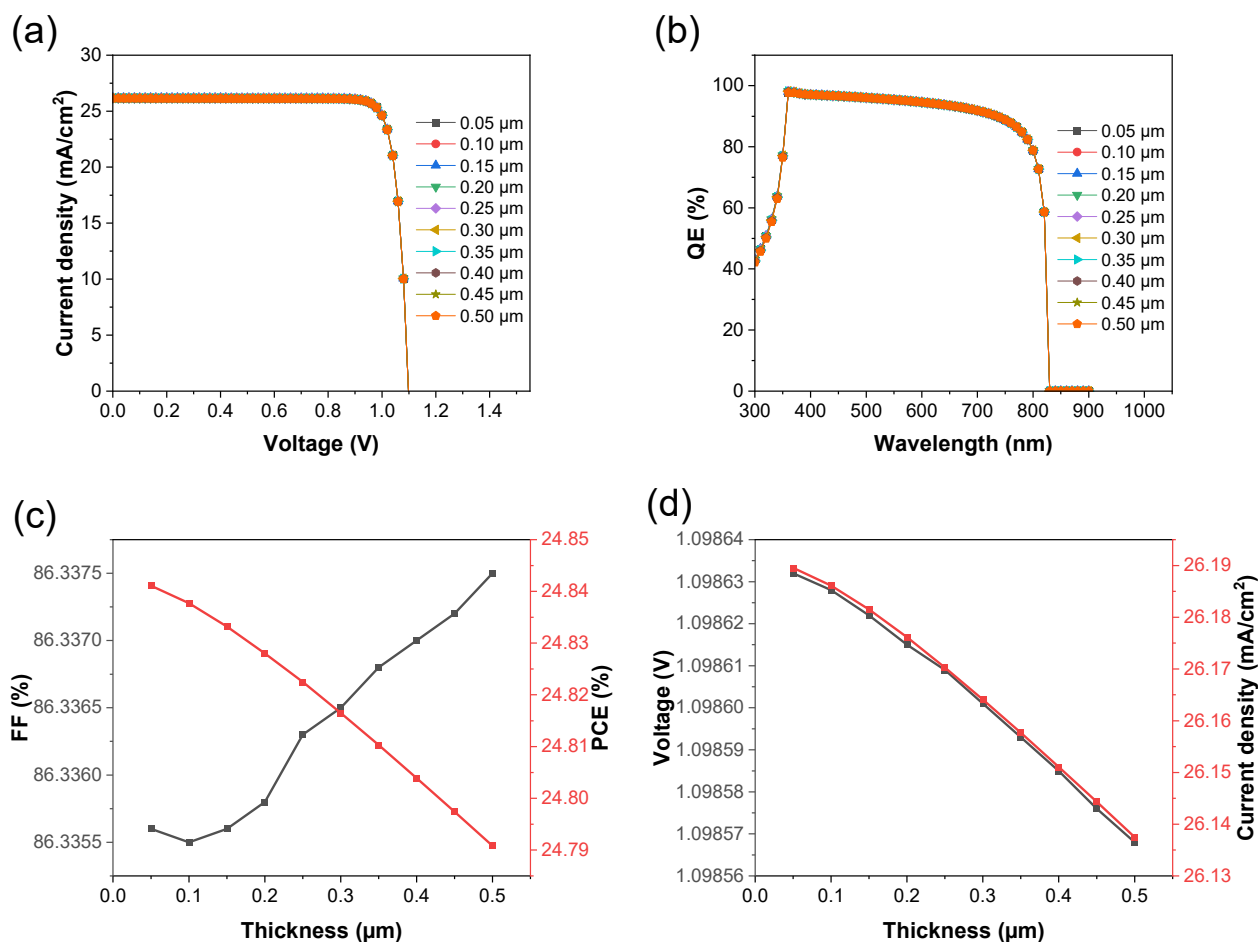


Figure 5. (a) J - V curve with varied ETL thickness under illumination, (b) QE curve with respect to wavelength, (c) PCE and FF with respect to ETL thickness and (d) J_{sc} and V_{oc} with respect to varied thickness

The chances of recombination are increased as the thickness of the ETL is increased, for the fact that charges take longer route of travel for diffusion to occur, leading to reduction in the PCE of the device. The efficiency decrease at a certain rate with corresponding increment in the ETL thickness, is apparently due to an increase in recombination [35,36]. Selecting the thickness from 50 to 500 nm results to spectral overlap in the QE versus Wavelength curve which is attributed to unchanged optical absorption efficiency within the selected values of thickness as shown in Figure 5b.

3.5. Effect of ETL doping concentration

Current generation is enhanced as electrons are being accelerated as a result of doping concentration of the ETL. The charge carrier conductivity is enhanced as there is an effective suppression of the ETL/absorber interface defects due to the introduction of n-type Al dopant in the ZnO ETL to replace the Zn^{2+} . The introduction of a donor level at 120 meV below the conduction band can lead to an appropriate band alignment, and an increase in the free carrier concentrations [37].

The doping concentration was varied from 10^{11} to 10^{19} cm⁻³ for the ETL. Figures 6a & b show the J - V behaviour and QE properties of the simulated device with varied ETL doping concentration while Figures 6c & d show the variation of performance parameters with doping concentration of ETL. There was a decrease in the V_{oc} , PCE and FF of the device as the doping concentration increased; steady decrease was observed in the V_{oc} before a rapid decrease was observed from 10^{18} to 10^{19} cm⁻³. The PCE of the device experiences an increase from the values of 10^{15} to 10^{17} cm⁻³, before following a declining path. The FF of the device experiences an increase from the values of 10^{13} to 10^{16} cm⁻³, before following a declining path. The J_{sc} of the device experiences an increase from the values of 10^{15} to 10^{17} cm⁻³. The optimized values of photovoltaic parameters were chosen at a V_{oc} of 1.149 V, J_{sc} of 25.922 mA/cm², FF of 88.260%, and PCE of 26.280% for an ETL doping concentration of 10^{17} cm⁻³. There was spectral overlap at the QE plot which shows an unchanged optical absorption within the selected doping concentration values.

3.6. Effect of back-metal contact work functions on the device

The back-metal contact is deposited over the perovskite absorber or HTM, for holes collection from the external circuit. The formation of an ohmic contact is vital to facilitate proper majority charge carrier collection (holes via the

back-metal contact). The work function of different back-metal contacts was studied to understand their effect on the performance of the device. The back-metal contact work functions studied were; Carbon (C) of 5.00 eV, Gold (Au) of 5.1 eV, Palladium (Pd) of 5.30 eV, and Platinum (Pt) of 5.65 eV.

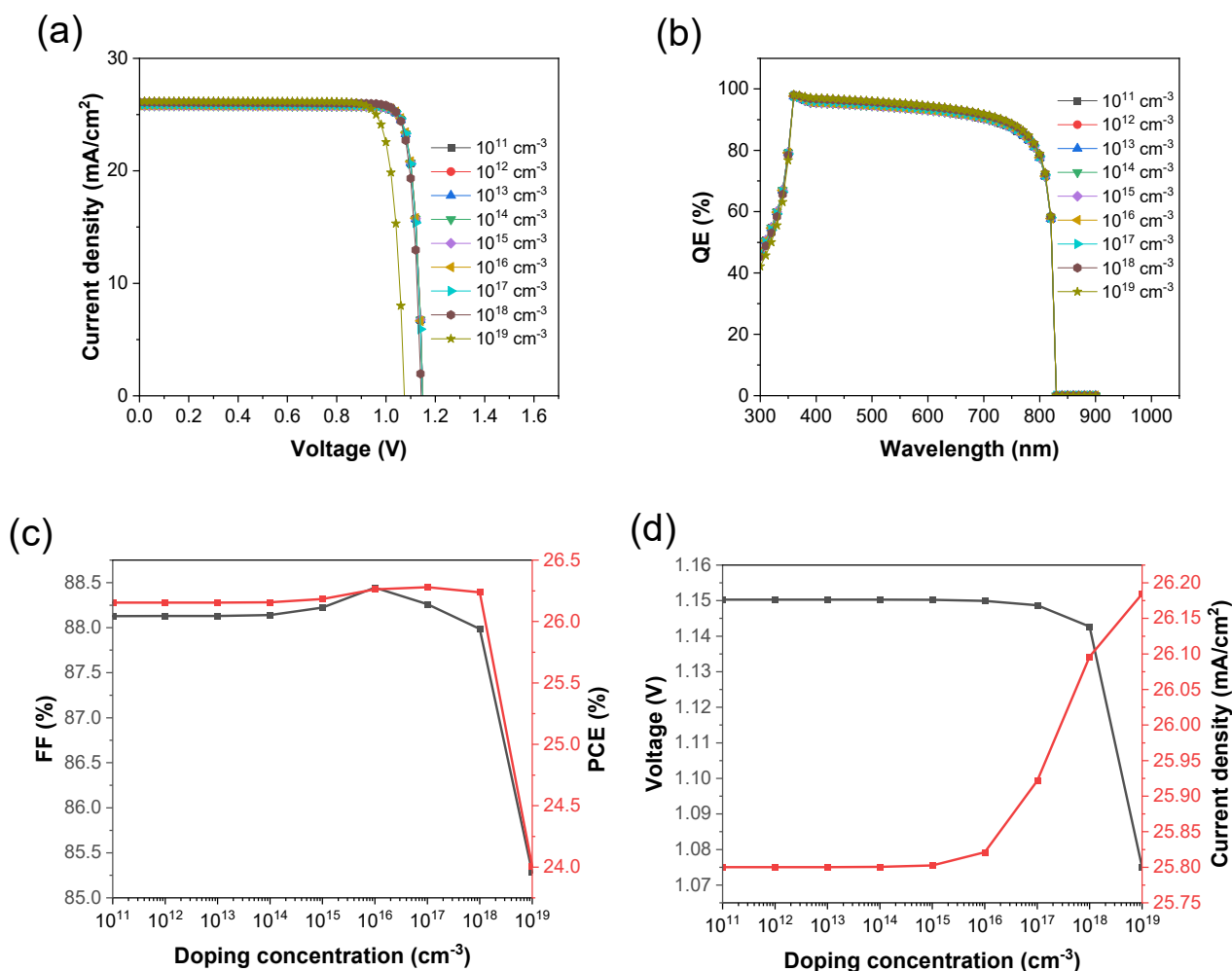


Figure 6. (a) J - V curve with varied doping concentration under illumination, (b) QE curve with respect to wavelength, (c) PCE and FF with respect to doping concentration and (d) J_{sc} and V_{oc} with respect to doping concentration

The impact of the back-metal contact work functions on the performance of the device is shown in Figures 7a-d with Figure 7a showing the J - V curve, 7b showing the QE and 7c & d showing the performance correlation with metal back contacts. As observed, when the back-metal work functions increased from 5.00 to 5.65 eV, there were no changes observed in the J_{sc} and V_{oc} values. The FF values increased from 86.277 to 86.344%, and PCE from 24.809 to 24.828%.

From the results obtained, it can be seen that, as the back-metal work functions increases, there is efficiency enhancement improving the performance of the device in turn. For this device, it can be concluded that a high PCE can be achieved when the back-metal work function is not less than 5.1 eV. The optimized values of photovoltaic parameters were chosen at a V_{oc} of 1.097 V, J_{sc} of 26.174 mA/cm², FF of 86.344%, and PCE of 24.828% for the back-metal contact of Pt with a work function of 5.65 eV for this device. There was spectral overlap at the QE plot which shows an unchanged optical absorption within the selected back-metal contact.

3.7. Effect of temperature on the device

Solar cells are generally installed outdoors, and the temperature will increase due to continuous solar radiation even higher than normal room temperature of 300 K. Therefore, it is necessary to understand the performance of the device with these variations in temperature. The device was varied from an operating temperature of 260 to 350 K subjected to constant illumination. The effect of temperature on the J - V curve is shown in Figure 8a. The correlation between the PCE, FF, J_{sc} and V_{oc} with temperature is shown in Figures 8b & c. From observation, as the temperature increases from 260 to 350 K, the V_{oc} decreases linearly from 1.150 to 1.034 V, the FF decreases steadily from 87.926 to 84.093%, and PCE decreases from 25.172 to 23.942%. However, the J_{sc} of the device increases steadily with temperature increase from 24.897 to 27.538 mA/cm².

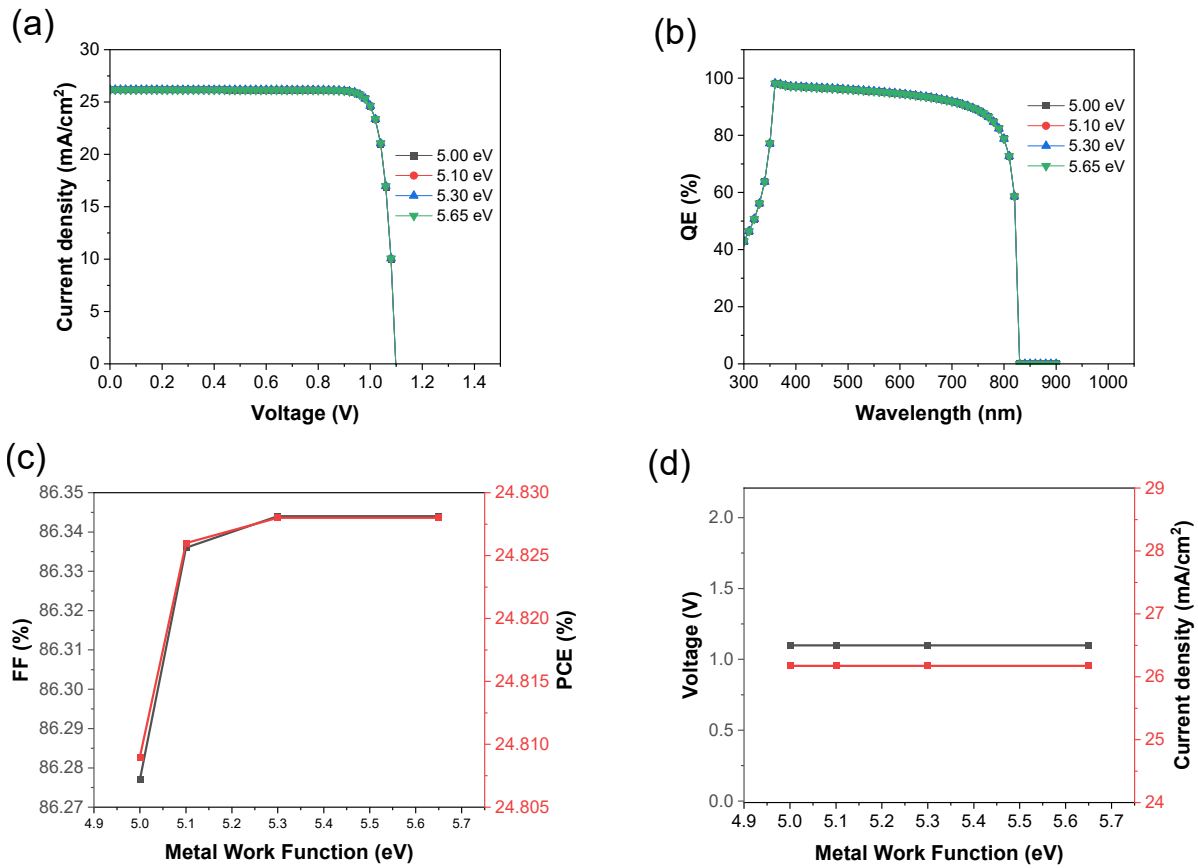


Figure 7. (a) $J-V$ curve with different metal contact under illumination, (b) QE curve with respect to wavelength with different metal contact, (c) PCE and FF with respect to metal contact and (d) J_{sc} and V_{oc} with respect to metal contact

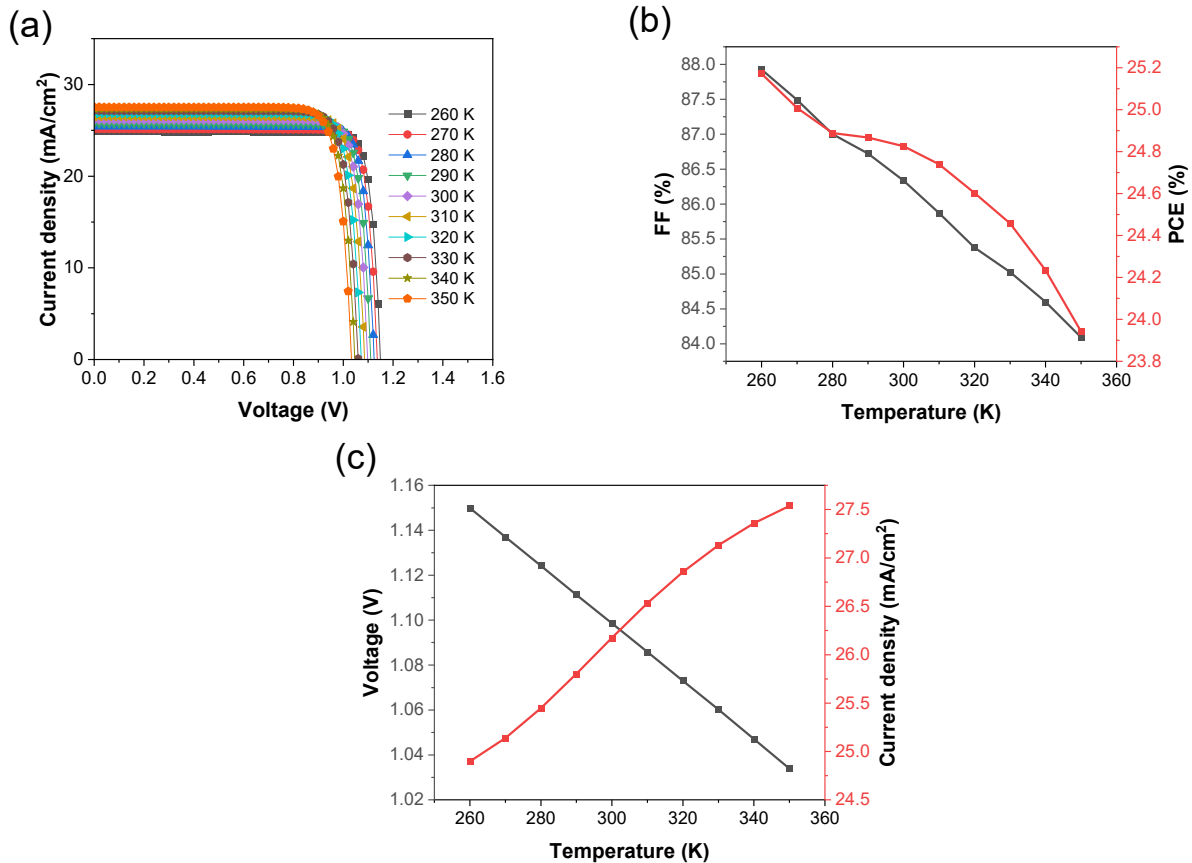


Figure 8. (a) $J-V$ curve with varied temperature under illumination, (b) PCE and FF with respect to temperature and (c) J_{sc} and V_{oc} with respect to temperature

The behavior exhibited by the J_{sc} is due to the metastable nature of the device at higher temperatures [38]. The electrons absorb enough photons and hence recombines with positive charge carriers that have been already generated, becoming a site for recombination, leading to an unstable state [38]. The decrease in V_{oc} is attributed to the increase in defects as the temperature of the device increases. Change in the resistance of the device occurs as the temperature increases which affects electron and hole mobilities, and the carrier concentration leading to a decrease in PCE.

3.8 Performance study of the initial and optimized device

The J - V characteristics of the initial and optimized perovskite solar cell device simulated under illumination is shown in Figure 9. Under illuminated condition, the performance of the optimal PSC is as follows: $V_{oc} = 1.145$ V, $J_{sc} = 25.241$ mA/cm², FF = 88.060% and PCE = 25.459%. Upon comparing with the initial device, an appreciable improvement of ~4.20%, ~2.00% and ~2.56% in V_{oc} , FF and PCE respectively were observed.

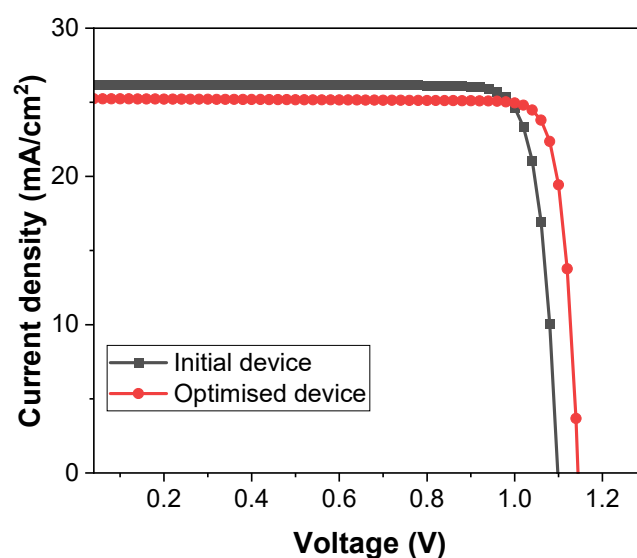


Figure 9. Initial and optimized of J - V curves the device

4. Conclusion

In this paper, the numerical investigation of lead-free CsSnGeI₃-based perovskite solar cell was performed using SCAPS-1D simulation software. The device performance was studied to achieve better efficiency with respect to (i) effect of the absorbing layer thickness, (ii) effect of absorbing layer defect density, (iii) effect of ETL thickness, (iv) effect of ETL doping concentration, (v) effect of back-metal contact work functions and (vi) effect of temperature on the device. Our study revealed that better photovoltaic parameters were obtained when the optimal values of the absorbing layer thickness was 1000 nm, the absorbing layer defect density was 10¹⁴ cm⁻³, the ETL thickness was 50 nm, the ETL doping concentration was 10¹⁷ cm⁻³ and the best performing back-metal contact was Pt with a work function of 5.65 eV. Also, the CsSnGeI₃-based perovskite solar cells are very sensitive to temperature with an optimized value of 260 K. There was significant degradation of PV parameters as the temperature of the device increases, adversely affecting material conductivity. The optimized device (FTO/ZnO:Al/CsSnGeI₃/CuI/Pt) gives PCE of 25.459%, V_{oc} of 1.145 V, J_{sc} of 25.241 mA/cm², and fill factor of 88.060%. A 2.56% improvement in PCE and 4.20% improvement in V_{oc} were obtained over the initial device. This numerical simulation paves better understanding on the choice of parameters leading to a high performing PSCs, stability enhancement and characterization.

Acknowledgments

The authors would like to thank Professor Marc Burgelman and his team from the Department of Electronics and Information Systems, University of Ghent, Belgium, for the development of the SCAPS software package and allowing its use.

Conflict of interest. Authors have declared that there is no conflict of interest.

Funding. This article did not receive any funding support.

ORCID IDs

Muhammed O. Abdulmalik, <https://orcid.org/0000-0002-3250-7864>;
 Eli Danladi, <https://orcid.org/0000-0001-5109-4690>
Francis U. Salifu, <https://orcid.org/0000-0001-9015-2347>

REFERENCES

- [1] S. Ameen, M.A. Rub, S.A. Kosa, K.A. Alamry, M.S. Akhtar, H.S. Shin, H.K. Seo, A.M. Asiri, and M.K. Nazeeruddin. ChemSusChem, 9, 10 (2016). <https://doi.org/10.1002/cssc.201501228>

- [2] A. Kojima, K. Teshima, Y. Shirai, and T. Miyasaka, *Journal of American Chemical Society*, **131**, 6050 (2009). <https://doi.org/10.1021/ja809598r>
- [3] M.A. Green, A. Ho-Baillie, and H.J. Snaith, *Nature Photonics*, **8**, 506 (2014). <https://doi.org/10.1038/nphoton.2014.134>
- [4] Z. Qu, F. Ma, Y. Zhao, X. Chu, S. Yu, and J. You, *Chinese Physics Letters*, **38**, 107801 (2021). <https://doi.org/10.1088/0256-307X/38/10/107801>
- [5] B. Ai, Z. Fan, and Z.J. Wong, *Microsystems & Nanoengineering*, **8**, 5 (2022). <https://doi.org/10.1038/s41378-021-00334-2>
- [6] Z.N. Jahanbakhshi, Z.M. Borhani, and M.R. Nateghi, *Thin Solid Films*, **671**, 139 (2019). <https://doi.org/10.1016/j.tsf.2018.12.029>
- [7] E. Danladi, M. Kashif, A. Ichoja, and B.B. Ayiwa, *Transactions of Tianjin University*, **28**(5), (2022). <https://doi.org/10.1007/s12209-022-00343-w>
- [8] G. Pindolia, S. M. Shinde, and P.K. Jha, *Solar Energy*, **236**, 802 (2022). <https://doi.org/10.1016/j.solener.2022.03.053>
- [9] W. Ke, and M.G. Kanatzidis, *Nature Communications*, **10**, 965 (2019). <https://doi.org/10.1038/s41467-019-08918-3>
- [10] N.K. Noel, S.D. Stranks, A. Abate, C. Wehrenfennig, S. Guarnera, A.A. Haghighirad, A. Sadhanala, G.E. Eperon, S.K. Pathak, M.B. Johnston, A. Petrozza, L.M. Herz, and H.J. Snaith, *Energy & Environmental Science*, **7**, 3061 (2014). <https://doi.org/10.1039/C4EE01076K>
- [11] M. Roknuzzaman, K. Ostrikov, H. Wang, A. Du, and T. Tesfamichael, *Scientific Reports*, **7**, 14025 (2017). <https://doi.org/10.1038/s41598-017-13172-y>
- [12] D. Sabba, H.K. Mulmudi, R.R. Prabhakar, T. Krishnamoorthy, T. Baikie, P.P. Boix, S. Mhaisalkar, and N. Mathews, *Journal of Physical Chemistry C*, **119**, 1763–1767 (2015). <https://doi.org/10.1021/jp5126624>
- [13] M.H. Kumar, S. Dharani, W.L. Leong, P.P. Boix, R.R. Prabhakar, T. Baikie, C. Shi, H. Ding, R. Ramesh, M. Asta, M. Graetzel, S.G. Mhaisalkar, and N. Mathews, *Advanced Materials*, **26**, 7122–7127 (2014). <https://doi.org/10.1002/adma.201401991>
- [14] B. Wu, Y. Zhou, G. Xing, Q. Xu, H.F. Garces, A. Solanki, T.W. Goh, N.P. Padture, and T.C. Sum, *Advanced Functional Materials*, **27**, 1604818 (2017). <https://doi.org/10.1002/adfm.201604818>
- [15] H. Wei, P. Qiu, Y.E. Li, Y. He, M. Peng, X. Zheng, and X. Liu, *Ceramics International*, **48**(5), 5876 (2021). <https://doi.org/10.1016/j.ceramint.2021.11.184>
- [16] M. Chen, M.G. Ju, H.F. Garces, A.D. Carl, L.K. Ono, Z. Hawash, Y. Zhang, T. Shen, Y. Qi, R.L. Grimm, D. Pacifici, X.C. Zeng, Y. Zhou, and N.P. Padture, *Nature Communications*, **10**, 16 (2019). <https://doi.org/10.1038/s41467-018-07951-y>
- [17] M.G. Ju, M. Chen, Y. Zhou, J. Dai, L. Ma, N.P. Padture, and X.C. Zeng, *Joule*, **2**, 1231 (2018). <https://doi.org/10.1016/j.joule.2018.04.026>
- [18] T. Leijtens, G.E. Eperon, N.K. Noel, S.N. Habisreutinger, A. Petrozza, and H.J. Snaith, *Advanced Energy Materials*, **5**, 1500963 (2015). <https://doi.org/10.1002/aenm.201500963>
- [19] O.A. Muhammed, E. Danladi, P.H. Boduku, J. Tasiu, M.S. Ahmad, and N. Usman, *East European Journal of Physics*, **2**, 146 (2021). <https://doi.org/10.26565/2312-4334-2021-2-12>
- [20] E. Danladi, M.Y. Onimisi, S. Garba, R.U. Ugbe, J.A. Owolabi, O.O. Ige, G.J. Ibeh, and A.O. Muhammed, *Journal of the Nigerian Society of Physical Sciences*, **1**, 72 (2019). <https://doi.org/10.46481/jnsps.2019.13>
- [21] A. Tara, V. Bharti, S. Sharma, and R. Gupta, *Optical Materials*, **128**, 112403 (2022). <https://doi.org/10.1016/j.optmat.2022.112403>
- [22] H. Pan, X. Zhao, X. Gong, H. Li, N.H. Ladi, X.L. Zhang, W. Huang, S. Ahmad, L. Ding, Y. Shen, M. Wang, and Y. Fu, *Materials Horizons*, **7**, 2276 (2020). <https://doi.org/10.1039/D0MH00586J>
- [23] N.S.N. M. Alias, F. Arith, A.N. Mustafa, M.M. Ismail, N.F. Azmi, and M.S. Saidon, *Journal of Engineering and Technological Sciences*, **54**(4), 220409 (2022). <https://doi.org/10.5614/j.eng.technol.sci.2022.54.4.9>
- [24] M.F.M. Noh, C.H. Teh, R. Daik, E.L. Lim, C.C. Yap, M.A. Ibrahim, N.A. Ludin, A.R.B.M. Yusoff, J. Jang, and M.A.M. Teridi, *Journal of Materials Chemistry C*, **6**, 682 (2018). <https://doi.org/10.1039/C7TC04649A>
- [25] H. Sabbah, *Materials*, **15**, 3229 (2022). <https://doi.org/10.3390/ma15093229>
- [26] N. Singh, A. Agarwal, and M. Agarwal, *Superlattices and Microstructures*, **149**, 106750 (2021). <https://doi.org/10.1016/j.spmi.2020.106750>
- [27] S.M. Seyed-Talebi, and J. Beheshtian, *International Journal of Energy and Power Engineering*, **15**(6), 252 (2021).
- [28] K. Chakraborty, M.G. Choudhury, and S. Paul, *Solar Energy*, **194**, 886 (2019). <https://doi.org/10.1016/j.solener.2019.11.005>
- [29] F. Hao, C.C. Stoumpos, D.H. Cao, R.P. Chang, and M.G. Kanatzidis, *Nature Photonics*, **8**(6), 489 (2014). <https://doi.org/10.1038/nphoton.2014.82>
- [30] W. Ning, F. Wang, B. Wu, J. Lu, Z. Yan, X. Liu, Y. Tao, J.M. Liu, W. Huang, M. Fahlman, and L. Hultman, *Advanced Materials*, **30**(20), 1706246 (2018). <http://dx.doi.org/10.1002/adma.201706246>
- [31] S.Z. Haider, H. Anwar, and M. Wang, *Semiconductor Science and Technology*, **33**(3), 035001 (2018). <https://doi.org/10.1088/1361-6641/aaa596>
- [32] C.M. Wolff, P. Caprioglio, M. Stolterfoht, and D. Neher, *Advanced Materials*, **31**(52), 1902762 (2019). <http://dx.doi.org/10.1002/adma.201902762>
- [33] M.I. Hossain, F.H. Alharbi, and N. Tabet, *Solar Energy*, **120**, 370 (2015). <https://doi.org/10.1016/j.solener.2015.07.040>
- [34] C.S. Solanki, *Solar Photovoltaics: Fundamentals, Technologies and Applications*, (PHI Learning Pvt. Ltd., New Delhi, 2015).
- [35] F. Anwar, R. Mahbub, S.S. Satter, and S.M. Ullah, *International Journal of Photoenergy*, Article ID 9846310, (2017). <https://doi.org/10.1155/2017/9846310>
- [36] J.P. Correa-Baena, M. Anaya, G. Lozano, W. Tress, K. Domanski, M. Saliba, T. Matsui, T.J. Jacobsson, M.E. Calvo, A. Abate, M. Grätzel, H. Míguez, and A. Hagfeldt, *Advanced Materials*, **28**(5031), 7 (2016). <https://doi.org/10.1002/adma.201600624>
- [37] A. Mahmood, T. Munir, M. Fakhar-e-Alam, M. Atif, K. Shazad, K.S. Alimgeer, T.G. Nguyen H. Ahmad, and S. Ahmad, *Journal of King Saud University-Science*, **34**(2), 101796, (2022). <https://doi.org/10.1016/j.jksus.2021.101796>
- [38] E. Danladi, M. Kashif, T.O. Daniel, C.U. Achem, M. Alpha, and M. Gyan, *East European Journal of Physics*, **3**, 19 (2022). <https://doi.org/10.26565/2312-4334-2022-3-03>

ЧИСЕЛЬНЕ ДОСЛІДЖЕННЯ 25,459% ЛЕГОВАНОГО НЕОРГАНІЧНОГО БЕЗСВИНЦЕВОГО СОНЯЧНОГО ЕЛЕМЕНТА НА ОСНОВІ ПЕРОВСКІТУ CsSnGeI₃ ШЛЯХОМ СИМУЛЯЦІЇ ПРИСТРОЮМухаммед О. Абдулмалік^a, Елі Данладі^b, Ріта С. Обасі^c, Філібус М. Гюк^d,Френсіс У. Саліфу^a, Сулейман Магаджі^e, Анселем С. Егбуга^f, Даніель Томас^d^aФізичний факультет, Науково-технологічний університет Конфлюенс, Осара, штат Когі, Нігерія^bФізичний факультет Федеральний університет наук про здоров'я, Отукпо, штат Бенуе, Нігерія^cЦентр розвитку супутникових технологій NASRDA, Абуджа, Нігерія^dФізичний факультет, Університет штату Кадуна, Кадуна, Нігерія^eФакультет електроніки та інженерії зв'язку, Нігерійська оборонна академія, Кадуна, Нігерія^fОпераційний підрозділ, Starsight Energy, Нігерія

Токсичний свинцевий компонент, а також дорогий і менш стабільний spiro-OMeTAD у перовскітних сонячних елементах (PSC) створюють велику перешкоду для їх комерційної життєздатності. У цьому дослідженні було запропоновано та реалізовано обчислювальний підхід до моделювання та симуляції всіх неорганічних перовскітних сонячних елементів на основі цезію олова-германію (CsSnGeI₃) за допомогою інструменту імітатора ємності сонячних елементів (SCAPS-1D). Допований алюмінієм оксид цинку (ZnO:Al) і йодид міді (CuI) використовувалися як транспортні шари електронів і дірок (ETL і HTL) відповідно. Початковий пристрій без будь-якої оптимізації дав ефективність перетворення потужності (PCE) 24,826%, коефіцієнт заповнення (FF) 86,336%, щільність струму короткого замикання (J_{sc}) 26,174 мА/см² і напругу холостого ходу (V_{oc}) 1,099 В. При зміні вищезазначених параметрів індивідуально, зберігаючи інші незмінними, оптимальні значення становлять 1000 нм для товщини поглинача, 10¹⁴ см⁻³ для щільності дефектів шару поглинача, 50 нм для товщини ETL, 10¹⁷ см⁻³ для концентрації легування ETL і 260 К для температури. Моделювання з цими оптимізованими значеннями призводить до PCE 25,459%, V_{oc} 1,145 В, J_{sc} 25,241 мА/см² і FF 88,060%. Ці результати вказують на те, що CsSnGeI₃ є життєздатним альтернативним поглинаючим шаром для використання в конструкції перовскітного сонячного елемента з високим PCE.

Ключові слова: перовскітні сонячні елементи, SCAPS-1D, CsSnGeI₃, дірковий транспортний матеріал, електротранспортний матеріал

ASSESSMENT OF EXPLICIT MODELS BASED ON THE LAMBERT W-FUNCTION FOR MODELING AND SIMULATION OF DIFFERENT DYE-SENSITIZED SOLAR CELLS (DSSCs)[†]

 Jamu B. Yerima^{a,*},  Dunama William^b,  Alkali Babangida^c,  Sabastine C. Ezike^a

^aDepartment of Physics, Modibbo Adama University Yola, Nigeria

^bDepartment of mathematics, Modibbo Adama University Yola, Nigeria

^cDepartment of Science Education, COE Azare, Bauchi State, Nigeria

*Corresponding author: bjyerima@gmail.com

Received August 20, 2022; revised September 9, 2022; accepted September 17, 2022

In this paper, the characteristic points were used as input data in five different explicit models based on Lambert W-function for the extraction of model parameters of three DSSCs. Moreover, these model parameters for given values of voltages were used to obtain the corresponding currents for the simulation of the DSSCs. The results show that the sign of the model parameter does not matter for methods that do not have series resistance and shunt resistance. However, when R_{sh} was negative the five-parameter single-diode model failed to yield good curve fit except when R_{sh} was neglected and four-parameter model used. Moreover, all the model parameters for DSSCs with bitter gourd dye were regular and yielded good curve fit for all the models. On the hand, DSSCs with R_{sh} values negative were handled with four-parameter model to obtain good curve fit. Thus, the sign of model parameter matters in simulation of DSSC using single-diode model.

Keywords: Model parameter, Explicit model, Lambert W-function, Characteristic points, DSSC, Curve fit

PACS: 2010: 88.90.+t, 88.40H-, 88.40.hj, 42.79.Ek.

INTRODUCTION

Nowadays, renewable energy plays a great role in reducing fossil resources consumption [1] due to problems arising from the use of fossil resources such as global warming, climate change, and air pollution [2] to mention a few. Presently, among the various renewable energy sources, solar energy is likely the most applicable, as it is clean, safe, and unlimited [3,4]. In one year, the amount of solar energy received from the sun is 10^4 times greater than the world's energy consumption [4]. It has been revealed the installed photovoltaic power increased from 100.9 GW in 2012 to 230 GW in 2015, rising to 400 GW in 2017 [1, 5]. This rate of increase has been feasible due to a new brand of solar cells that permit production growth while reducing costs and environmental impact [6].

Modeling has become a crucial step for photovoltaic system design and development, as it permits appropriate and accurate energy production forecasts [7]. The modeling of solar cells/panels is usually performed by using equivalent circuit models represented with mathematically implicit equations which are not easy to solve. However, the Lambert W-function has been identified as a useful tool to solve these equations.

The purpose of this paper is to present simplified model expressions in terms of the Lambert W-function, which is usually applied in photovoltaic devices, and depicts how this function is needed to solve equations connected to these systems. The desired model expressions were obtained by matching famous mathematical equations (exponential functions, polynomials, hyperbolic functions) to points on the Lambert W-function calculated numerically with the highest available accuracy.

The approach presented in this paper is to apply simplified model equations based on the Lambert W-function that can be solved easily with a pocket calculator, to model and simulate DSSC systems behavior.

MATERIALS AND METHODS

Modeling and simulation of solar cells

A host of researchers have reported that ideal solar cells behave like a current source connected in parallel with a diode [7-9]. This ideal model is achieved with resistors to represent the losses and sometimes with additional diodes that takes into account other phenomena [10,11]. The most common circuit equivalent to a solar cell consists of a current source, one diode and two resistors; one in series and one in parallel [12-19]. It is worth noting each of the element in the equivalent circuit one parameter has to be calculated except two in the case of the diode whose behavior is represented by the Shockley equation [20]. Thus, five parameters are required to be determined when applying this method [21-33]. This simple equivalent circuit has been used quite well to reproduce the current-voltage curve or simply I-V curve. Three important points of the I-V curve known as characteristic points namely: short circuit, maximum power, and open circuit points are used as input data. These representative points depend on temperature, irradiance of the photocurrent source, characteristic points and usually the normal information included in the manufacturer's datasheets.

[†] Cite as: A. J.B. Yerima, D. William, A. Babangida, and S.C. Ezike, East Eur. J. Phys. 4, 136 (2022), <https://doi.org/10.26565/2312-4334-2022-4-13>
© J.B. Yerima, D. William, A. Babangida, S.C. Ezike, 2022

The conventional equation (1) describes a simple diode with a distinctive I-V curve

$$I = I_o \left(e^{\frac{V}{a}} - 1 \right), \tag{1}$$

where a is the modified ideality diode factor (quality factor or emission coefficient) which varies with the nature of diode is determined according to the fabrication process and the semiconductor material.

When the semiconductor is illuminated, it will produce a photo-generated current I_{ph} , which will result in a vertical translation of the I-V curve of a quantity that is almost entirely related to the surface density of the incident energy. The equivalent circuit solar cell containing series resistance R_s , shunt resistance R_{sh} , photocurrent I_{ph} , diode saturation current I_o , modified diode ideality factor, a is depicted in Fig. 1.

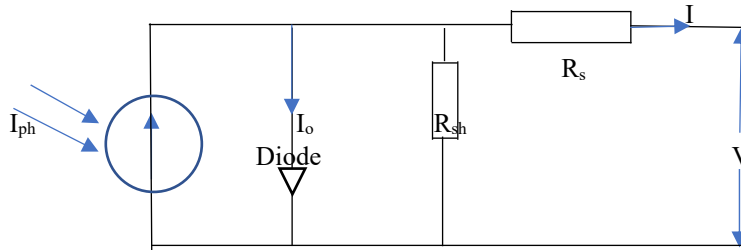


Figure 1. Electrical equivalent circuit of the single-diode solar cell

The single-diode model assumes an ideal cell is pictured as a current generator that is linked to a parallel diode with an I-V characteristic which is mathematically defined by Schokley equation (2)

$$I = I_{ph} - I_o \left(e^{\frac{V+IR_s}{a}} - 1 \right) - \frac{V+IR_s}{R_{sh}}, \tag{2}$$

where I and V are the terminal current and voltage respectively, I_o the junction reverse current, a is the modified junction ideality factor, R_s and R_{sh} are the series and shunt resistance respectively.

Equation (2) is transcendental in nature hence it is not possible to solve for V in terms of I and vice versa. However, explicit solutions can be obtained using the principal branch of the Lambert W-function W_o [21, 34-37].

$$I = \frac{R_{sh}(I_{ph}+I_o)-V}{R_{sh}+R_s} - \frac{a}{R_s} W_o \left(\frac{R_{sh}R_s I_o}{a(R_{sh}+R_s)} e^{\left(\frac{R_{sh}R_s(I_{ph}+I_o)+VR_{sh}}{a(R_{sh}+R_s)} \right)} \right), \tag{3}$$

$$V = R_{sh}(I_{ph} + I_o) - (R_s+R_{sh})I - aW_o \left\{ \frac{R_{sh}I_o}{a} e^{R_{sh}\left(\frac{I_{ph}+I_o-I}{a}\right)} \right\}. \tag{4}$$

One can directly find the current for a given value of voltage using equation (3) or the voltage via (4), which makes the computation easy and robust in contrast to (2). The Lambert W function is readily available in all computation procedures [21, 35]. Finally, for simulation purpose the current can be calculated for each model by plugging the appropriate model parameters for any given value of V into equation (3) and vice versa for V for any given value of I in equation (4). However, if the curve fit fails due to parameter irregularity, for example R_{sh} negative or complex we neglect $R_{sh}=\infty$, the last term in equation (2) vanishes reducing the five-parameter model to four-parameter model. Therefore, equation (3) reduces to equations (5)

$$I = I_{ph} + I_o - \frac{a}{R_s} W_o \left(\frac{R_s I_o}{a} e^{\left(\frac{R_s(I_{ph}+I_o)+V}{a} \right)} \right). \tag{5}$$

Furthermore, if equation (5) fails to yield good curve fit then R_s is neglected and equation (2) reduces to the ideal diode equation (1) representing a three-parameter model. Thus, equations (1), (3) and (5) can be used for simulation of three-, four- and five-parameter models respectively.

The explicit model equations based on the Lambert W-function

There are many explicit models to study the current-voltage behavior of a solar cell [38]. Notwithstanding, the results do not sustain any of the physical appearance of the photovoltaic conversion process, they are attracting great attention and accurate enough to produce recent discoveries from time to time [39]. Some of the explicit models with solutions based on the Lambert W-function include:

I. The El-Tayyan model [40]. The proposed El-Tayyan model equation for generating I-V characteristics of solar cell or PV module is in the form

$$I = I_{sc} - C_1 e^{\left(\frac{-Voc}{c_2} \right)} \left(e^{\left(\frac{V}{c_2} \right)} - 1 \right), \tag{6}$$

where C_1 and C_2 are coefficients of the model equation. These coefficients are given by [41] as

$$C_1 = \frac{I_{sc}}{1 - e^{\left(\frac{-V_{oc}}{C_2}\right)}} \tag{7}$$

and, if $V_{oc}/C_2 \gg 1$:

$$C_2 = \frac{V_{mp} - V_{oc}}{W_{-1}\left(\left(1 - \frac{V_{oc}}{V_{mp}}\right)\left(\frac{I_{mp}}{I_{sc}}\right)\right)} \tag{8}$$

However, Babangida [42] have shown that the relationships between the conventional model parameters (I_o and a) and the El-Tayyan coefficients (C_1, C_2) are given by equations (9) and (10)

$$I_o = C_1 e^{-\frac{V_{oc}}{C_2}}, \tag{9}$$

$$a = C_2. \tag{10}$$

Thus, a and I_o in equations (9) and (10) are the two model parameters for the El-Tayyan model.

II. The Karmalkar and Haneefa model [43]. This model presents the current-voltage relation as

$$I = I_{sc} \left\{ 1 - \left(1 - \gamma \left(\frac{V}{V_{oc}} \right) \right) - \gamma \left(\frac{V}{V_{oc}} \right)^m \right\}, \tag{11}$$

where the model parameters are:

$$\gamma = \frac{2\left(\frac{I_{mp}}{I_{sc}}\right) - 1}{(m-1)\left(\frac{V_{mp}}{V_{oc}}\right)^m}, \tag{12}$$

$$m = \frac{W_{-1}\left[\left(\frac{V_{oc}}{V_{mp}}\right)^{\frac{1}{K}} \ln\left(\frac{V_{mp}}{V_{oc}}\right)\right]}{\ln\left(\frac{V_{mp}}{V_{oc}}\right)} + \frac{1}{K} + 1, \tag{13}$$

$$K = \frac{1 - \left(\frac{I_{mp}}{I_{sc}}\right) - \left(\frac{V_{mp}}{V_{oc}}\right)}{2\left(\frac{I_{mp}}{I_{sc}}\right) - 1}. \tag{14}$$

III. The Das model [44]. The current-voltage for this model is given by

$$I = I_{sc} \left[\frac{1 - \left(\frac{V}{V_{oc}}\right)^k}{1 + h\left(\frac{V}{V_{oc}}\right)} \right], \tag{15}$$

where the coefficients are:

$$k = \frac{W_{-1}\left[\left(\frac{I_{mp}}{I_{sc}}\right) \ln\left(\frac{V_{mp}}{V_{sc}}\right)\right]}{\ln\left(\frac{V_{mp}}{V_{oc}}\right)}, \tag{16}$$

$$h = \left(\frac{V_{oc}}{V_{mp}}\right) \left(\frac{I_{sc}}{I_{mp}} - \frac{1}{k} - 1\right). \tag{17}$$

IV. The Saetre [45] and Das model [44]. This model was proposed independently by Das [41] and Saetre [42] given by the following equation

$$I = I_{sc} \left[1 - \left(\frac{V}{V_{oc}}\right)^f \right]^{\frac{1}{g}}, \tag{18}$$

where the model parameters f and g are estimated with output current measurements at $V=0.8V_{oc}$ and $V=0.9V_{oc}$.

Using the maximum power point conditions, $(v, i) = (\alpha, \beta)$ and $\frac{\partial i}{\partial v} |_{mp} = -\frac{\beta}{\alpha}$, such that $\alpha = \frac{V_{mp}}{V_{oc}}$ and $\beta = \frac{I_{mp}}{I_{sc}}$, the following equations are obtained:

$$\beta^g = 1 - \alpha^f, \tag{19}$$

$$g\beta^g = f\alpha^f. \tag{20}$$

Assuming $\alpha^f \ll 1$, then

$$g \ln \beta = -\alpha^f. \tag{21}$$

Therefore, plugging equation (21) into equation (20), the equations for f and g are finally given by

$$f = W_{-1}\left(\frac{-\alpha}{\ln \beta}\right), \tag{22}$$

$$g = \frac{-\alpha^f}{\ln \beta}. \tag{23}$$

V. The 1-diode/2-resistors equivalent circuit model. The mathematical form of this model is already defined by equation (2) whose solution for I or V in terms of Lambert W-function is given by equation (3) or (4) respectively. Many researchers like [35] have published a solution of equation (2) based on the Lambert W-function which requires the diode ideality factor n as an input, say n=1.1 for the silicon cells studied and R_s is determined via equation (24).

$$R_s = A[W_{-1}(Be^C) - (C + D)]. \tag{24}$$

where W_{-1} is the lower branch of the Lambert W-function and A, B, C, and D auxiliary parameters defined as:

$$A = \frac{a}{I_{mp}}, \quad B = \frac{V_{mp}(I_{sc} - 2I_{mp})}{[V_{mp}I_{sc} + V_{oc}(I_{mp} - I_{sc})]}, \tag{25}$$

$$C = \frac{V_{oc} - 2V_{mp}}{a} + \frac{V_{mp}I_{sc} - V_{oc}I_{mp}}{[V_{mp}I_{sc} + V_{oc}(I_{mp} - I_{sc})]}, \quad D = \frac{V_{mp} - V_{oc}}{a}. \tag{26}$$

Most often the modified diode ideality factor a in terms of n and the thermal voltage V_T is defined by equation (27)

$$a = nV_T \tag{27}$$

such that V_T is also defined by equation (27)

$$V_T = \frac{kT}{q} \tag{28}$$

where k is the Boltzmann constant, T is the absolute temperature and q is the electron charge. In another vein, [43] avoided the assumption of the value of n instead he deduced that the modified diode ideality factor a is equal to the second El Tayan coefficient C_2 i.e he set $a=C_2$ given by equation (29)

$$a = \frac{V_{mp} - V_{oc}}{W_{-1}\left(\left(1 - \frac{V_{oc}}{V_{mp}}\right)\left(\frac{I_{mp}}{I_{sc}}\right)\right)}. \tag{29}$$

Furthermore, the parameter R_{sh} is calculated via [21] equation (30)

$$R_{sh} = \frac{(V_{mp} - I_{mp}R_s)(V_{mp} - R_s(I_{sc} - I_{mp}) - a)}{(V_{mp} - I_{mp}R_s)(I_{sc} - I_{mp}) - aI_{mp}}. \tag{30}$$

Finally, the remaining parameters I_o and I_{ph} are found by equations (31) and (32) respectively

$$I_o = \left[I_{sc} \left(1 + \frac{R_s}{R_{sh}} \right) - \frac{V_{oc}}{R_{sh}} \right] e^{-\frac{V_{oc}}{a}}, \tag{31}$$

$$I_{ph} = I_{sc} \left(1 + \frac{R_s}{R_{sh}} \right). \tag{32}$$

In this paper, equations (24) and (29-32) are used to extract the five model parameters (a, R_s , R_{sh} , I_o , and I_{ph}) to study the performance of DSSCs.

RESULTS AND DISCUSSION

Table 1. The characteristic points for three DSSCs

Source of natural dye		Characteristic points			
English Name	Scientific Name	I_{sc} (mA)	I_{mp} (mA)	V_{mp} (V)	V_{oc} (V)
Bitter gourd	Momordica charantia	9.244	6.450	0.4	0.536
Bougainvillea	Bougainvillea	3.450	2.783	0.3	0.484
Mango peel	Mangifera indica	2.51	2.130	0.4	0.618

In Table 1, the characteristic or representative points namely the short circuit point ($I_{sc}, 0$), open circuit point ($0, V_{oc}$) and the maximum power point (I_{mp}, V_{mp}) were obtained from the I-V curves of measured currents and voltages for three DSSCs are included. These points were used as input data for the modeling and simulation of the DSSCs studied.

Table 2. The El Tayyan model parameter for three DSSCs

Source of natural dye		Parameter model	
English Name	Scientific Name	C_1	C_2
Bitter gourd	Momordica charantia	0.009245	0.060353
Bougainvillea	Bougainvillea	0.003927	0.229684
Mango peel	Mongifera indica	0.002760	0.257501

Table 2 contains the two parameters for the 2-parameter El Tayyan model and both parameters are positive and less than unity. This means the parameters are regular parameters. The two parameters are inversely proportional to each other.

Table 3. The Karmalkar and Haneefa model parameter for three DSSCs

Source of natural dye		Parameter model		
English Name	Scientific Name	Υ	m	K
Bitter gourd	Momordica charantia	0.758887	9.611764	-1.12783
Bougainvillea	Bougainvillea	1.846619	1.777069	-0.69538
Mango peel	Mongifera indica	1.394703	2.453534	-0.71120

Table 3 depicts the three parameters of the Karmalkar and Haneefa 3-parameter model. Two of the parameters, γ and m , have positive values whereas the parameter K has all values negative. This implies that γ and m are regular parameters and K is irregular parameter. The three parameters are inversely proportional to one another.

Table 4. The Das model parameter for three DSSCs

Source of natural dye		model parameter	
English Name	Scientific Name	k	h
Bitter gourd	Momordica charantia	8.584082	0.428833
Bougainvillea	Bougainvillea	2.024451	-0.410257
Mango peel	Mongifera indica	2.293207	-0.398095

Table 4 contains the two parameters (k and h) for the 2-parameter Das model. The parameter k has positive values for all DSSCs while h negative value for DSSC with bitter gourd dye and positive values for DSSCs with bougainvillea and mango peel dyes. This means k is regular parameter for all dyes whereas h is regular for bitter gourd dye and irregular for bougainvillea and mango dyes. The parameters are directly proportional to one another.

Table 5. The Saetre and Das model parameter for three DSSCs

Source of natural dye		model parameter	
English Name	Scientific Name	f	g
Bitter gourd	Momordica charantia	2.746442	1.235772
Bougainvillea	Bougainvillea	0.990796	2.897765
Mango peel	Mongifera indica	0.393542	5.133096

In Table 5, the Saetre and Das model parameters f and g are included. Both parameters are positive and therefore they are regular. Also, f and g are inversely proportional. However, the DSSCs with bougainvillea and mango dyes exhibit parameter irregularity in R_{sh} and I_{ph} .

Table 6. The Single diode circuit 5-parameter model for three DSSCs

Source of natural dye		model parameter				
English Name	Scientific Name	A	R_s (W)	R_{sh} (W)	I_o (mA)	I_{ph} (mA)
Bitter gourd	Momordica charantia	0.060353	11.2	189.6	9.6755×10^{-4}	9.7879
Bougainvillea	Bougainvillea	0.229684	35.5	-18.6	2.7823×10^{-3}	-3.1223
Mango peel	Mongifera indica	0.257501	34.6	-99.5	7.1220×10^{-4}	1.6378

In Table 6, the single-diode model parameters ($a, R_s, R_{sh}, I_o,$ and I_{ph}) are included. The DSSC with bitter gourd dye have all the parameters positive and hence they are regular. Similarly, the other DSSCs show parameter irregularity in R_{sh}

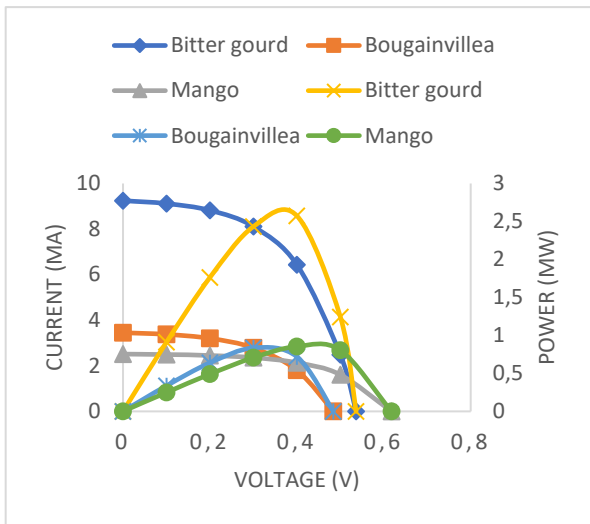
and I_{ph} for DSSC with bougainvillea dye and only R_{sh} for DSSC with mango dye. Also, a and I_{ph} are inversely proportional to R_{sh} and R_s respectively.

Table 7. Some common features of the five models studied

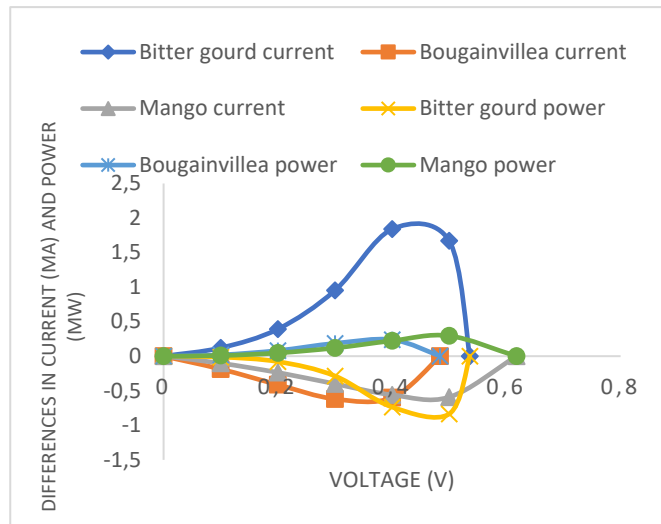
Model	Year	MP	OB	PI	SM ($R_{sh}=\infty$)
El Tayyan	2006	2	6	0	2-parameter model
Karmalkar & Haneefa	2008	3	9	3	3-parameter model
Das	2011	2	6	2	2-parameter model
Saetre and Das	2011	2	6	0	2-parameter model
Shockley single-diode	1949	5	15	3	4-parameter model

Table 7 depicts the 2wnumber of model parameters (MP), observations (OB), parameter irregularities (PI), and simulation model (SM) that produced good curve match for all the DSSCs studied.

In all cases, the model parameters were used in appropriate model equations for the simulation of the DSSCs investigated. In this work, the five-parameter model was used to simulate DSSC with bitter gourd dye with regular parameters whereas the four-parameter model for the remaining DSSCs with irregular parameters yielded good curve fits Figs. (2a-6a) on the left and their corresponding error distributions in Figs.(2b-6b) on the right.



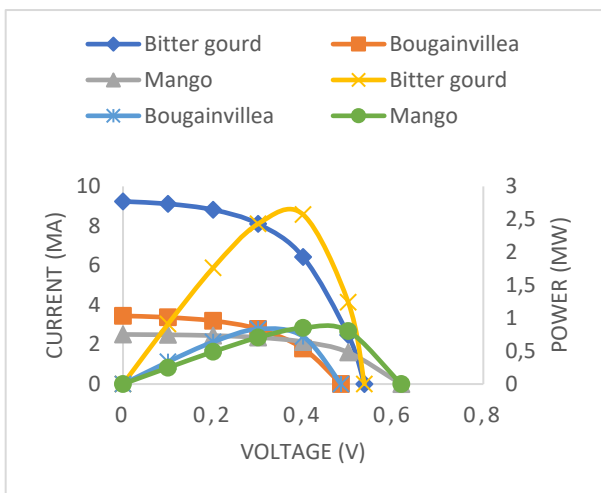
(a) Characteristic I-V/P-V curves



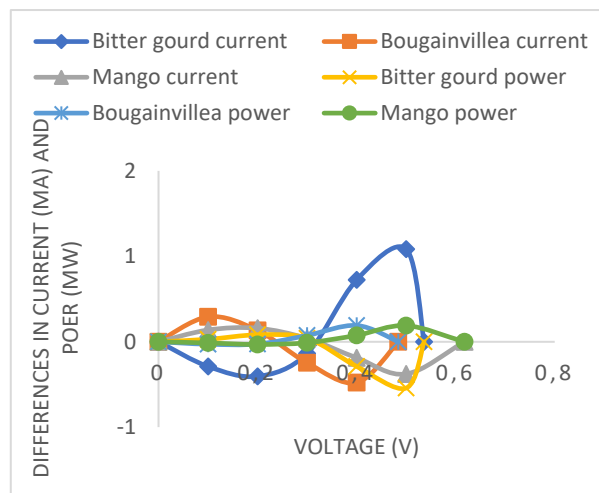
(b) Differences in Current and power

Figure 2. El Tayyan model

(a) characteristic curves and (b) differences between measured and simulated currents and powers



(a) Characteristic I-V/P-V curves



(b) Differences in Current and power

Figure 3. Karmalkar and Haneefa model

(a) characteristic curves and (b) differences between measured and simulated currents and powers

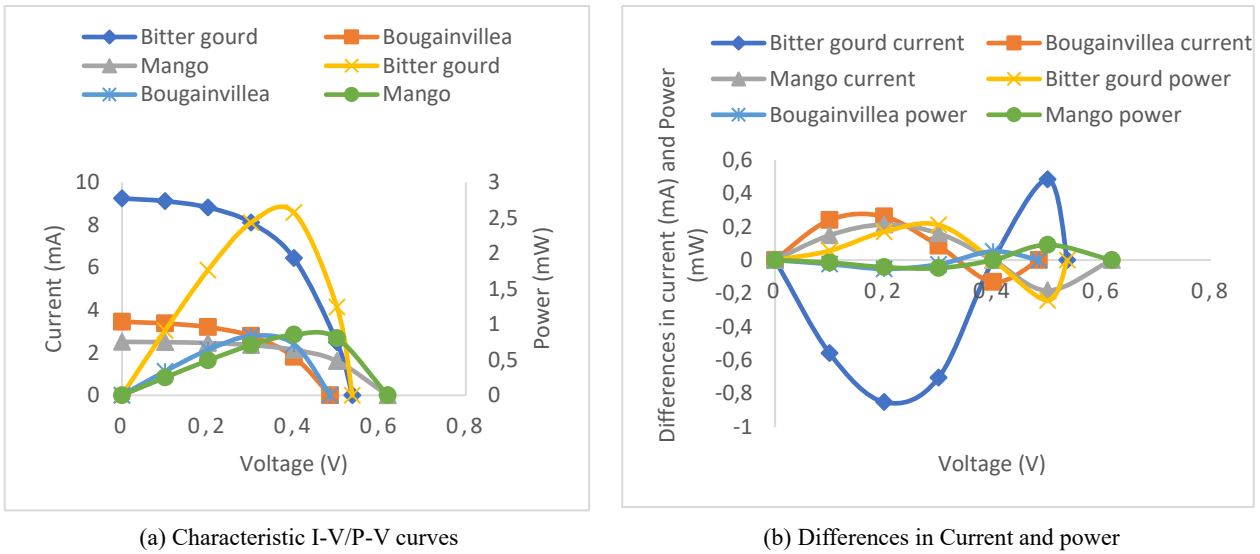


Figure 4. Das model

(a) characteristic curves and (b) differences between measured and simulated currents and powers

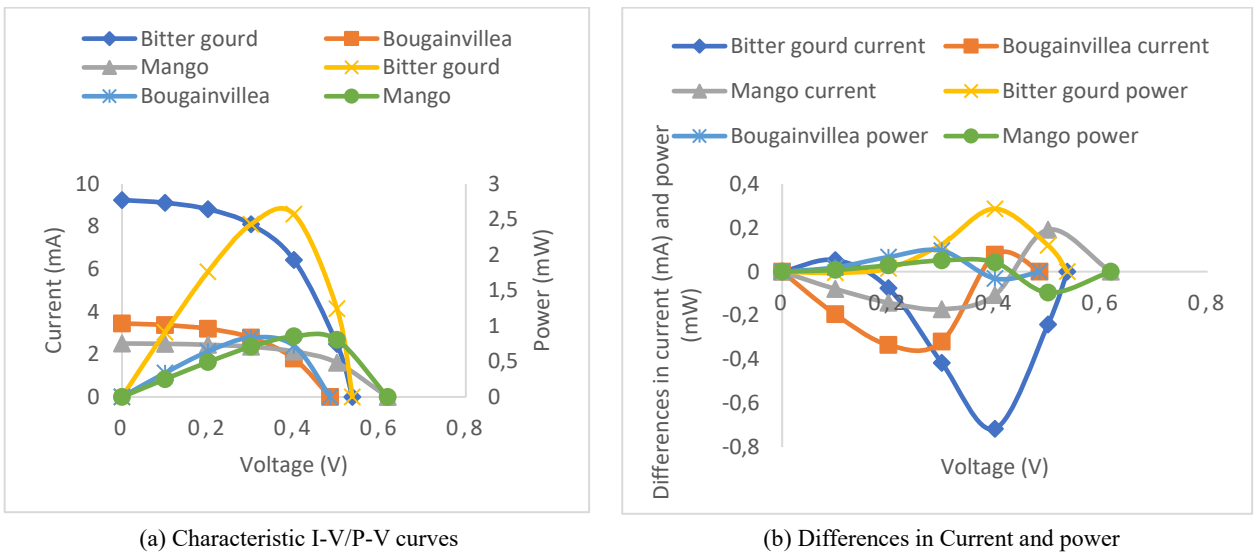


Figure 5. Sactre and Das model

(a) characteristic curves and (b) differences between measured and simulated currents and powers

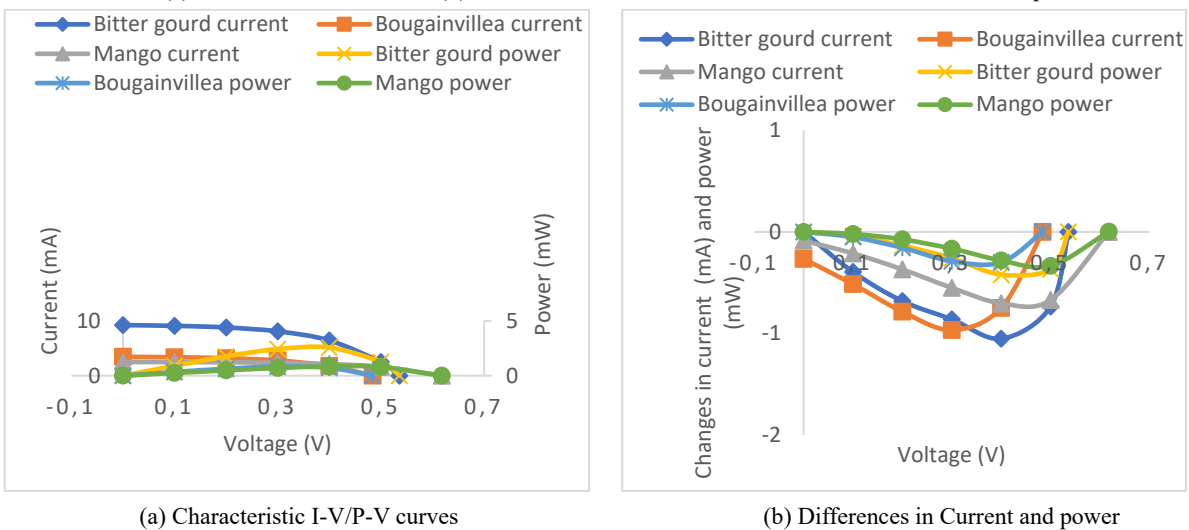


Figure 6. Single-diode model

(a) characteristic curves and (b) differences between measured and simulated currents and powers

CONCLUSIONS

In this study, solutions of five explicit model equations based on the Lambert W-function were used to model and simulate the behavior of three DSSCs. The major conclusions resulting from this work are:

- The input data was the experimental data (short-circuit, maximum power and open circuit) of three DSSCs.
- The nature or sign of model parameters did not affect curve fit for models that neglect resistances (R_s and R_{sh}) as opposed to those depending on the resistances.
- The five-parameter single-diode model relies on resistance with poor curve fit when R_{sh} was negative.
- If n is the number of irregular model parameters, then the model that produced good curve fit is $5-n$ parameter single-diode model i.e., if R_{sh} is neglected we have 4-parameter single-diode model; if R_s and R_{sh} neglected we have 3-parameter single-diode model; etc.
- The single-diode model is more rigorous, time consuming, higher number of model parameters and hence provide more information about the system than the other models.
- The proposed models have provided overall curve fits between the simulated and experimental data.

ORCID IDs

✉ **Jamu Benson Yerima**, <https://orcid.org/0000-0002-8136-3975>; **Dunama William**, <https://orcid.org/0000-0001-9109-8880>

✉ **Alkali Babangida**, <https://orcid.org/0000-0002-3570-0299>; ✉ **Sabastine Chinedu Ezike**, <https://orcid.org/0000-0003-3962-1624>

REFERENCES

- [1] L Hernandez-Callejo, S. Gallardo-Saavedra, and V. Alonso-Gomez, "A review of photovoltaic systems: Design, operation and maintenance", *Sol. Energy*, **188**, 426-440 (2019). <https://doi.org/10.1016/j.solener.2019.06.017>
- [2] P.G.V. Sampaio, and M.O.A. Gonzalez, "The photovoltaic solar energy: conceptual framework", *Renew. Sustainable Energy Rev.* **74**, 590 (2017). <https://doi.org/10.1016/j.rser.2017.02.081>
- [3] M.H. Shubbak, "Advances in solar photovoltaics: Technology review and patent trends", *Renew. Sustainable Energy Rev.* **115**, 109383 (2019). <https://doi.org/10.1016/j.rser.2019.109383>
- [4] A.S. Sarkin, N. Ekren, and S. Saglam, "A review of anti-reflection and self-cleaning coating on photovoltaic panels", *Solar energy*, **199**, 63 (2020). <https://doi.org/10.1016/j.solener.2020.01.084>
- [5] V. Muteri, M. Cellura, D. Curto, V. Franzitta, S. Longo, M. Mistretta, and M.L. Parisi, "Review on life cycle assessment of solar photovoltaic panels", *Energies*, **13**(1), 252 (2020). <https://doi.org/10.3390/en13010252>
- [6] M. Krebs-Moberg, M. Pitz, T.L. Dorsette, and S. H. Gheewala, "Third generation of photovoltaic panels: A life cycle assessment", *Renew. Energy*, **164**, 556 (2021). <https://doi.org/10.1016/j.renene.2020.09.054>
- [7] A.M. Humada, S.Y. Darweesh, K.G. Mohammed, M. Kamil, S.F. Mohammed, N.K. Kasim, T.A. Tahseen, et al, "Modeling of PV system and parameter extraction based on experimental data: Review and investigation", *Sol. Energy*, **199**, 742 (2020). <https://doi.org/10.1016/j.solener.2020.02.068>
- [8] S.M. Sze, *Physics of semiconductor devices*, (Wiley-Interscience, NY, USA, 1969).
- [9] W.G. Pfann, and W. Van Roosbroeck, "Radiative and photovoltaic p-n junction power sources", *J. Appl. Phys.* **25**, (1954). <https://doi.org/10.1063/1.1721579>
- [10] M.B. Prince, "Silicon solar energy converters", *J. Appl. Phys.* Vol. **26**, 534 (1955). <https://doi.org/10.1063/1.1722034>
- [11] M. Wolf, and H. Rauschenbach, "Series resistance on the performance of photovoltaic modules", *Renew. Energy Convers.* **3**, 455 (1963). [http://dx.doi.org/10.1016/0365-1789\(63\)90063-8](http://dx.doi.org/10.1016/0365-1789(63)90063-8)
- [12] E.E. Van Dyk, and E.L. Meyer, "Analysis of the effect of parasitic resistances on the performance of photovoltaic modules", *Renew. Energy*, **29**, 333 (2004). [http://dx.doi.org/10.1016/S0960-1481\(03\)00250-7](http://dx.doi.org/10.1016/S0960-1481(03)00250-7)
- [13] M. De Blas, J. Torres, E. Prieto, and A. Garcia, "Selecting a suitable model for characterizing photovoltaic devices", *Renew. Energy*, **25**, 371 (2002). [https://doi.org/10.1016/S0960-1481\(01\)00056-8](https://doi.org/10.1016/S0960-1481(01)00056-8)
- [14] C. Carrero, J. Rodriguez, D. Ramirez, and C. Platero, "Simple estimation of PV modules loss resistances for low error modeling", *Renew. Energy*, **35**, 1103 (2010). <https://doi.org/10.1016/j.renene.2009.10.025>
- [15] X.-G. Zhu, Z.-H. Fu, and X.-M. Long, "Sensitivity analysis and more accurate solution of photovoltaic solar cell parameters", *Sol. Energy*, **85**, 393 (2011). <https://doi.org/10.1016/j.solener.2010.10.022>
- [16] D.L. Batzner, A. Romeo, H. Zogg, and A.N. Tiwari, CdTe/CdS Solar cell performance under low irradiance, in: *Proceeding of the 17th European photovoltaic solar energy conferences and exhibition*, (WIP-Renewable Energies, Munich, 2001). pp. 1-4.
- [17] K.L. Kennerd, "Analysis of performance degradation in CdS solar cells", *IEEE Trans. Acrosp. Electron Syst.* **AES-5**, 912 (1969). <https://doi.org/10.1109/taes.1969.309966>
- [18] J. Charles, M. Abdelkrim, Y. Muoy, and P. Mialhe, "A practical method of analysis of the current-voltage characteristics of solar cells", *Sol. Cells*, **4**, 169 (1981). [https://doi.org/10.1016/0379-6787\(81\)90067-3](https://doi.org/10.1016/0379-6787(81)90067-3)
- [19] W. De Soto, S.A. Klein, and W.A. Beckman, "Improvement and validation of a model for photovoltaic array performance", *Sol. Energy*, **80**, 78 (2006). <https://doi.org/10.1016/j.solener.2005.06.010>
- [20] C. Carrero, J. Amador, and S. Arnaltes, "A single procedure for helping PV designers to select silicon PV modules and evaluate the loss resistances", *Renew. Energy*, **32**, 2579 (2007). <https://doi.org/10.1016/j.renene.2007.01.001>
- [21] W. Shockley, "The theory of p-n junctions in semiconductors and p-n junction transistors", *Bell syst. Tech. J.* **28**, 435 (1949). <https://doi.org/10.1002/j.1538-7305.1949.tb03645.x>
- [22] J. Cubas, S. Pindado, and M. Victoria, "On the analytical approach for modeling photovoltaic systems behavior", *Power sources*, **247**, 467 (2014). <https://doi.org/10.1016/j.jpowsour.2013.09.008>
- [23] S. Lineykin, M. Averbukh, and A. Kuperman, "Five-parameter model of photovoltaic cell based on STC data and dimensionless", in: *Proceedings of the 2012 IEEE 27th convention of electronical and electronics engineers in Israel*, (Eilat, Israel, 2012). pp. 1-5, <https://doi.org/10.1109/EEEL.2012.6377079>

- [24] L. Peng, Y. Sun, Z. Meng, Y. Wang, and Y. Xu, "A new method for determining the characteristics of solar cells", *J. Power sources*, **227**, 131 (2013). <https://doi.org/10.1016/j.jpowsour.2012.07.061>
- [25] L. Peng, Y. Sun, and Z. Meng, "An improved model and parameters extraction for photovoltaic cells using only three state points at standard test condition", *J. Power Sources*, **248**, 621 (2014). <https://doi.org/10.1016/j.jpowsour.2013.07.058>
- [26] A. Orioli, and A. Di Gangi, "A procedure to calculate the five-parameter model of crystalline silicon photovoltaic modules on the basis of the tabular performance data", *Appl. Energy*, **102**, 1160 (2013). <https://doi.org/10.1016/j.apenergy.2012.06.036>
- [27] J. Ma, K.L. Man, T.O. Ting, N. Zhang, S.-U. Guan, and P.W.H. Wong, "Approximate single-diode photovoltaic model for efficient I-V characteristic estimation", *Sci. World J.* 23047 (2013). <https://doi.org/10.1155/2013/230471>
- [28] J. Ma, K.L. Man, T.O. Ting, N. Zhang, S.-U. Guan, and P.W.H. Wong, "Parameter estimation of photovoltaic models via Cuckoo" Search. *J. appl. Math.* 362619 (2013). <https://doi.org/10.1155/2013/362619>
- [29] Y. Li, W. Huang, H. Huang, C. Hewitt, Y. Chen, G. Fang, and D.L. Carroll, "Evaluation of methods to extract parameters from current-voltage characteristics of solar cells", *Sol. Energy*, **90**, 51 (2013). <https://doi.org/10.1016/j.solener.2012.12.005>
- [30] S.B. Dongue, D. Njomo, J.G. Tamba, L. Ebengai, "Modeling of electrical response of illuminated crystalline photovoltaic modules using four-parameter models", *Int. J. Emerg. Technol. Adv. Eng.* **2**, 612 (2012). https://www.ijetae.com/files/Volume2Issue11/IJETAE_1112_96.pdf
- [31] K. Ishibashi, Y. Kimura, and M. Niwano, "An extensively valid and stable method for derivation of all parameters of a solar cell from a single current-voltage characteristics", *J. appl. Phys.* **103**, (2008). <https://doi.org/10.1063/1.2895396>
- [32] S. Lineykin, M. Averbukh, and A. Kuperman, "An improved approach to extract the single-diode equivalent circuit parameters of a photovoltaic cell/panel", *Renew. Sustain. Energy Rev.* **30**, 282 (2014). <https://doi.org/10.1016/j.rser.2013.10.015>
- [33] D.T. Cotfas, P.A. Cotfas, and S. Kaplanis, "Methods to determine the DC parameters of solar cells: A critical review", *Renew. Sustain. Energy Rev.* **28**, 588 (2013). <https://doi.org/10.1016/j.rser.2013.08.017>
- [34] D.T. Cotfas, P.A. Cotfas, D. Ursutiu, and C. Samoila, D.T. Cotfas, P.A. Cotfas, D. Ursutiu, and C. Samoila, in: *2012 13th International Conference on Optimization of Electrical and Electronic Equipment (OPTIM)*, (Brasso, Romania, 2012), pp. 966-972. <https://doi.org/10.1109/OPTIM.2012.6231814>
- [35] E.I. Batzelis, and S.A. Papatthanassiou, "A method for the analytical extraction of the single-diode PV model parameters", *IEEE Trans. Sustain. Energy*, **7**, 504 (2016). <https://doi.org/10.1109/TSTE.2015.2503435>
- [36] J. Cubas, S. Pindado, and C. de Manuel, "Explicit expressions for solar panel equivalent circuit parameters based on analytical formulation and the Lambert W function", *Energies*, **7**, 4098 (2014). <https://doi.org/10.3390/en7074098>
- [37] G. Petrone, C.A. Ramos-Paja, and G. Spagnuolo, *Photovoltaic sources modeling*, first ed. (Wiley-IEEE Press, Hoboken, NJ, USA, 2017), pp. 208.
- [38] Y. Mahmoud, and E.F. El-Saadany, "Fast power-peaks estimator for partially shaded PV systems", *IEEE. Trans. Energy. Convers.* **31**, 206 (2016). <https://doi.org/10.1109/TEC.2015.2464334>
- [39] S. Pindado, J. Cubas, E. Roibas-Millan, F. Bugallio-Siegel, and F. Sorribes-Palmer, "Assessment of explicit models for different photovoltaic technologies", *Energies*, **11**, 1 (2018). <https://doi.org/10.3390/en11061353>
- [40] M. Oulcaid, H. El Fadil, A.L. Ammeh, A. Yahya, and F. Giri, "One shape parameter-based explicit model for photovoltaic cell and panel", *Sustain. Energy, Grids Networks*, **21**, 100312 (2020). <https://doi.org/10.1016/j.segan.2020.100312>
- [41] A. Et-Tayyan, "An empirical model for generating the IV characteristics for a photovoltaic system", *J. Al-Aqsa Uni.* **10**, 214 (2006). https://www.alaqsa.edu.ps/site_resources/aqsa_magazine/files/225.pdf
- [42] E. Roibas-Millan, J.L. Cubera-Estalarich, A. Gonzalez-Estrada, R. Jado-Peunte, M. Sanabria-Pinzon, D. Alfonso-Corcuera, J.M. Alvarez, J. Cubas, and S. Pindado, "Lamber W-function simplified expressions for photovoltaic current-voltage modeling", in: *2020 IEEE International Conference on Environment and Electrical Engineering and 2020 IEEE Industrial and Commercial Power Systems Europe*, (IEEE, Spain, 2020), pp. 1-6. <https://doi.org/10.1109/EEEIC%2FICPSEUROPE49358.2020.9160734>
- [43] A. Babangida, Doctorate Thesis, Modibbo Adama University Yola (Nigeria), 2022.
- [44] S. Karmalkar, and S. Haneefa, "A physically based explicit J-V model of a solar cell for simple design calculations", *IEEE Electron Device Letters*, **29**(5), 449 (2008). <https://dx.doi.org/10.1109/LED.2008.920466>
- [45] A.K. Das, "An explicit J-V model of a solar cell for simple fill factor calculation", *Sol. Energy*, **85**, 1906 (2011). <https://doi.org/10.1016/j.solener.2011.04.030>
- [46] T.O. Saetre, O.M. Midtgand, and G.H. Yordanov, "A new analytical solar cell I-V curve model", *Renew. Energy*, **36**, 2171 (2011). <https://doi.org/10.1016/j.renene.2011.01.012>

ОЦІНЮВАННЯ ЯВНИХ МОДЕЛЕЙ НА ОСНОВІ W-ФУНКЦІЇ ЛАМБЕРТА ДЛЯ МОДЕЛЮВАННЯ ТА ВІДТВОРЕННЯ РІЗНИХ СЕНСИБІЛІЗОВАНИХ БАРВНИКАМИ СОНЯЧНИХ ЕЛЕМЕНТІВ (DSSC)

Джаму Б. Єріма^a, Дунама Вільям^b, Алкалі Бабангіда^c, Сабастін С. Езіке^a

^aФізичний факультет Університету Модіббо Адама в Йола, Нігерія

^bФакультет математики, Університет Модіббо Адама Йола, Нігерія

^cДепартамент наукової освіти, COE Azare, штат Баучі, Нігерія

У цій статті використовувалися характерні точки як вхідні дані в п'яти різних явних моделях на основі W-функції Ламберта для вилучення параметрів моделі трьох DSSC. Крім того, ці параметри моделі для заданих значень напруг були використані для отримання відповідних струмів для моделювання DSSC. Результати показують, що знак параметра моделі не має значення для методів, які не мають послідовного опору та опору шунта. Однак, коли R_{sh} був від'ємним, 5-параметрична однодіодна модель не дала хорошої відповідності кривої, за винятком випадків, коли нехтували R_{sh} та використовували 4-параметричну модель. Більше того, усі параметри моделі для DSSC з гарбузовим барвником були регулярними та дали хорошу відповідність кривій для всіх моделей. З іншого боку, DSSC з негативними значеннями R_{sh} оброблялися за допомогою чотирипараметричної моделі для отримання хорошої відповідності кривої. Таким чином, знак параметра моделі має значення при моделюванні DSSC з використанням однодіодної моделі.

Ключові слова: параметр моделі, явна модель, W-функція Ламберта, характерні точки, DSSC, підгонка кривої

STUDY OF CIGS PSEUDO-HOMOJUNCTION THIN FILM SOLAR CELL USING SCAPS-1D[†]

✉ Samah Boudour^{a,*}, Idris Bouchama^{b,c}, ✉ Samiha Laidoudi^d, Walid Bedjaoui^{a,e},
Leila Lamiri^a, Ouafia Belgherbi^a, Siham Aziez^f

^aResearch Center in Industrial Technologies CRTI, P.O. Box 64, Cheraga, 16014, Algiers, Algeria

^bElectronic Department, Faculty of Technology, University of M'sila, Algeria

^cResearch Unite on Emerging Materials (RUEM), University Ferhat Abbas, Setif, Algeria

^dUniversité Mohamed El Bachir El Ibrahimi de Bordj Bou Arréridj El-Anasser, 34030, Algérie

^eDepartment of Mechanical Engineering, University of Biskra, B.P.145, 07000, Biskra, Algeria

^fCentre de Recherche Scientifique et Technique en analyse physico-chimique CRAPC

Zone Industrielle lot n°30, Bou Ismail, Tipaza 42415, Algeria

*Corresponding Author: Dr. Samah Boudour, Research Centre in Industrial Technologies CRTI, P.O. Box 64, Cheraga, 16014, Algiers, Algeria. E-mail: s.boudour@crti.dz, boudoursamah@gmail.com

Received August 22, 2022; revised September 9, 2022; accepted September 15, 2022

The present modelling study reports the performance of defected CIGS pseudo-homojunction thin film solar cell (P-HTFSC) and determines its optimum parameters for high performance using the Scaps-1D software under the AM1.5 illumination and the operating temperature of 300 K. To focus the discussion on the optimal parameters (thickness, doping concentrations, deep/interface defect concentrations and bandgap) for the ZnO, CdS, ODC and CIGS thin film layers, cross sectional (1D) simulations have been performed on the ZnO/CdS/ODC/CIGS P-HTFSC device for obtaining its optimal structure that confers high light-into-electricity conversion efficiency. The four light J-V characteristics (short-circuit current: J_{sc} , open-circuit voltage: V_{oc} , fill factor: FF and conversion efficiency: η) have been used as indicators to evaluate the device performances. Simulation outcomes have proved that for a best performance for CIGS P-HTFSC device, the optimal thickness for CIGS and ODC layers should be small than 2 μm and few nm, respectively, while the optimal defect concentration within the layer should be 10^{13} cm^{-3} and between 10^{13} cm^{-3} - 10^{18} cm^{-3} , respectively.

Keywords: CIGS, ODC, Pseudo-homojunction, J-V characteristics, Scaps-1D.

PACS: 02.60.Pn, 85.60.-q, 84.60.Jt, 79.60.Dp, 72.40.+w, 73.63.-b, 68.55.Ln

In recent decades, hiring photovoltaic devices in human being daily life has known an upward trend worldwide; especially in countries that have acquired photovoltaic technology and have use it to solve the problems associated with the dominance of fossil fuels on their growth and to prevent climate change as well. Generally, three generations have been developed and distinguished on the basis of used materials as active layers in photovoltaic device. CIGS, the abbreviation for copper indium gallium selenide materials are considered excellent active layers for the second generation, namely thin film solar cells (TFSC) that take into account the use of small amounts of raw materials that can be easily processed with little of time and energy [1-2]. Regardless of the material composition, the current record efficiency of CIGS thin film solar cell reaches 23.3 % achieved by National Renewable Energy Laboratory (NREL) under AM1.5 spectrum (1000 W/m^2) at temperature of 25° [3]. This record efficiency stays away by more than five-ones from the theoretical limit efficiency of CIGS solar cells that estimated between 28-30% [4]. Such theoretical limit is due to the optimal bandgap of CIGS semiconductor materials that ranges between 1.0-1.7 eV [1-2]. In addition, it was found that, since CIGS materials have high optical absorption coefficient, they absorb light strongly through thin layers not exceeding few (~2) micrometers and thus generate high currents and voltages. At the same time, the few nanometers of the few micrometers of CIGS layer at n-buffer/p-CIGS interface are highly defected region because of the Cu leakage towards the CIGS material and thus this part of the CIGS transforms from p-type to n-type and is named by the Ordered-Defect-Compound (ODC) part and, for example, is a compound of CuIn_3Se_5 or CuIn_5Se_8 or $\text{Cu}_2\text{In}_4\text{Se}_7$, etc [1,2]. Therefore, the junction formed between the ODC layer and the CIGS layer is an accidental junction that occurs during the fabrication process and is named the ODC/CIGS pseudo-homojunction. To study the impact of the work function on the overall performance of the superstrate CIGS TFSC, Bouchama et al. [5] inserted a significant n-type ODC layer between the In_2Se_3 and CIGS layers. At the end of the study, they obtained an outstanding efficiency of 20.18%. When photovoltaic community looks at the diversity of features that distinguish the CIGS material among others, they discover that CIGS still needs to more development to make the performance of CIGS solar cells more perfect and challenging to other photovoltaic devices in terms of large-scale manufacturing. Therefore, they have used software tools (AMPS-1D [5], SILVACO-TCAD [6], etc) that were developed in parallel with the development of solar cell devices to facilitate and streamline the manufacturing procedure.

The present article targets and analyses the light-to-electricity conversion performance of ZnO/CdS/ODC/CIGS pseudo-homojunction thin film solar cell (P-HTFSC) using a computer simulator named Solar Cell Capacitance Simulator (Scaps-1D) [7]. This leads to assess the performance of targeted device through the current density-voltage

[†] Cite as: S. Boudour, I. Bouchama, S. Laidoudi, W. Bedjaoui, L. Lamiri, O. Belgherbi, and S. Aziez, East Eur. J. Phys. 4, 145 (2022), <https://doi.org/10.26565/2312-4334-2022-4-14>

© S. Boudour, I. Bouchama, S. Laidoudi, W. Bedjaoui, L. Lamiri, O. Belgherbi, S. Aziez, 2022

(J-V) characteristics, which consisted of short-circuit current (J_{sc}), open-circuit voltage (V_{oc}), fill factor (FF) and power conversion efficiency (η), against input settings, which includes the thickness, acceptor/donor concentration, interface/bulk defect and band gap of different device layers (ZnO or CdS or ODC or CIGS). As a result, the outcome of this study may be an optimized device that ensures to achieve the highly efficiency/cost ratio.

DEVICE AND SIMULATION TOOL

The following Figure 1(a) schemes the structure of the CIGS P-HTFSC, which is composed from the top to the bottom of: an aluminium (Al) metal fingers as an ohmic contact from the front side of the device; a zinc oxide (ZnO) thin film as a transparent conducting oxide (TCO) window layer; a cadmium sulphide (CdS) thin film as a buffer layer; an ordered defect compounds (ODC) layer, a copper indium gallium selenide (CIGS) thin film as an absorber layer; a molybdenum (Mo) metal as an ohmic back contact coated on the glass substrate.

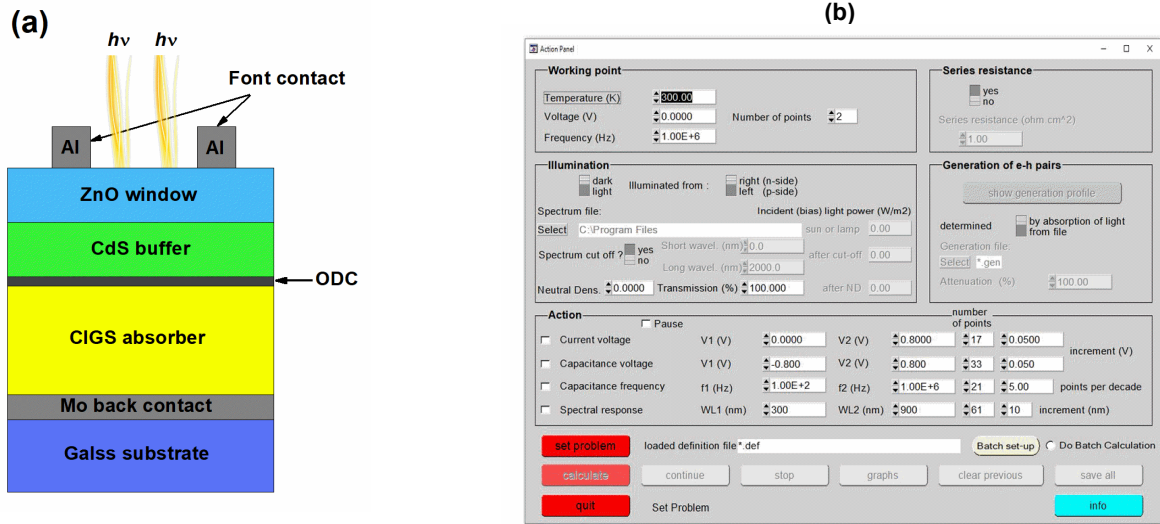


Figure 1. (a) Scheme of CIGS P-HTFSC Structure & (b) Scaps-1D graphical interface

In order to better address and analyse the light-to-electricity conversion efficiency of targeted device presented by Figure 1(a), Scaps-1D will be used as simulator tool [7]. This simulating tool resolves the dipolar problems in one dimension across layers of semiconducting devices by governing the equations of Poisson and electron/hole continuity. Moreover, it is featured by an easy graphical interface, as shown in Figure 1(b) that allows inputting and varying, either individually or collectively, the different properties of each layer, for example, thickness, bandgap energy, and donor/acceptor/defect concentrations. In addition, SCAPS-1D is equipped by different solar irradiation spectra, for example, the AM1.5 spectrum which will be used to radiate an incident power of 100mW/cm² towards the targeted device, while the reflection will be ignored during all simulation processes, meanwhile the operating temperature will be in contrast fixed at 300 K. While, each row in the Table 1 represents electrical and optical settings for a semiconducting layer in the proposed device shown in Figure 1(a), Table 2 represents the defect settings for CIGS layer.

Table 1. Settings for ZnO, CdS and CIGS layers used in SCAPS-1D simulation

Parameter	Symbol (unit)	ZnO	CdS	CIGS
Thickness	w (μm)	0.01 ~ 0.3	0.04 ~ 1	0.2 ~ 15
Dielectric constant	ϵ/ϵ_0	10	10	10
Electron affinity	χ_e (eV)	4.6	4.3	4.5
Electron mobility	μ_n ($\text{cm}^2\text{V}^{-1}\text{s}^{-1}$)	100	100	100
Hole mobility	μ_p ($\text{cm}^2\text{V}^{-1}\text{s}^{-1}$)	25	25	25
Bandgap	E_g (eV)	3.3	2.45	1.01 ~ 1.56
Donor / Acceptor concentration	N_d / N_a (cm^{-3})	$10^{12} \sim 4 \times 10^{21}$	$10^{12} \sim 4 \times 10^{21}$	$10^{12} \sim 10^{22}$
Effective density of states in CB	N_c (cm^{-3})	4×10^{18}	2×10^{18}	2×10^{18}
Effective density of states in VB	N_v (cm^{-3})	9×10^{18}	1.5×10^{19}	2×10^{18}

Table 2. Defect settings for CIGS absorber layer

Parameter	Symbol (unit)	Value
Defect density	N_t (cm^{-3})	1×10^{13}
Standard deviation	(eV)	0.1
Electron cross-section	(cm^2)	5.3×10^{-13}
Hole cross-section	(cm^2)	5×10^{-15}

RESULTS AND DISCUSSION
Optimal Thickness of CIGS Absorber Layer

The photovoltaic community has long sought an increased focus on thin film technology, which fulfils the criterions of high photon absorption and low quantity materials to improve the cost-efficiency ratio of the solar cell devices. Based on this approach, Figure 2 summarizes the evolution of J-V characteristics against the change in thickness of the CIGS absorber layer from 0.2 μm to 15 μm, starting with small steps of 0.2 μm to 0.5 μm to 1 μm as the CIGS layer thickness is increased; the important thing is that sharp increase was observed at first 2 μm of thickness in both J_{SC} , V_{OC} , FF and efficiency (η), which take almost unchanged value along the remaining 13 μm.

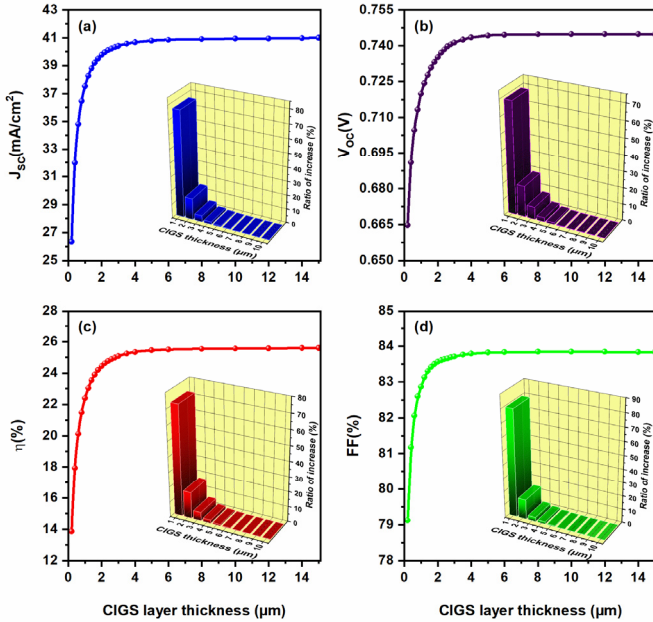


Figure 2. J-V characteristics versus thickness of CIGS absorber layer

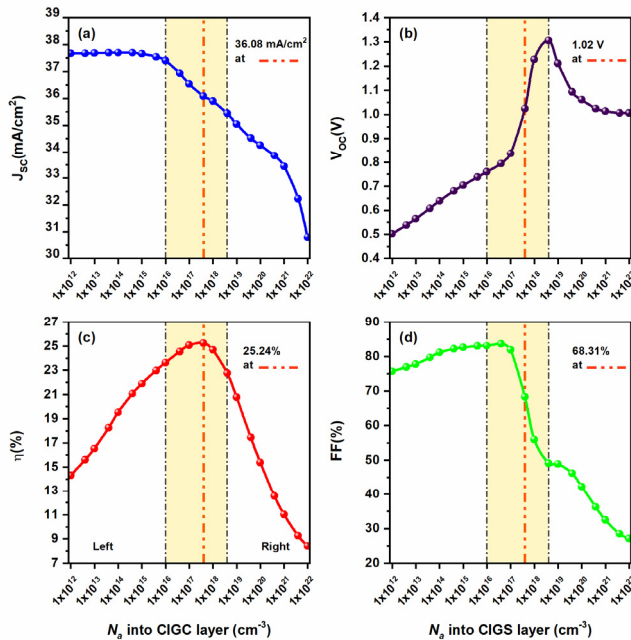


Figure 3 J-V characteristics versus acceptor concentration N_a into CIGS absorber layer

(at $N_a = 4 \times 10^{17} \text{ cm}^{-3}$ in Figure 3) due to the deterioration of the V_{OC} at lower acceptor concentration (left of N_a) and the deterioration of both J_{SC} , V_{OC} and FF at higher acceptor concentration (right of N_a). The deterioration of the V_{OC} at

Hence, at 2 μm, both J_{SC} , V_{OC} , FF and efficiency achieved 39.75 mA/cm², 0.73 V, 83.56 %, and 24.43 %, respectively, while at 15 μm they achieved 40.98 mA/cm², 0.74 V, 83.83 %, and 25.59 %, respectively. As a result, the convergence of the obtained values of J-V characteristics at 2 μm and 15 μm emphasized that a few μm of CIGS layer are sufficient for an absorber layer in a solar cell device to absorb the penetrating photons to the fullest. This was also supported by the included inset histograms in Figure 2, which emphasized that an approximately 2 μm of CIGS thin layer is necessary and sufficient to perform best cost-efficiency ratio. This sufficiency at 2 μm thickness is due to the high absorption coefficient (10^5 cm^{-1}) of CIGS material in the fundamental region of solar spectrum [8], where the absorbed energy of photons is responsible to generate hole-electron pairs, which will be separated by the space charge region (SCR) that is formed due to the metallurgical junction between parts of p-CIGS layer and n-CdS layer. Subsequently, the CIGS layer offers the bulk which through it will journey the separated holes to the back contact (Mo), while the electrons will journey through the buffer (CdS) to the window (ZnO) to the front contact (Al). The performed simulations subject to the conditions listed in Table 1 and 2 have proved that the extravagance of using 15 μm of the CIGS material for absorber layer will rise the manufacturing cost compared to the improvements it can achieve in the performance of the solar cell device, and sufficiency of using 2 μm or a little less of a CIGS absorber layer gives to ZnO/CdS/ODC/CIGS P-HTFSC the ability to perform an efficiency of about 24.43%.

Optimal Acceptor Concentration into CIGS Absorber Layer

Figure 3 summarizes the evolution of J-V characteristics against the change in acceptor concentration (N_a) within CIGS absorber layer from 10^{12} cm^{-3} to 10^{22} cm^{-3} ; the important thing is that the efficiency reaches its maximum value of 25.24% at $4 \times 10^{17} \text{ cm}^{-3}$ of acceptor concentrations into CIGS absorber layer that it was coincided with the achievements of 36.08 mA/cm², 1.02 V and 68.31% for both J_{SC} , V_{OC} and FF, respectively, as shown by the intersections of the dashed orange lines with the curves in Figure 3. However, the efficiency experienced weak or deteriorated behaviour on the right and left of the orange dashed line

higher acceptor concentration is due to an increase in recombination rate at rear surface of CIGS absorber layer. While the highly J_{SC} at low acceptor concentration is induced by the high carrier mobility and high carrier life time, which induce good collection of the photo-generated carriers, the drop of the J_{SC} at higher acceptor concentration is attributed to the increase of recombination rate of the photo-generated charge carriers that takes place within the CIGS bulk. As a result, in order to obtain best performance in term of efficiency (25.24%) for ZnO/CdS/ODC/CIGS P-HTFSC, the optimum acceptor concentration within CIGS absorber layer should be around $N_a = 4 \times 10^{17} \text{ cm}^{-3}$, which is slightly larger than what was mentioned by the experimental studies in both Lee et al [9] and Yüksel et al [10].

Optimal Bandgap of CIGS Absorber Layer

$\text{CuIn}_{1-x}\text{Ga}_x\text{Se}_2$ (CIGS: copper, indium, gallium and diselenide) materials are I-III-VI semiconducting alloys that mutate from CuInSe_2 (CIS: $x=0$) alloy to CuGaSe_2 (CGS: $x=1$) alloy according to x value ($0 \sim 1$) of Ga, as documented in Table 3.

Table 3. CIGS alloys and their bandgap energies

x concentration	Bandgap energy, E_g (eV)	$\text{CuIn}_x\text{Ga}_{1-x}\text{Se}_2$
$x = 0$	1.01	CuGaSe_2
$x = 0.31$	1.176	$\text{CuIn}_{0.31}\text{Ga}_{0.69}\text{Se}_2$
$x = 0.45$	1.260	$\text{CuIn}_{0.45}\text{Ga}_{0.55}\text{Se}_2$
$x = 0.66$	1.398	$\text{CuIn}_{0.66}\text{Ga}_{0.34}\text{Se}_2$
$x = 1$	1.65	CuInSe_2

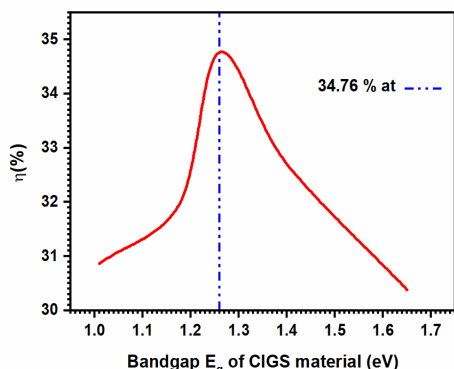


Figure 4. Efficiency (η) for ZnO/CdS/ODC/CIGS P-HTFSC versus bandgap (E_g) of CIGS material

This wide range of x value means that the CIGS alloys can be tuned in terms of stability and miscibility of the embedded materials, therefore, tuning the optical bandgap energy (E_g) of CIGS alloys over a wide range (1.01 eV \sim 1.65 eV) is possible and sometimes even demanded (see Table 3). As mentioned in the literature, the bandgap of CIGS material is a direct optical feature, which allows to strongly absorbing the photons of fundamental range of the solar spectrum [4].

Figure 4 summarizes the evolution of power conversion efficiency (η) for ZnO/CdS/ODC/CIGS TFSC against the change in bandgap energy of CIGS absorber layer from 1.01 eV to 1.65 eV; the important thing is that the efficiency reaches its maximum value of 34.76% at 1.26 eV of bandgap energy as shown by the intersection of the dashed blue line with the curve in Figure 4. As a result, in order to obtain best performance in term of efficiency (34.76%) for ZnO/CdS/ODC/CIGS P-HTFSC, the optimum bandgap energy for CIGS absorber layer should be around 1.26 eV, which corresponds the x of 0.45 for Ga content.

Optimal Thickness of CdS Buffer Layer

Figure 5 summarizes the evolution of JV characteristics against the change in the thickness of the CdS buffer layer from 40 nm to 1 μm starting with small steps of 20 nm (at first 80 nm) to 50 nm as the CdS layer thickness is increased; the important thing is that while the performances in both J_{SC} , V_{OC} , FF and efficiency were low or deteriorated at thicknesses less than 80 nm and more than 100 nm, they were excellent and even improvements were achieved at thicknesses over 80 nm and less than 100 nm, as shown by the curves outlined in the yellow areas in Figure 5.

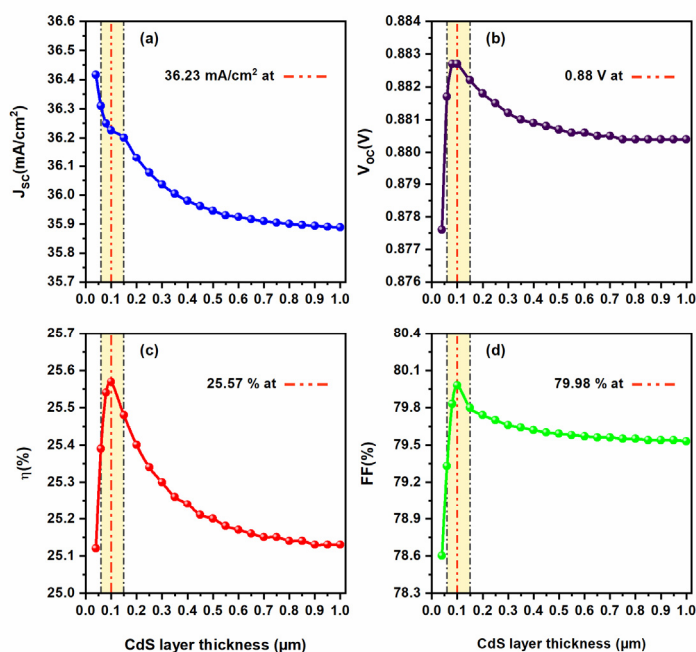


Figure 5. J-V characteristics versus thickness of CdS buffer layer

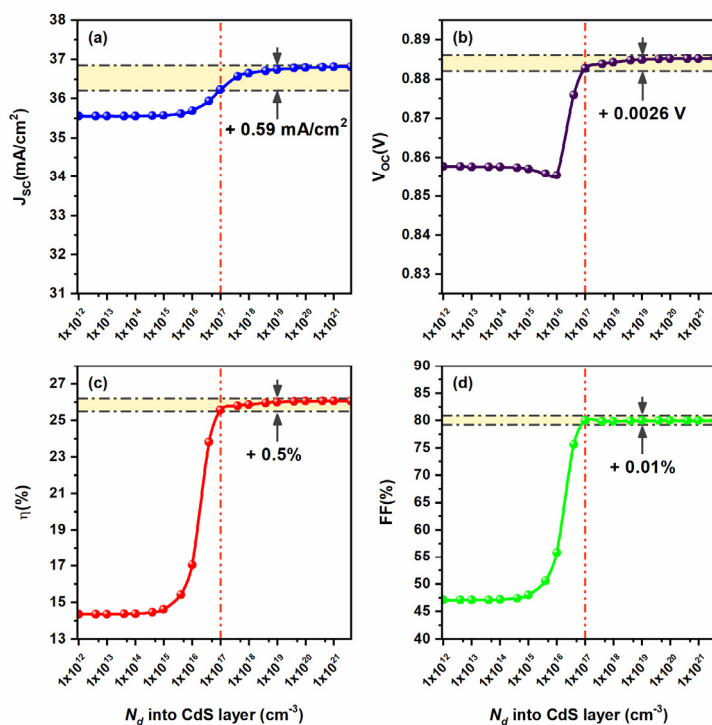


Figure 6. J-V characteristics versus donor concentration N_d into CdS buffer layer

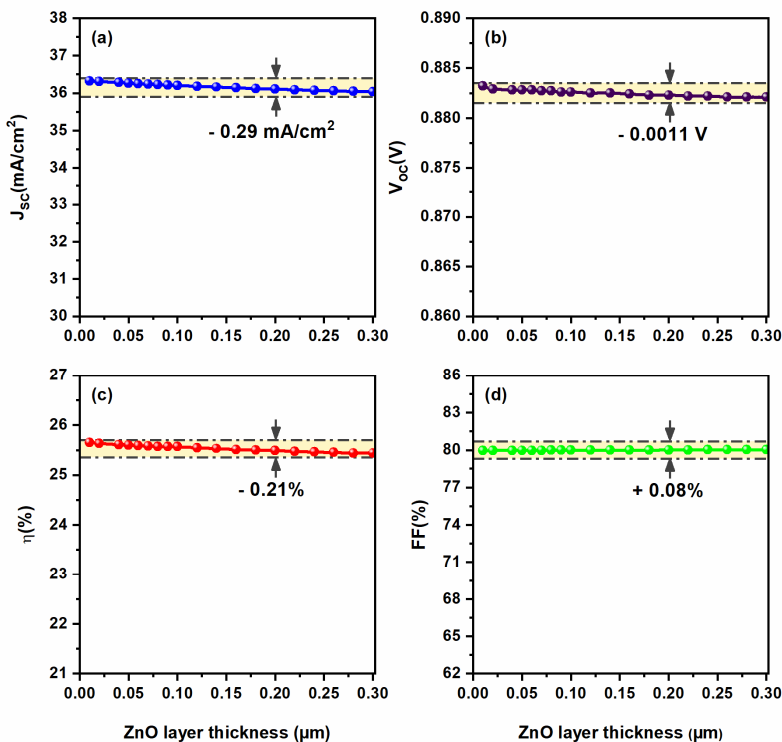


Figure 7. J-V characteristics versus thickness of ZnO window layer

Optimal Thickness of ZnO

Window Layer. Figure 7 summarizes the evolution of JV characteristics against the change in the thickness of the ZnO window layer from 10 nm to 300 nm starting with small steps of 10 nm to 20 nm as the ZnO layer thickness is increased; the important thing is that there was no significant change in all J-V characteristics performances, as shown

While the poor efficiency of CIGS solar cell with a CdS buffer layer of some only tens of nanometres thick (<80 nm) is due to V_{OC} and FF deteriorations, which are attributed to the low bandgap of CdS material that cause an excessive absorption of photons in the blue wavelength range [11], the poor efficiency of CIGS solar cell with a CdS buffer layer of thickness over than 100 nm is due to J_{SC} , V_{OC} and FF deteriorations, which are attributed to the high recombination rate of charge carrier during its journey through CdS buffer layer. As a result, a sufficiency of using 100 nm or a little less of a CdS buffer layer gives to ZnO/CdS/ODC/CIGS P-HTFSC the ability to perform high J_{SC} , V_{OS} , FF and efficiency of 36.23 mA/cm², 0.88 V, 79.98 % and 25.57 %, respectively.

Optimal Donor Concentration into CdS Buffer Layer

Figure 6 summarizes the evolution of J-V characteristics against the change in donor concentration (N_d) within CdS buffer layer from 1×10^{12} cm⁻³ to 4×10^{21} cm⁻³; the important thing is that the efficiency reaches its optimum value of 25.57% at 1×10^{17} cm⁻³ of donor concentration into CdS buffer layer that it was coincided with the achievements of 36.23 mA/cm², 0.88 V and 79.98% for both J_{SC} , V_{OC} and FF, respectively, as depicted by the intersections of the dashed orange lines with the curves shown in Figure 6. The sharp increase in all J-V characteristics at 1×10^{17} cm⁻³ of donor concentration is attributed to increase in collection rate of minority carrier charge. The slight increases of 0.59 mA/cm², 2.6 mV, 0.01% and 0.5% in both J_{SC} , V_{OC} , FF and efficiency, respectively, despite the big jump in donor concentration from 1×10^{17} cm⁻³ to 4×10^{21} cm⁻³ confirm that the 1×10^{17} cm⁻³ concentration is the optimum donor concentration for CdS material to be a highly performant buffer layer for the ZnO/CdS/ODC/CIGS P-HTFSC. This optimized concentration means that the CdS buffer layer do not need to reaches its effective density of states (2×10^{18} cm⁻³) to do best performance.

by the curves outlined in the yellow areas in Figure 7, where small decreases of 0.29 mA/cm², 1.1 mV, 0.08% and 0.21% were recorded in both J_{SC}, V_{OS}, FF and efficiency, respectively.

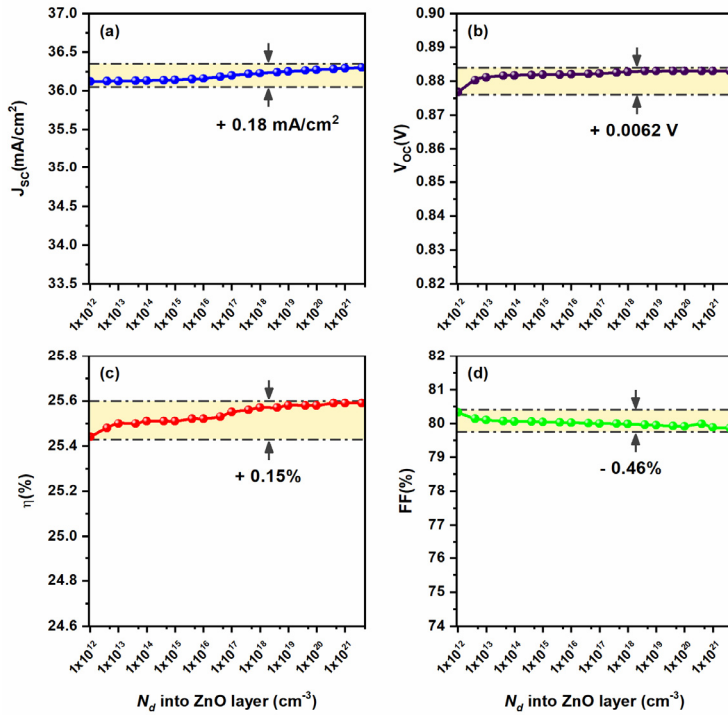


Figure 8. J-V characteristics versus donor concentration N_d into ZnO window layer

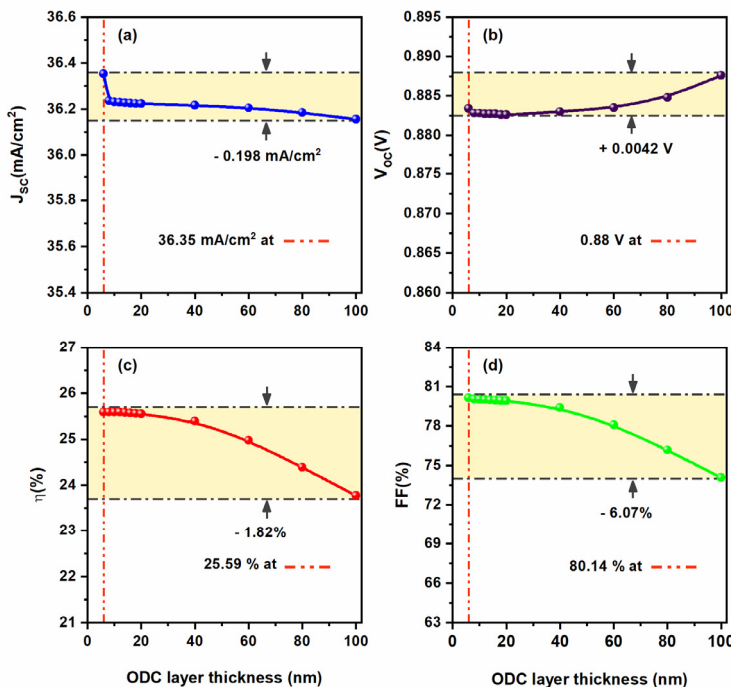


Figure 9. J-V characteristics versus thickness of ODC layer

This slight decrease is attributed to the wide optical bandgap (3.3 eV) of the ZnO material that prevents the absorption of photons that have less energy than their bandgap. As a result, a sufficiency of using few manometers of a ZnO layer gives to ZnO/CdS/ODC/CIGS P-HTFSC the ability to perform high J_{SC}, V_{OS}, FF and efficiency of about 36.32 mA/cm², 0.88 V, 80% and 25.65%, respectively.

Optimal Donor Concentration into ZnO Window Layer

Figure 8 summarizes the evolution of J-V characteristics against the change in donor concentration (N_d) within ZnO window layer from 1×10^{12} cm⁻³ to 4×10^{21} cm⁻³; the important thing is that there was slight changes of +0.18 mA/cm², +6.2 mV, -0.46% and +0.15% in both J_{SC}, V_{OC}, FF and efficiency, respectively, despite the high increase in donor concentration within ZnO window layer. Based on what summarized in Figure 8 that both J_{SC}, V_{OC}, FF and efficiency achieved 36.25 mA/cm², 0.88 V, 79.94%, 25.58%, respectively, at 10^{19} cm⁻³ of donor concentration and based on what is mentioned in the literature that the elaborated ZnO thin films are semiconductors with stoichiometry controlled carrier concentration ranging from 10^{16} cm⁻³ to 10^{21} cm⁻³ [12], the 10^{19} cm⁻³ is the optimum donor concentration within ZnO window layer that gives the best performance for ZnO/CdS/ODC/CIGS P-HTFSC.

Optimal Thickness of ODC Layer

While Section (3.1.) has studied the effect of the overall thickness of the CIGS material used inside the solar cell structure, this section will study the effect of the last few nanometres of the CIGS layer near the CdS/CIGS interface side. Figure 9 summarizes the evolution of J-V characteristics against the change in thickness of ODC layer from 6 nm to 100 nm; the important thing is that there were small changes of +0.198 mA/cm², +4.2 mV, -6.07% and -1.82% in both J_{SC}, V_{OC}, FF and efficiency, respectively. The negative changes in J_{SC} and hence efficiency (Figure 9) is may be due to the

increase in recombination rate at the CIGS/CdS interface due to the inadequacy of passivation effect of the ODC layer.

Study of Defects in CIGS Pseudo-Homojunction Structure

Effect of defect Concentration into CIGS Absorber Layer. Figure 10 summarizes the evolution of J-V characteristics against the change in defect concentration N_i into CIGS absorber layer from the concentration

10^{13} cm^{-3} to the concentration $4 \times 10^{17} \text{ cm}^{-3}$, which represents the optimum acceptor concentration for the CIGS pseudo-homojunction cell; the important thing is that the efficiency achieved its maximum value of 25.57% at 10^{13} cm^{-3} of defect concentration into CIGS absorber layer that it was coincided with the achievements of 36.23 mA/cm², 0.88 V and 79.98% for both J_{SC} , V_{OC} and FF, respectively. However, both J_{SC} , V_{OC} , FF and efficiency began to deteriorate once the defect concentration began to decrease, reaching their lowest levels of 9.57 mA/cm², 0.53 V, 43.37% and 2.19%, respectively, once the defect concentration reaches $4 \times 10^{17} \text{ cm}^{-3}$. This J-V deterioration behaviour is attributed to the reduction in generated carrier journeying through the bulk of the CIGS absorber layer because of the high defect concentration within it, which means that for the CIGS pseudo-homojunction cell to perform well, the defect concentration must be lowered to 10^{13} cm^{-3} .

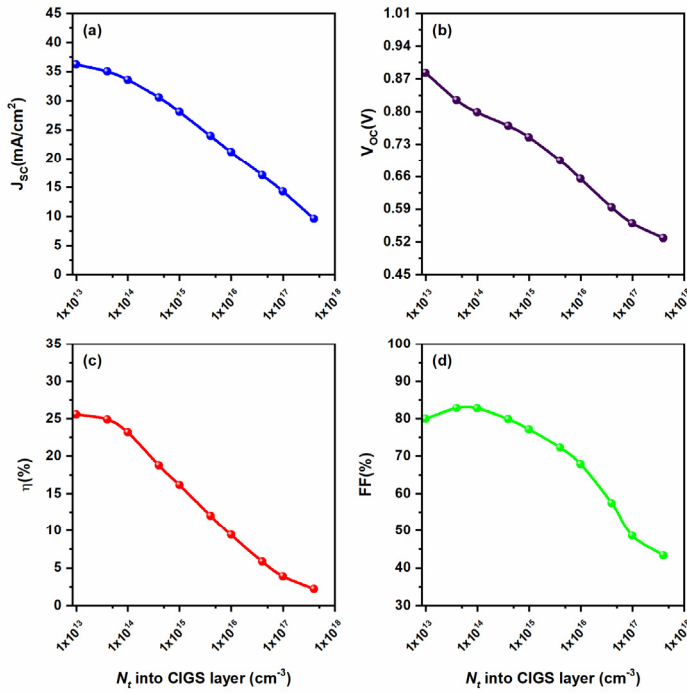


Figure 10. J-V characteristics versus defect concentration N_t into CIGS absorber layer

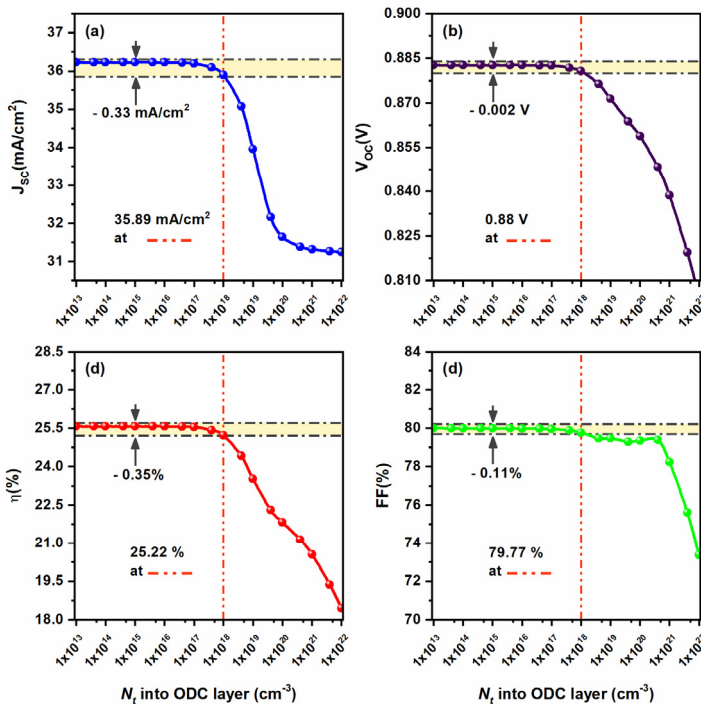


Figure 11. J-V characteristics versus defect concentration N_t into ODC layer

Effect of defect concentration into ODC Layer.

Figure 11 summarizes the evolution of J-V characteristics against the change in defect concentration N_t within ODC layer from 10^{13} cm^{-3} to 10^{22} cm^{-3} ; the important thing is that while increasing defect concentration from 10^{13} cm^{-3} to 10^{18} cm^{-3} there was slight decreases of 0.33 mA/cm², 2 mV, 0.11% and 0.35% in both J_{SC} , V_{OC} , FF and efficiency, respectively. After achieving considerable values of 35.89 mA/cm², 0.88 V, 79.77% and 25.22% (Figure 11) in both J_{sc} , V_{oc} , FF and efficiency, respectively, at defect concentration of 10^{18} cm^{-3} , all characteristics experienced deterioration down to their minimum values 10^{22} cm^{-3} of defect concentration. As a result, limiting the defect concentration 10^{13} cm^{-3} to 10^{18} cm^{-3} within the ODC layer leads the ZnO/CdS/ODC/CIGS P-HTFSC device to the best performance.

CONCLUSIONS

Through the present simulation study, the feasibility of CIGS material for thin film solar cell device has been investigated through numerical simulation using Scaps-1D software. CdS/CIGS heterojunction and ODC/CIGS pseudo-homojunction have been systematically investigated, and the influences of bandgap, thickness, carrier concentration, defect concentration and the performance of layers within the ZnO/CdS/ODC/CIGS P-HTFSC device have been discussed in more details. It was found that for a CdS/CIGS heterojunction, an efficiency of 25.57% can be obtained, with a CIGS layer at $4 \times 10^{17} \text{ cm}^{-3}$ of acceptor concentrations, 10^{13} cm^{-3} of defect concentration and 2 μm of thickness. And if an ODC layer is considered at the CdS/CIGS interface to form a new ODC/CIGS pseudo-homojunction, an efficiency of 25.22% can be obtained, with an ODC layer of 10^{13} - 10^{18} cm^{-3} of defect concentration and 100 nm of thickness. These results-out performances are very promising for further improvements for CIGS thin film solar cell.

ORCID IDs

Samah Boudour, <https://orcid.org/0000-0002-4277-6945>; Samiha Laidoudi, <https://orcid.org/0000-0002-3566-9359>

Credit author statement. Samah Boudour: Conceptualization, Methodology, Data curation, Original draft preparation Writing, Editing. Idris Bouchama: Data curation, Editing, Supervision.

Acknowledgments

The authors show recognition to the scientists, at the Department of Electronics and Information Systems (ELIS) of the University of Gent, Belgium, that developed the freely SCAPS-1D simulator.

REFERENCES

- [1] S.R. Kodigala, Chapter 5 - Optical Properties of I–III–VI₂ Compounds, Thin Films and Nanostructures, **35**, 195 (2010). <https://doi.org/10.1016/B978-0-12-373697-0.00005-5>
- [2] N. Khoshsirat, and N.A.M. Yunus, in: *Nanoelectronics and Materials Development*, edited by K. Abhijit, (InTechOpen, 2016), pp. 41-65.
- [3] M.A. Green, E.D. Dunlop, J. Hohl-Ebinger, M. Yoshita, N. Kopidakis, and X.J. Hao, “Solar cell efficiency tables (Version 59)”, *Prog. Photovolt. Res. Appl.* **30**, 3 (2022). <http://dx.doi.org/10.1002/pip.3506>
- [4] L.A. Kosyachenko, in: *Solar Cells: New Approaches and Reviews*, edited by J. Fagerberg, D.C. Mowery, and R.R. Nelson, (IntechOpen, 2015). <https://doi.org/10.5772/58490>
- [5] I. Bouchama, S. Boudour, N. Bouarissa, and Z. Rouabah, “Quantum and conversion efficiencies optimization of superstrate CIGS thin-films solar cells using In₂Se₃ buffer layer”, *Optical Materials*, **72**, 177 (2017). <http://dx.doi.org/10.1016/j.optmat.2017.05.056>
- [6] A. Bakoura, A. Saadoun, I. Bouchama, F. Dhiabi, S. Boudour, and M.A. Saeede, “Effect and optimization of ZnO layer on the performance of GaInP/GaAs tandem solar cell”, *Micro and Nanostructures*, **168**, 207294 (2022). <https://doi.org/10.1016/j.micrna.2022.207294>
- [7] M. Burgelman, K. Decock, A. Niemegeers, J. Verschraegen, and S. Degraeve, *SCAPS manual, Version 2021*, (University of Gent, Belgium).
- [8] Y. Osman, M. Fedawy, M. Abaza, M.H. Aly, “Optimized CIGS based solar cell towards an efficient solar cell: impact of layers thickness and doping”, *Optical and Quantum Electronics*, **53**, 245 (2021). <https://doi.org/10.1007/s11082-021-02873-4>
- [9] J.W. Lee, J.D. Cohen, and W.N. Shafarman, “The determination of carrier mobilities in CIGS photovoltaic devices using high-frequency admittance measurements”, *Thin Solid Films*, **480**, 336 (2005). <https://doi.org/10.1016/j.tsf.2004.11.087>
- [10] Ö.F. Yüksel, B.M. Başol, H. Şafak, and H. Karabiyik, “Optical characterisation of CuInSe₂ thin films prepared by two-stage process”, *Appl. Phys. A*, **73**, 387 (2001). <https://doi.org/10.1007/s003390100744>
- [11] J.R. Lakowicz, I. Gryczynski, Z. Gryczynski, and C.J. Murphy, “Luminescence Spectral Properties of CdS Nanoparticles”, *J. Phys. Chem. B*, **103**(36), 7613 (1999). <https://doi.org/10.1021/jp991469n>
- [12] S. Emin, S. P. Singh, L. Han, N. Satoh, and A. Islam, “Colloidal quantum dot solar cells”, *Sol. Energy*, **85**, 1264 (2011). <https://doi.org/10.1016/j.solener.2011.02.005>

ДОСЛІДЖЕННЯ ПСЕВДОГОМОПЕРЕХОДУ CIGS ТОНКОПЛІВКОВОГО СОЛЯЧНОГО ЕЛЕМЕНТА З ВИКОРИСТАННЯМ SCAPS-1D

Самах Будур^a, Ідріс Бучама^{b,c}, Саміха Лайдуді^d, Валід Беджауї^e, Лейла Ламірі^a, Уафія Белгербі^a, Сіхам Азіз^f

^aНауково-дослідний центр промислових технологій CRTI, Р.О. Вох 64, Черага, 16014, Алжир

^bЕлектронний факультет, технологічний факультет, Університет Мсіла, Алжир

^cДослідницький відділ нових матеріалів (RUEM), Університет Ферхата Аббаса, Сетіф, Алжир

^dУніверситет Мохамед Ель Башир, Ель Ібрахімі Бордж-Бу Аррерідж Ель-Анассер, 34030, Алжир

^eФакультет машинобудування, Університет Біскри, В.Р.145, 07000, Біскра, Алжир

^fНауково-технічний дослідницький центр фізико-хімічного аналізу CRAPC
промислова зона, лот №30, Бу-Ісмаїл, Тупаза 42415, Алжир

У цьому дослідженні повідомляється про моделювання продуктивності пошкодженої псевдогетероструктурної тонкоплівкової сонячної батареї CIGS (P-HTFSC) і визначаються її оптимальні параметри для високої продуктивності за допомогою програмного забезпечення SCAPS-1D при освітленні AM1.5 і робочій температурі 300 К. Щоб зосередити дискусію на оптимальних параметрах (товщині, концентраціях легування, концентраціях дефектів на глибині/інтерфейсі та ширині забороненої зони) для тонкоплівкових шарів ZnO, CdS, ODC та CIGS, було виконано моделювання поперечного перерізу (1D) на ZnO/CdS/ Пристрій ODC/CIGS P-HTFSC для отримання оптимальної структури, яка забезпечує високу ефективність перетворення світла в електрику. Чотири світлові характеристики J-V (струм короткого замикання: JSC, напруга холостого ходу: VOC, коефіцієнт заповнення: FF та ефективність перетворення: η) використовувалися як індикатори для оцінки характеристик пристрою. Результати моделювання показали, що для найкращої продуктивності пристрою CIGS P-HTFSC оптимальна товщина шарів CIGS і ODC повинна бути відповідно меншою за 2 мкм і декілька нм, тоді як оптимальна концентрація дефектів у шарі повинна становити 10¹³ cm⁻³-10¹⁸ cm⁻³, відповідно.

Ключові слова: CIGS, ODC, псевдогетероструктура, J-V характеристики, SCAPS-1D.